# Absolute distance metrology using frequency swept lasers

Matthew Stuard Warden
Merton College, Oxford


Thesis submitted in fulfilment of the requirements for the degree of Doctor of Philosophy at the University of Oxford

Trinity Term, 2011

# Absolute distance metrology using frequency swept lasers

Matthew Stuard Warden
Merton College, Oxford

Thesis submitted in fulfilment of the requirements for the degree of Doctor of Philosophy at the University of Oxford

Trinity Term, 2011

This thesis describes and evaluates two new interferometric distance measurement methods based upon the well known method of Frequency Scanning Interferometry (FSI). These new methods are known as Dynamic FSI and Cascaded FSI.

Dynamic FSI addresses the two problems, commonly seen in previous FSI implementations, of not being able to measure a moving target and having a slow measurement rate. This method measures stationary and moving targets equally well, and can determine the distance to the target at all times during the measurement, in contrast to previous methods, which obtain only a single measured length from a measurement process which can take up to a second to make.

Cascaded FSI was developed with the aim of increasing the accuracy and precision of FSI. This method allows for measurements with precision equal to that of displacement interferometry, and also provides a way of measuring length relative to the frequencies of atomic absorption lines, which are inherently more stable length references than a physical length artefact.

# Acknowledgements

I would like to thank and acknowledge the many people that have helped and supported me though the long process of finishing a DPhil.

To start with, I wish to thank my fellow students whom I shared an office with: Greg Moss, John Dale and Andrew Lancaster, for making it a pleasant place to work and periodically dragging me away from my screen for a much needed coffee. I would also like to acknowledge the support I have received from my supervisors, David Urner and Armin Reichold, who have always been happy to make time for me and provide optimism, scepticism, or encouragement as required.

Thanks also to Paul Coe, for his careful and patient instruction, to Patrick Brockill, for sharing his extensive knowedge of all things least squares, and to Stephen Gibson for many enlightening conversations about interferometry. I would also like to thank the physics support staff; the electronics workshop, mechanical design and mechanical workshop, and the particle physics secrataries.

Finally, I would like to thank my family and last, but not least, Kitty. Without their support and encouragement this thesis would not have been possible.

The author gratefully acknowledges financial support for his work from STFC under the auspices of studentship PPA/S/S/2006/4505.

This thesis was typeset using the LaTeXtypesetting package. Graphs and diagrams were produced using Matlab and CorelDraw. This thesis and the research it describes are original work carried out solely by the named author.



Material contained within chapters 4 and 5 of this thesis relates to patent pending inventions PCT/GB2011/051399 and PCT/GB2011/051397 held by Isis Innovation Limited (www.isis-innovation.com).

# Contents

# List of Figures

# List of Tables

# Glossary

**ADC** Analogue to Digital Converter

**ATLAS** A Toroidal LHC Apparatus (A particle detector at the LHC)

**CLIC** Compact Linear Collider

**CMM** Coordinate measuring machine

**DFT** Discrete Fourier Transform

**EM** Electromagnetic

**FSI** Frequency Scanning Interferometry

**HT** Hilbert Transform

**ILC** International Linear Collider

**kS/s** kilo-Samples per second

**LCLS** Linac Coherent Light Source

**LHC** Large Hadron Collider

**MS/s** Mega-Samples per second

**OPD** Optical Path Difference

**SCT** Semi-Conductor Tracker

$\oplus$ Quadrature sum

$\mathcal{F}$ Fourier transform

$\mathcal{F}^{-1}$ Inverse Fourier transform

$\mathcal{H}$ Hilbert transform

$\sigma_X$ Uncertainty in $X$

$\hat{X}$ Estimate of $X$

# Introduction

Many areas of science and technology rely on the ability to accurately determine length. The fact that this requirement is often easy to overlook is a testament to the success of many current technologies and processes used for length measurement. However, in certain more demanding areas, for example requiring measurement with high accuracy or over large areas, length metrology equipment is not so easily overlooked. Here, measurement requires expensive equipment that is labour intensive to operate and maintain, and even so a lack of measurement capability can still be a limiting factor. In such areas more sophisticated dimensional metrology tools can have direct benefits upon scientific and technological endeavours.

Examples of scientific areas with particularly challenging dimensional metrology requirements include the alignment of particle accelerators [20, 22] and astronomical telescopes [25], as well as formation flying satellite missions [60]. In industry, examples of areas that could benefit from more sophisticated dimensional metrology capability include construction of large objects such as aeroplanes and wind turbines, and also the calibration of coordinate measuring machines [63] and machine tools [57].

Optical interferometers are a frequently used tool in the area of dimensional metrology, due to their ability to make highly accurate and precise measurements [12]. Many of these can be thought of as variants of the Michelson interferometer design that dates back to 1887 [48]. Such interferometers can measure, with great precision and accuracy, the displacement of a reflective target along the line of a light beam. However, they cannot determine the *absolute distance* to the target. An additional limitation is that each interferometer can

measure only a single target at any one time. Many current interferometric measurement tools, although highly useful, have needed to be designed around these limitations.

Non interferometric measurement tools exist that have the capability for absolute distance measurement. These are commonly based around measuring the time of flight of a reflected pulse of light from a target. Although they are capable of rapid and accurate measurements, they do not have the innate accuracy and traceability of interferometric measurements. In addition, they are also usually restricted to measuring the distance to a single target only.

The method of Frequency Scanning Interferometry (FSI [1] ) is able to measure the absolute distance to a target, and can also measure multiple targets simultaneously. It operates using the same Michelson interferometer as is used for the displacement measuring interferometers mentioned above, but substitutes the continuous wave, fixed optical frequency laser for a continuous wave, variable optical frequency laser. A measurement is made by continuously sweeping the laser's frequency through a known amount, and recording the phase change in the interferometer as this is done. It may be shown that the ratio of change in phase to change in laser frequency is proportional to the interferometer's optical path difference, allowing absolute distance to be measured with this system.

However FSI suffers from several drawbacks which explains why it is not more widely used. Typical FSI methods such as those described in [3, 20, 58, 60] suffer from the following limitations: Compared with displacement interferometry, measurement is less precise and is made at a slower rate; the target is required to be stationary during the measurement; expensive and delicate external cavity diode lasers are usually required; and length is measured relative to a physical length artefact with limited stability.

The purpose of this thesis is to propose and investigate methods that mitigate some of these problems. Not all problems have been addressed, and this thesis by no means proposes to present a complete measurement solution. The focus is instead on developing techniques that make FSI more competitive, and moving toward a situation where the great benefits of FSI are not outweighed by the current disadvantages.

[1] There are multiple other acronyms in use for this method, summarised in appendix A

To this end, this thesis proposes two new FSI based methods for absolute distance measurement. The first method, 'Dynamic FSI', addresses the problems of not being able to measure a moving target and having a slow measurement rate. This method measures stationary and moving targets equally well, and can determine the distance to the target at all times during the measurement, in contrast to previous methods, which obtain only a single measured length from a measurement process which can take up to a second to make.

The second method, 'Cascaded FSI', was developed with the aim of increasing the accuracy and precision of FSI. This method allows for measurements with precision equal to that of displacement interferometry, and also provides a way of measuring length relative to the frequencies of atomic absorption lines, which are inherently more stable length references than a physical length artefact.

There are several themes that run through this thesis and the new measurement methods proposed within. A model based approach was used to develop both new FSI methods; the emphasis being on obtaining as much useful information as possible from the recorded data in each measurement. In several places an estimate is made of a discrete quantity: The knowledge that there is a restricted set of possible values for this quantity sometimes allows measurement error to be reduced.

The contents of this thesis are arranged as follows. Chapter 1 contains discussions of some potential application areas for FSI, and some relevant background concepts. In chapter 2, a mathematical model of an FSI measurement is developed. Chapter 3 contains a review of interferometric measurement methods, which also serves to introduce more background concepts required later. Chapter 4 describes Dynamic FSI, and contains numerical and experimental analyses of the method, and Chapter 5 gives the same treatment to Cascaded FSI. Finally, Chapter 6 contains a summary of the main results and conclusions of the thesis.

# Chapter 1

# Background and Applications

This chapter starts with a summary of some areas where FSI measurement methods could be used, in section 1.1. This provides some context for the new measurement methods presented later on, and illustrates how features such as absolute distance measuring capability, or a faster measurement rate, can have practical benefits.

Section 1.2 introduces some general concepts relevant to all the interferometric methods described in this thesis, paying particular attention to the requirements for an interferometric method capable of absolute distance measurement. These concepts will be used in later chapters, which contain more detailed analysis and description of specific interferometric measurement methods.

Some further background material is included in section 1.3.

## 1.1 Applications

FSI is capable of making precise and absolute distance measurements. This section reviews some example areas in science and industry which require this kind of measurement and could potentially benefit from a suitable FSI measurement system.

### 1.1.1 Scientific Applications

As the very purpose of much scientific research is to push the boundaries of knowledge by testing in more extreme conditions, or measuring with more sophisticated sensors, it should come as no surprise that this often leads to demanding dimensional metrology requirements. Two areas in which this is the case are particle accelerators and certain space missions.

#### Particle Accelerators

Current particle accelerators used for particle physics research already have challenging requirements on the position and stability of large numbers of components, but the next generation of planned linear particle accelerators such as the International Linear Collider (ILC) [15] and Compact Linear Collider (CLIC) [6] will take these requirements to the extreme. I shall describe here two specific examples where FSI has already been used in particle accelerators used for particle physics.

Both the ILC and CLIC have extremely demanding requirements for the alignment of large numbers of components. The cause of some of these requirements stems from the fact that these machines are linear accelerators (as opposed to existing machines such as the Large Hadron Collider and the Tevatron, which are circular machines). Each particle bunch passes only once through the accelerator, and is not recycled as it would be in a circular machine. Therefore, in order to achieve a rate of interactions competitive with a circular collider, linear colliders must produce as many interactions as possible from each bunch collision. This is done by compressing the bunches to a very small size at the collision point, creating as high a density of particles as possible and therefore maximising the potential for interactions: The nominal beam size at the collision point is 639 nm $\times$ 5.7 nm for the ILC [15] and 60 nm $\times$ 0.7 nm for CLIC [6].

In order to be able to focus the bunches down to a suitably small size at the collision point, the bunches must be very well collimated at the entrance to the final set of focussing magnets. The relevant figure of merit for this is the *emittance*, which should be made as

small as possible. Various kinds of misalignments of elements along the beam line can cause the emittance to grow, so in order to achieve a high rate of particle interactions, these misalignments must be kept within strict tolerances. Some potential causes of emittance growth are as follows: Misaligned quadrupoles will give a transverse kick to the beam particles that is of different size for particles of different energies; rotated quadrupoles will couple the large horizontal emittance into the much smaller vertical emittance; and tilts of radio-frequency (RF) cavities will give a transverse kick to the beam which will then be misaligned with respect to the next quadrupole it passes through.

In order to keep the emittance to an acceptably small level these potential causes of misalignment must be controlled. There are two elements to this control. Firstly, the components are aligned into position along the accelerator tunnel. This is done with respect to sets of fiducial marks on the exterior of the components, which themselves have a known relation to the functional geometry of the element such as the magnetic or electric field axes. Obtaining this relation by measurements is referred to as fiducialisation. The fiducials on the components are then aligned to a set of *reference marker* fiducials in the tunnel which have been accurately surveyed before and encode the accelerator's co-ordinate system. Secondly, it is then possible to use the beam itself as a diagnostic by measuring its properties as it passes through the accelerator. Information gained from this is used to steer the beam in such a way as to minimise the emittance growth, and/or physically move components into more optimal positions. But in order for this to work well the components must be well enough aligned initially. This process is known as *beam based alignment*.

The positions of accelerator components will slowly drift with time due to, for example, slow deformations of the floor, or thermal expansion of components. This means that periodic realignments of the components relative to their external fiducials must be done. Therefore the alignment method used must be more than merely accurate enough, it must also be possible to perform it periodically without interrupting the operation of the accelerator too much, which means that it should be fast.

An alignment tool for the ILC that addresses these issues and which uses FSI as a key

measurement tool has been built and tested. This is known as the Rapid Tunnel Reference Surveyor (RTRS). It is a self-propelled, automated survey robot that can measure the location of reference marker fiducials along an accelerator tunnel wall. This can be done quickly, and with minimal human interaction. It also opens the possibility of surveying whilst the accelerator tunnel is still too radioactive for humans to enter. Ultimately, the accelerator down-time could be minimised by surveying the tunnel with the RTRS whilst the accelerator was running.

It operates by running along a rail on the accelerator tunnel wall and surveying the positions of the wall reference markers. These will be located in groups of several markers at regular intervals along the tunnel wall. The RTRS measures the relative location of several adjacent groups of markers. It then moves along one interval such that it can detect one new group of markers at the front, and can no longer detect the group that was previously at the back. It then measures the relative location of this new set of adjacent groups, which partially overlaps with the previous set. This procedure is repeated along the entire length of the tunnel and the recorded data can then be used to determine the relative location of all the markers.

FSI has several advantages as the choice of distance measurement tool in the RTRS: It can measure absolute distance - required so that it can re-establish the relative locations of all the markers within range at each measurement; it is capable of high precision; and it is relatively cheap to add more measurement channels, as a large amount of the cost of the measurement system is in the laser and any optical amplifiers used and the light output from this can be shared amongst multiple interferometers.

I have only briefly described the RTRS here, as it is the subject of previous theses [34, 22].

The quality of measurements made by particle physics detectors is also dependent upon the alignment of elements within them. This is particularly true for particle tracking detectors which need to measure trajectories to very high accuracies. An FSI based alignment system is in use at the Large Hadron Collider (LHC), inside the ATLAS detector's Semiconductor Tracker (SCT) [50]. The SCT consists of a large number of position sensitive silicon

strip detectors. Data recorded by it plays an important part in measuring the momentum and impact parameters associated with the tracks of long lived charged particles. The performance of this detector subsystem relies upon knowing the precise location of the silicon strip modules (mounted upon a carbon fibre support structure, designed to be as light and rigid as possible). The standard method for achieving this is to use particle tracks themselves to determine the modules' relative locations. However, the ATLAS SCT is unusually large, and it was feared that distortions of the support structure occurring on short time-scales could not be measured using the particle track method, which needs time to accumulate enough data to make an accurate measurement of the modules' locations.

For this reason, a network of 842 interferometers has been installed inside the ATLAS SCT, each using FSI to measure absolute distance to a precision of about 1 micron. This system can additionally monitor displacements with a precision of 50 nm with a novel 'vibrato FSI' mode [30]. Combining measurements from all the interferometers, which are made between points on the support structure, gives information about the most common degrees of freedom of the structure's distortion. This can then be used to help determine the alignment of the silicon tracker modules.

As with the RTRS, the example of the ATLAS SCT alignment is only briefly described here, as it is the subject of several previous theses [28, 35, 20, 49, 29]. An investigation has been done into using a very similar method to monitor alignment inside a future ILC detector [66].

Particle accelerators have many other uses apart from fundamental particle physics research. They may also be used to create ultra-short pulses of X-rays in accelerators known as free electron lasers, such as the Linac Coherent Light Source (LCLS). As with linear colliders, this kind of accelerator also has stringent alignment tolerances [54]. A key set of components used for producing the X-ray pulses are the undulator magnets, parallel arrays of magnets with alternating polarity. When a bunch of electrons passes between the two arrays of magnets it oscillates laterally and emits the synchrotron radiation that constitutes the X-ray pulses. The gap between the two rows of magnets in each undulator is usually

variable and requires a sensor to precisely determine its size; FSI would be a suitable sensor for performing this measurement. Alignment of undulators with respect to each other and to the intervening quadrupoles is also critical and may also benefit from an FSI based monitoring system. In particular, the distance between undulators must be controlled to sub-micron accuracy. The application of an FSI based monitoring system for free electron laser alignment monitoring is a topic currently being investigated by the Oxford AMULET group.

### Space applications

Another area where advanced dimensional metrology methods are a key enabling technology for future scientific missions is space science. The past few years have seen several proposed scientific space missions that require accurate dimensional monitoring of the relative location of separate satellites [60, 1, 32, 43], however many of these missions have not progressed past the early planning stages. Apart from the large budgets typically required for these missions, a key reason for this is the lack of supporting technologies in several areas, including dimensional monitoring methods. Advances in the required supporting technologies would make this kind of mission more feasible.

One class of missions that requires extremely precise metrology methods is that of synthetic aperture telescopes. These use multiple telescopes to achieve a resolution comparable to that of a single telescope that has the same size as the maximum separation between the telescopes. One proposed mission that would have used this technique was the ESA Darwin mission, which had the goal of observing planets around nearby stars. The mission requirements included a metrology subsystem capable of measuring the absolute distance between satellites to within 70 micrometers over a range of 250 metres for which an FSI based system was studied [60].

### 1.1.2 Industrial Applications

Certain industrial applications require high precision measurement capability. These include the aerospace, automotive and shipbuilding industries. The calibration of machine tools also requires high accuracy measurement. A future area where high precision measurement capability could be required is the wind energy sector.

A general purpose workhorse used for many of these applications is the laser tracker, an interferometer fitted with a rotatable mirror used to steer its output beam. It is fitted with a position sensitive detector that allows it to track the movement of a corner cube retro-reflector and the mechanics that rotate the mirror are fitted with precise angle encoders. In this way it can measure both the distance and the angle to the corner cube retro-reflector, enabling its 3D coordinates to be determined.

Such systems can be made to work using only displacement measurements, but in fact most modern laser trackers also have absolute distance measurement capability. These operate by modulating the amplitude or polarisation of the output beam and using this to time the round trip to the target. The measurements with these devices are neither as precise nor as accurate as interferometer measurements. More capable absolute distance measuring methods such as those discussed in this thesis could improve the capability of tools such as laser trackers.

Another industrial metrology tool is the Laser Tracer, which is essentially a laser tracker that has been designed specifically to make highly accurate distance measurements, and that deliberately discards the data from its angle encoders. It is used for CMM and machine tool calibration, and operates by measuring the distance to the probe or tool head as it is moved through a repeatable sequence of locations. The Laser Tracer is then moved to a different location and the CMM or machine tool repeats its sequence of movements. This procedure is repeated at least four times, and the data recorded can then be used to precisely determine the movements of the machine using the principle of sequential multilateration. This is used to generate an *error map* for the machine, which allows it to position its head

more accurately in future use. The new FSI methods described in this thesis are currently being studied for their potential for inclusion on an FSI-enabled Laser Tracer.

Another commonly used measurement tool is the laser scanner. This is similar in concept to the laser tracker, but instead of measuring a single, reflective target, it rapidly scans the laser beam across a measurement area and measures distances to whatever the laser beam hits in each direction. Doing this requires absolute measurement capability. Some devices measure distance by modulating the amplitude or polarisation of the output beam, but there is a commercially available laser scanner which uses FSI [19, 38].

## 1.2 Principles of interferometry

FSI is markedly different from the more commonly used method of displacement interferometry. Each method has its own strengths and weaknesses. This section contains an analysis of the basic principles of interferometry, in an attempt to determine the underlying cause for these characteristic strengths and weaknesses.

In the process, I shall address several key questions:

- What is the root cause for the main limitation of displacement interferometry; that it cannot be used to measure absolute distance?
- What key features are required of an interferometry system in order to overcome this limitation?
- How does FSI fulfil these requirements?

### 1.2.1 Fundamentals of fixed frequency interferometry

One way to measure the distance between two points is to send something of known speed between them, and measure the time taken. Distance may then be calculated from the simple formula: distance = speed $\times$ time.

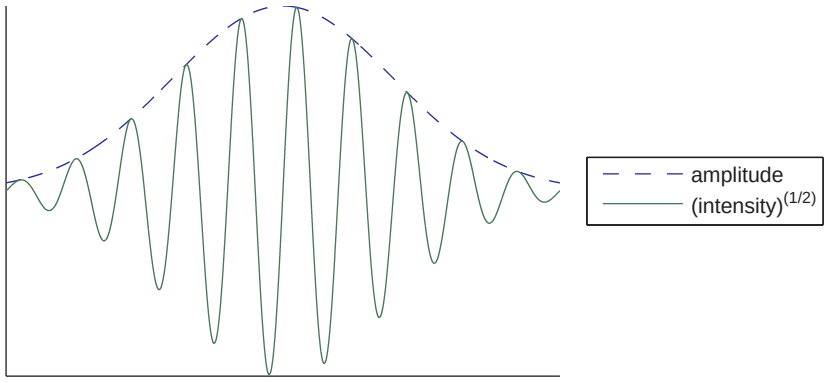


Figure 1.1: Comparison of the sharpness of an electromagnetic wave with a pulse of light: The pulse is merely an amplitude modulation of the electromagnetic wave, and can never be quite as sharp as the electromagnetic wave crest itself.

One system that operates in this manner is a *time of flight* range-finder, which produces a pulse of light and times the return of its reflection. To measure distance precisely with this system we would need to time the return of the reflection precisely. To do this, the signal must have sharply defined features, and the light detection system must be fast enough to resolve these features. Both signal creation and detection in this kind of system is typically done with high speed electronics, so an important limitation of the precision of these systems is the speed of the electronics involved.

A further limitation of time of flight measurements is that the sharpness of a pulse of light is limited by the fact that it is merely an amplitude modulation of a carrier wave, as illustrated in Fig. 1.1. This places a fundamental limitation on the sharpness of the pulse for any given carrier wave. Another option for a timing signal is to use the peaks and troughs of the electromagnetic carrier wave itself. This is the signal that interferometric measurements use, and has the potential for more precise measurements. Also, high frequency electronics are no longer required to create this signal.

The problem remains how to detect this signal. To do this, we may employ a method commonly used in electronics when dealing with high frequency signals: The high frequency signal is mixed with another signal of similar frequency to generate a beat signal with a frequency equal to the frequency difference of the two signals. The system may thereafter deal with this lower frequency beat signal, which retains some information about the timing

of the high frequency signal, yet is easier to deal with in practice because lower speed electronics may be used. As our incoming high frequency signal is optical, it is combined with another optical signal of similar frequency, and the beat signal may be observed as variations in the intensity of this combination. These intensity variations contain information about the returning optical signal which may be used to infer something about the round trip distance the returning optical signal has travelled. However, as we shall see, this information won't simply be the round trip time of the light signal, as we would have ideally hoped for. Nevertheless it can be (and is regularly) used to make useful distance measurements.

In order to employ this beat generation method, we require, in addition to the distance measuring signal, another signal of similar frequency to mix with it and generate a beat signal. The requirement for a 'similar' frequency stems from the fact that if the beat signal is too high in frequency our electronics will not be fast enough to detect and process it.

What we can do is to take a fraction of the outgoing light and mix this with the returning, reflected light. However, this will not necessarily produce a beat signal with a low enough frequency to work with: If the frequency of the outgoing electromagnetic wave were to vary, then as it takes time to return from the round trip to the reflector, the distance measuring signal and the mixing signal will have different frequencies, generating a beat signal that could potentially have too high a frequency to detect.

This places a limit on the amount of acceptable frequency variation of the light source when we use this interferometric mixing technique. This means that if we wish to measure large distances then we must use a spectrally narrow, coherent light source.

One such light source is a laser with a fixed optical frequency. An advantage of using this as a light source is that distance can be measured relative to a stable length standard, which is the laser's vacuum wavelength.

Such a fixed frequency, coherent light source emits an electromagnetic wave that is an almost pure sinusoid of a fixed frequency. The return signal we receive from the reflector would thus also be a pure sinusoid of the same frequency. But with this light source there is a

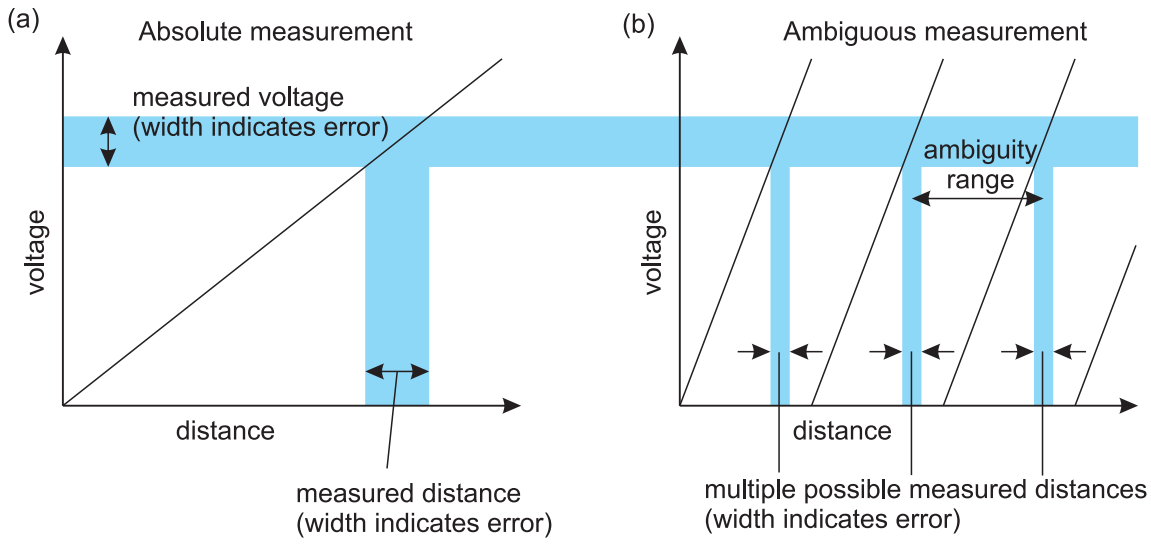


Figure 1.2: Examples of an absolute and and an ambiguous measurement, illustrating the difference in measurement precision and the ambiguity range.

problem: Recall that we want to measure distance by timing the return of an electromagnetic wave-crest from the reflector, yet each wave-crest is identical to all the others: They are principally indistinguishable. This means that we can't make a straightforward measurement of the round trip time of this light of the sort that could tell us directly, for example, "the round trip time is 30 ns".

The only information that can be obtained is the phase difference between the outgoing and incoming waves. A summary of how this may be achieved technically is given later, but for this discussion, we may ignore these details: As was said earlier, the limitation comes from the very nature of the signal itself, rather than the specific signal detection method.

What information can we gain from measuring this phase difference? We do not know the integer number of wave crests emitted in the time that it takes one wave crest to travel to the reflector and back. What we measure instead is the fractional part of this number. This causes something I will refer to as the ambiguity problem: The length measurement is not absolutely determined, but is ambiguous, with our measurement corresponding to many possible lengths (given by different possible values of the integer number of cycles). This ambiguity problem is purely caused by the periodic nature of the signal we are using.

The issues around this ambiguity problem are illustrated graphically in Fig. 1.2. This

shows examples of both an absolute (unambiguous) measurement and an ambiguous measurement. For each example consider that the distance measurement system acts as a transducer, generating some easy to record signal, such as a voltage, that varies according to some function of the measured distance. Each example shows a different possible mapping between the measured distance and the voltage created by the transducer. The measurement shown on the left has a 1-1 mapping between distance and voltage. This means that it makes an absolute distance measurement, without ambiguity. On the right of the figure is an example of an ambiguous measurement. Here, a given voltage value no longer corresponds uniquely to a single possible measured distance. Hence by measuring the voltage we cannot make a unique determination of the distance, and the measurement is said to be ambiguous. The 'ambiguity range', marked in the figure, is the separation between adjacent distances that are both consistent with the same measured voltage. It is half (due to the round trip) the distance the signal travels within one period. For a fixed frequency, coherent light source, this is half the wavelength of the light used.

Clearly it is an advantage to be able to measure a distance absolutely, but there are also certain advantages to be gained from a measurement that exhibits ambiguity in this way. Notice the gradient of the line in each example: It is larger for the ambiguous measurement (when there is the same range of output voltages for both types of measurement). This means that the ambiguous measurement has a higher sensitivity to distance changes. Note also that if we were to reduce the ambiguity range, then the gradient would increase further, increasing the sensitivity even more. This leads to the important realisation that there is a trade-off between ambiguity length and sensitivity: Reducing the ambiguity length increases the sensitivity and vice versa. This trade-off is inherent to any ambiguous measurement of this sort, not merely interferometric ones. Note also that typically we will have a limited range of voltages that we may detect. This means that the absolute measurement will have a limited range of distances it can measure (unless its sensitivity goes to zero), whereas the ambiguous measurement is not limited in this way.

An ambiguous measurement system, by its very nature, gives little useful information

when only a single measurement is made. Where this kind of measurement system comes into its own, though, is in making repeated measurements to the same object. Referring back to Fig. 1.2, one can see that it is possible to make highly precise measurements of how much the distance changes as long as these changes remain within one ambiguity length. If the measurement system measures continuously as the distance is changed over multiple ambiguity lengths, then it is still possible to measure the total displacement, as long as the system is able to keep track of the number of ambiguity lengths that have been passed through. In this way it is possible to measure large displacements with high precision.

It is possible to measure large 'absolute' distances with displacement interferometry by physically moving a target between the two ends of the distance to be measured and measuring the displacement as this is done. There are several drawbacks to this method: This is a labour intensive and slow operation; if the system loses count of the number of ambiguity lengths moved over at any point (for example, if something were to momentarily block the laser beam) then the measurement must be started again; and it is not always practical or possible to move the target continuously and under constant observation between the desired points.

### 1.2.2 Unambiguous measurement

We have seen that using interferometric mixing requires the use of a coherent light source. If the frequency of this source is fixed, and if it is unmodulated in any other way, then we end up with an ambiguous measurement system having all the pros and cons that were discussed above.

To make a light source for an absolute distance measurement system we must break this periodicity in some way. We would like to do this in a way that still enables us to use interferometric mixing, so the light source must remain coherent. One way of doing this is to modulate the frequency of the light source. If the frequency variation is slow enough then the signal will be nearly periodic on short time scales (and interferometric mixing will still work), yet the signal considered as a whole will not be periodic. The frequency variation has

given it an identifiable structure and this allows, at least in principle, the round trip time to the target to be calculated unambiguously.

In this way, using interferometric mixing combined with a frequency modulated light source that is not periodic in the same way as a fixed frequency light source, it is possible to make precise absolute distance measurements that aren't limited by the speed of the detection electronics. This is the method which is used in FSI.

An absolute distance measurement, in contrast to a displacement only measurement, has a definite zero point to the measurement. The location of this zero point is not always in a convenient location, and may well be inside the instrument itself. This is in no way a drawback, however: We can define a zero position arbitrarily by recording the measured distance to this position and subtracting this value from subsequent measurements.

### 1.2.3 Summary

The cause of ambiguous measurement in interferometry is the periodicity of the distance measuring signal it uses. There are various pros and cons of ambiguous measurements.

To make unambiguous measurements one must use a non-periodic signal. If using a coherent light source, as is required for interferometry, this means that it must be modulated in some way. FSI modulates the frequency of the light source. Doing this enables precise, absolute distance measurements that are not limited by the speed of the detection electronics.

One could imagine other absolute distance measurement methods that create different kinds of non-periodic signal. The distinguishing characteristic of FSI is thus the particular signal it uses, which is non-periodic when considered as a whole but also may be detected using interferometric mixing.

## 1.3 Additional metrology issues

This section contains a brief discussion of two further issues that are important to length metrology. These are the role of length standards in distance measurement, and the effect of the refractive index of air upon interferometric distance measurements.

### 1.3.1 Length and Frequency standards

An important concept in the science of metrology is that of traceability, the idea that all measurements should be traceable in an unbroken chain back to the definition of the units for the measurement. When measuring length within the SI system, the measurement should be traceable back to the SI metre, defined as the length of the path travelled by light in vacuum during a time interval of 1/299 792 458 of a second. It is desirable to have as few links in this traceability chain as possible. This reduces the accumulation of measurement uncertainty that happens at every stage, and also reduces the chance of errors due to mistakes.

Many implementations of FSI make their length measurements relative to the optical path difference of a *reference interferometer*. In order for these measurements to be traceable, this reference interferometer must have its length calibrated at some point, which then becomes one step in the traceability chain. The problem with measurements made relative to a physical length standard, such as a reference interferometer, is that they rely on the stability of the length standard after calibration. The overall measurement uncertainty is thus increased, not just due to the uncertainty in the calibration, but also due to the instability of the length standard.

An alternative option for a length standard is to create one using a physical process. For example, the wavelength of a Helium-Neon laser is determined by the energy levels of the gas atoms within the laser cavity. These energy levels may be used as the basis for an inherently stable length standard: The wavelength of light output from the laser depends very little upon external factors such as ambient temperature when compared to typical physical length standards.

| Parameter | Nominal value | Change required for +10ppb change in n |
|---|---|---|
| Air Temperature | 20 °C | -0.01 °C |
| Atmospheric Pressure | 101.325 kPa | +3.8 Pa |
| Relative humidity | 50 % | -1.1 % |
| $CO_2$ content | 450 ppm | +71 ppb |

Table 1.1: Summary of changes in air refractive index, calculated using the NIST engineering metrology toolbox [52], which implements the Ciddor equation [18].

Later on in this thesis, I will present a method which gives the option of measuring length relative to atomic transition lines in an absorption gas cell. These, as with the He-Ne laser example above, have only a very weak dependence upon ambient conditions, and can thus be used as a stable length standard.

### 1.3.2 Refractive index

The above discussion has described interferometric length measurement as a timing measurement. If we measure the time $\tau$ for our signal to return from being reflected from a target then the distance, $L$, to that target may be calculated as

$$L = \frac{\tau}{2}\frac{c}{n} ,$$

where $c$ is the speed of light in vacuum, $n$ is the refractive index of the medium the signal travels through (which for many applications will be air) and the factor 1/2 takes account of the signal's round trip.

To calculate distance we need to know $n$, which tells us the speed at which the signal travels. When measuring in air, there are various ways in which $n$ may be determined. These include using a refractometer, which directly measures $n$, or by measuring the parameters upon which it predominantly depends: temperature, pressure, humidity, and $CO_2$ content. A summary of the dependence of air's refractive index upon these parameters is given in Table 1.1.

The length measurement precision obtainable using these methods is limited, however,

as they generally measure the refractive index in a slightly different location than the path of the light beam. We therefore rely on homogeneity of the air in order to extrapolate our measurements to this location. Although some parameters, such as pressure, homogenise rather quickly, others, such as temperature, may be very inhomogeneous (air is a poor conductor, and temperature is homogenised more by bulk transport than conduction). So, regardless of how well we measure refractive index in one location, our uncertainty on knowledge of the refractive index along the measurement beam path will be limited by inhomogeneity. A thorough discussion of these issues can be found in [27]. Indeed, partly due to this reason, according to Bobroff [12] "It is difficult to obtain a measurement accuracy of $10^{-7}$ when working in air".

Some attempts have been made to solve this problem by determining the speed of light directly along the signal path. One method is to measure the signal delay with two different frequencies of light [45], and make use of the dependence of the dispersion of air upon its refractive index to give an indication of the speed of the signal. Another method is to send a pressure wave along the same line as the beam, and use the fact that the speed of sound in air has a different dependence upon parameters such as temperature and pressure than the speed of light[42].

Another method of reducing this problem is to alter or even to remove the medium entirely, by surrounding the light path with an air-tight container or pressure vessel and either replacing the air with, for example Helium, or evacuating the beam path entirely. This enables highly accurate measurements to be made, at the cost of the severe amount of engineering required.

Another issue that becomes more important when measuring over large distances, greater than 10 m or so, is that refractive index gradients will curve the path of the light beam [26].

In this thesis, it will often be convenient to refer to the distance to be measured in terms of the optical path difference (OPD), $D$, which is related to physical distance, $L$, by

$$D = 2nL \; . \tag{1.3.1}$$

This thesis describes methods for measuring the OPD, and it is assumed that to use these in practice one would also adopt a standard method for determining the refractive index.

### Dispersion

Another complicating factor that this thesis does not attempt to address is that of dispersion, i.e. a wavelength dependent refractive index in the path of the interferometer's beam. It is assumed that most applications of the methods described in this thesis will have the interferometers placed in air, which is only slightly dispersive, with $dn/d\lambda \simeq 10^{-9}/nm$. In addition, in a major case of interest, when a reference interferometer is used as described in section 3.3.1, FSI methods are independent of the refractive index of the medium if we only assume that both reference and measurement interferometers are in the same medium.

However, it should be noted that if FSI methods are used in dispersive media, which may occur when using optical fibre based interferometers, or if dispersive optics such as lenses are placed in only one arm of an interferometer, then care must be taken to investigate and compensate for the additional wavelength dependence these interferometers will now exhibit.

More discussion on this topic may be found in [36].

# Chapter 2

# Mathematical model of FSI

This chapter describes background material common to all the distance measurement methods that will be introduced in the next chapter. It contains three sections.

The first section develops a mathematical model of the measurement process. This will be used as the basis for our theoretical understanding of the various measurement methods described throughout this thesis.

The second section describes methods for calculating interferometric phase from the intensity output of an interferometer. This will be used as a preliminary analysis step in the interferometric methods described later on.

Finally, in section 2.3, a general notation is defined that is suitable for describing the various measurement methods in later chapters.

## 2.1 Mathematical interference model

In this section I present a mathematical model of the interference in FSI. This model was the basis for the development of the new interferometric methods presented in chapters 4 and 5, but it will also be useful to have this model to hand for the review of interferometric methods in the next chapter.

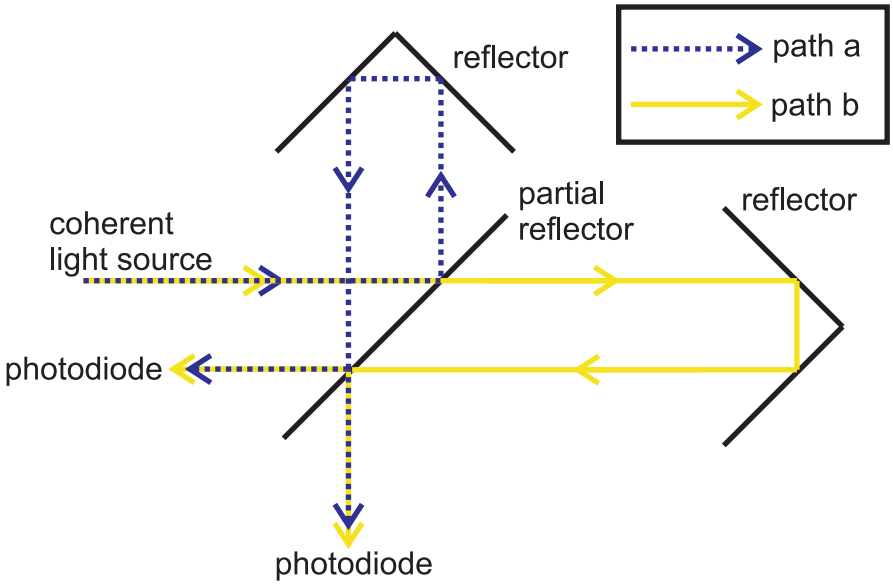


Figure 2.1: A Michelson interferometer

To start with, consider the typical setup for a distance measuring interferometer as illustrated in Fig. 2.1. After leaving the light source, the light beam is split by a partial reflector and sent along the two *arms* of the interferometer. One split beam is directed along a short path of fixed length. The other split beam is directed along the length to be measured to a reflector. This sends the beam back to be recombined with the first split beam at another partial reflector (often some part of the first partial reflector is used for this). The combined beam exits in two directions, and a photodiode is used to measure the intensity of one or both of these combined output beams. The recombination of the beams and detection of their intensity with a photodiode generates the interferometric mixing signal that was previously discussed in section 1.2.1.

### 2.1.1 Model options

At least three different models have been used in the literature to explain the occurrence of the interference signal in an FSI measurement. Some of these models are sufficiently different that it is not immediately obvious that they are even describing the same phenomenon. To clarify this situation, I present here a brief review of these different models, which I shall refer to as the 'steady state' model, the 'beat frequency' model, and the 'time delay' model.

Perhaps the most common is the 'steady state' model, as used in for example [41, 61]. This is the same model that is typically used in fixed frequency interferometry. It contains the implicit assumption that both the optical path difference and the laser frequency remain fixed during the period of time required for the light to travel the length of the interferometer's arms and back. This is a justified assumption to make for fixed frequency interferometry, but in FSI the laser frequency is deliberately being varied as fast as possible and some potential FSI applications are required to measure large distances. So in this case it may be prudent to investigate the validity of this assumption.

Another model, one that at first glance may appear to be describing a different phenomenon entirely, is the 'beat frequency' model, as used by [9, 56]. This model considers the fact that the swept frequency laser light in an FSI measurement takes different amounts of time to travel down the two interferometer arms, and as the frequency of the light is being varied in time, this means that the light reaching the detector from each arm will have a different frequency. A beat signal will therefore be generated. The frequency of this beat signal is

$$f_{\text{beat}} = \frac{\partial \nu}{\partial t}\tau \ ,$$

where $\tau$ is the difference in light travel time in the two arms of the interferometer. Measuring $f_{\text{beat}}$ allows the distance corresponding to the time delay, $\tau$, to be determined.

A third model, the 'time delay' model, has been seemingly independently proposed by Glombitza [33] and Zheng [67]. It takes a more low level approach that explicitly models a swept frequency electric field travelling two unequal path lengths in a two beam interferometer, calculating the observed intensity output as the squared amplitude of the electric field output from the interferometer.

All three models predict the same FSI signal (although the 'beat frequency' model is unable to predict the phase of the FSI intensity signal). In this sense they may be considered as three different ways of describing the same phenomenon. The 'time delay' model offers the most comprehensive approach, and this is the model that will be discussed in more depth below.

### 2.1.2 Development of time delay model

Consider a two beam interferometer similar to that of Fig. 2.1, illuminated with a linearly polarised electromagnetic (EM) wave. The magnitude of the electric field at the entrance to the interferometer is written as

$$E(t) = \mathrm{Re}\left[ae^{i\theta(t)}\right] \ ,$$

where $a$ is the amplitude of the wave and $\theta(t)$ is the phase of the wave at a time $t$. Note that although this appears similar to *complex phasor* notation, it is not: The frequency of the EM wave we consider is not time invariant and therefore the standard complex phasor notation is not suitable.

The *instantaneous frequency* of the EM wave, $\nu(t)$, is defined to be proportional to the time derivative of its phase, $\theta(t)$,

$$\nu(t) = \frac{1}{2\pi} \left.\frac{d\theta(t)}{dt}\right|_t \ . \tag{2.1.1}$$

The EM wave enters the interferometer and is split into two parts, each following a different path onto a single photodiode. The time taken for light to travel each of these paths is labelled as $\tau_1$ and $\tau_2$. The effect of this propagation time is modelled as a delay to the phase, $\theta$, of the light arriving at the detector from each path. The electromagnetic field at the detector, $E_{det}$, is the sum of the contributions from the two paths,

$$E_{det}(t) = \mathrm{Re}\left[a_1 e^{i\theta(t-\tau_1)} + a_2 e^{i\theta(t-\tau_2)}\right] \ ,$$

where the contributions from the two paths have amplitudes $a_1$ and $a_2$, which may in general be different.

Defining a shifted time variable, $t' = t - \tau_1$, and a quantity $\tau$ as the difference of the travel times of the two arms, $\tau = \tau_2 - \tau_1$, the electromagnetic field at the detector can be

expressed as the product of a carrier wave, A, and a modulation envelope, B,

$$E_{det}(t) = \mathrm{Re}\left[\underbrace{e^{i\theta(t')}}_{A}\underbrace{\left(a_1 + a_2 e^{-i(\theta(t')-\theta(t'-\tau))}\right)}_{B}\right] .$$

The *interferometric phase*, $\phi$, is defined as

$$\phi(t) = \theta(t') - \theta(t'-\tau) . \tag{2.1.2}$$

The intensity at the detector is given by the squared modulus of the modulation envelope, B,

$$\begin{aligned} I_{det} &= \left|a_1 + a_2 e^{-i\phi}\right|^2 /2\eta \\ &= \left(a_1^2 + a_2^2 + 2a_1 a_2 \cos(\phi)\right) /2\eta \\ &= I_1 + I_2 + 2\sqrt{I_1 I_2}\cos(\phi) , \end{aligned} \tag{2.1.3}$$

where $\eta$ is the characteristic impedance of free space, and $I_1$ and $I_2$ are the intensities the light from the two paths would have individually if not affected by interference.

Equation (2.1.3) is an exact expression within this model for the observed intensity detected during an FSI measurement, which varies sinusoidally with the interferometric phase, as defined in Eqn. (2.1.2). However, Eqn. (2.1.2) does not provide a usefully straightforward relationship between the quantities we are interested in (which are laser frequency, $\nu$, interferometer OPD, $D$, and interferometric phase, $\phi$). A first step to obtaining a simpler relationship is to write the phase of the EM wave, $\theta$, as a Taylor expansion,

$$\theta(t'-\tau) = \theta(t') + \frac{1}{1!}\frac{\partial\theta(t')}{\partial t'}(-\tau) + \frac{1}{2!}\frac{\partial^2\theta(t')}{\partial t'2}(-\tau)^2 + \frac{1}{3!}\frac{\partial^3\theta(t')}{\partial t'3}(-\tau)^3 + \dots .$$

Rearranging and substituting in the definition of frequency from Eqn. 2.1.1, this may be

written as

$$\theta(t') - \theta(t' - \tau) = 2\pi\nu(t')\tau - \frac{2\pi}{2!}\frac{\partial\nu(t')}{\partial t'}\tau^2 + \frac{2\pi}{3!}\frac{\partial^2\nu(t')}{\partial t'^2}\tau^3 + \dots .$$

Note that the left hand side of the above equation corresponds to the definition of interferometric phase in Eqn. 2.1.2, and therefore by dropping second and higher order terms in $\tau$ on the right hand side we obtain

$$\phi \simeq 2\pi\nu(t')\tau. \tag{2.1.4}$$

The time delay is related to optical path difference by $\tau = D/c$. Substituting this into Eqn. (2.1.4), we arrive at

$$\phi = 2\pi\frac{D\nu(t')}{c}, \tag{2.1.5}$$

and the interferometer's intensity output is thus

$$I_{det} = I_1 + I_2 + 2\sqrt{I_1 I_2}\cos\left(2\pi\frac{D\nu(t')}{c}\right). \tag{2.1.6}$$

In this approximation, the absolute phase (when expressed in cycles, $\phi/2\pi$) has the simple physical correspondence that it is equal to the number of wavelengths that fit into the interferometer OPD, $D$.

This final equation is the same as that used by the 'steady state' model. By deriving it in the above manner it may be seen that it is accurate only when the higher order terms in the Taylor expansion may be neglected. This is the case for the experimental measurements made later on in this thesis. However the approximation used to arrive at this equation will not always be valid. For example, if FSI is used to measure significantly larger OPDs, or the tuneable laser varies its frequency more rapidly, then neglecting the higher order terms may cause a significant discrepancy between the model and reality.

To investigate the accuracy of the approximation to the Taylor expansion above, consider the size of the second term, $(2\pi/2!)(\partial\nu(t)/\partial t)\tau^2$, with some typical values. The tuneable laser used for measurements in this thesis can vary its optical frequency at a rate of $\partial\nu(t)/\partial t =$

12 THz/s. At a distance of 1 metre in air (corresponding to an optical path difference of approximately 2 m), $\tau \simeq (2/3) \times 10^{-8}$ s. With these values, the value of the second term in the Taylor expansion is $1.2 \times 10^{-4}$ fringes. Unless measurement errors are brought down to this extremely small value, we need not be concerned by such a small discrepancy between the initial model and this approximation to it.

## 2.2 Working with phase

The above model describes the observed intensity output of an interferometer. This is the directly observable quantity in interferometry. However, when analysing interferometric data it is often more convenient to work with the interferometer's phase, which is linearly related to the OPD we wish to calculate, whereas the intensity is not. There are many different ways of calculating an interferometer's phase from recorded intensity values, and in this section I shall describe two.

The first method, quadrature readout, is commonly used in displacement interferometry, and is described here as background to the brief review of distance measuring interferometer methods in the next chapter.

The second method, based upon the Hilbert transform, is a method that is particularly suited for use with FSI. It is the method I have used for phase calculation in this thesis when evaluating FSI methods experimentally.

### 2.2.1 Quadrature readout

The model section above concluded with Eqn. (2.1.6), which has the intensity output of the interferometer varying with the cosine of the interferometric phase. The basis of the quadrature readout method of phase calculation is to arrange the interferometer optics so as to give an additional intensity output that varies with the sine, rather than the cosine of the phase. A method for doing this is illustrated in Fig. 2.2.

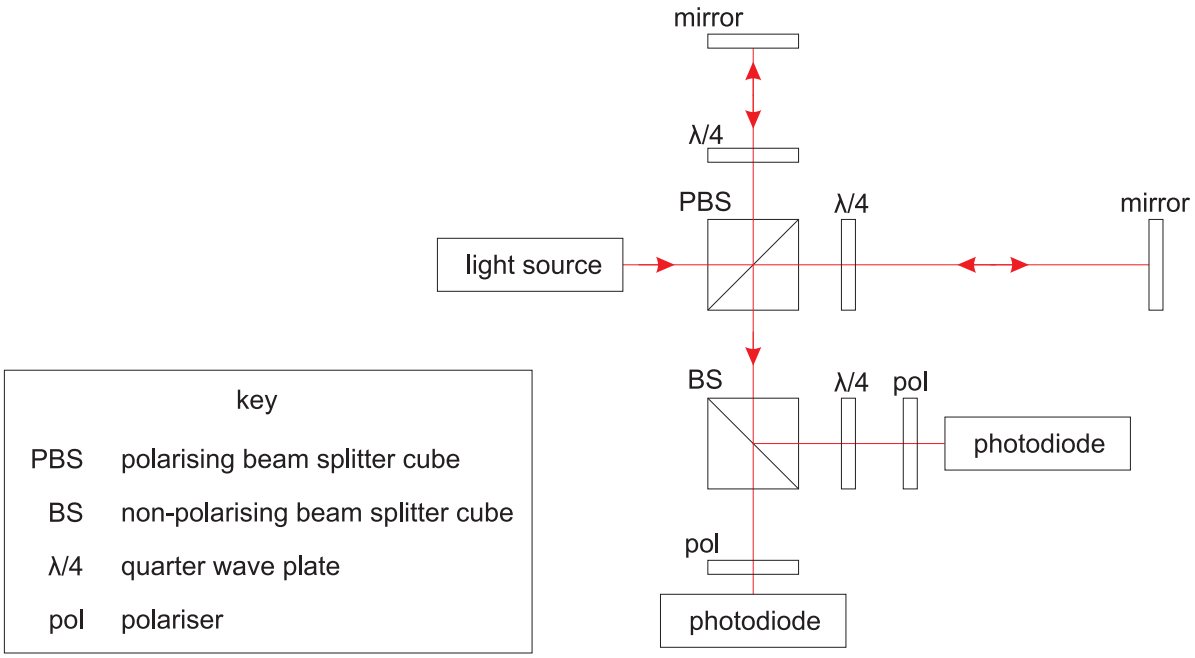


Figure 2.2: An example of a quadrature readout interferometer

This interferometric setup uses a polarising beam splitter cube, which transmits horizontally polarised light and reflects vertically polarised light. Light is sent into the beam splitter cube that is linearly polarised at 45 degrees to its axis. The light is thus split into two and sent into the reference and measurement arms of the interferometer just as it was in Fig. 2.1. The light beams return and are recombined in the beam-splitter cube. A quarter wave plate placed in each arm of the interferometer is used to direct the recombined output beam out of the lower face of the beam-splitter cube on the diagram.

After recombination two copies of the light are made using a non polarising beam splitter cube. As the light from each arm has orthogonal polarisations, it must be sent through a polariser oriented at 45 degrees to the polarisation axis of each light beam in order to observe interference. One of the copies of the light beam has a phase difference between the light from each arm added in with the use of a quarter wave plate. This is chosen such that the optical path length through it is $\lambda/4$ longer for the axis of polarisation corresponding to one of the interferometer arms. This has the effect of altering the interferometric phase for that copy of the light by $\pi/2$. As $\cos(\phi - \pi/2) \equiv \sin(\phi)$, the intensity of this copy of the light is now proportional to the sine of the phase, as we wanted.

There is an issue with using quarter wave plates in FSI, however. These elements have exactly $\lambda/4$ relative phase shift at one specific wavelength only. As widely tuneable lasers can vary their frequencies by as much as 10%, the relative phase shift between polarisations will vary significantly throughout the FSI measurement. Correction for non-perfect quarter wave plate phase shifts arising from non-perfect quarter wave plate alignment is common practice in fixed frequency interferometery [40] and these methods can be used to correct for the non-ideal performance of quarter waveplates throughout an FSI measurement.

The intensity from these two copies of the light may be written as

$$I_a = p_a + q_a \cos(\phi) \tag{2.2.1}$$

$$I_b = p_b + q_b \sin(\phi) \ , \tag{2.2.2}$$

which are rearranged to give

$$(I_a - p_a)/q_a = \cos(\phi)$$

$$(I_b - p_b)/q_b = \sin(\phi) \ .$$

The interferometric phase, $\phi$, may therefore be calculated from the measured intensities as

$$\phi = \arctan\left[\frac{(I_b - p_b)/q_b}{(I_a - p_a)/q_a}\right] \ .$$

As we know the signs of the numerator and denominator in this arc tangent calculation, a four quadrant arc tangent may be used in order to calculate the phase modulo $2\pi$.

### 2.2.2 Hilbert transform method

This section describes a method for calculating interferometric phase from the intensity output of an interferometer recorded during a laser frequency sweep. This can be used as a preliminary analysis step for many of the distance measurement methods described in this

thesis.

The method is based upon the Hilbert transform, which is a commonly used operation in signal processing. It is well understood theoretically [10, 11] and is straightforward to compute, as follows: The Hilbert transform, $\mathcal{H}[s(t)]$, of a signal, $s(t)$, may be computed using a forward and reverse Fourier transform, multiplying the signal with a Hilbert window in frequency space,

$$\mathcal{H}[s(t)] = \mathcal{F}^{-1}[\mathcal{F}[s(t)]H(\omega)] \ ,$$

where $\mathcal{F}$ and $\mathcal{F}^{-1}$ denote forwards and backwards Fourier transforms respectively, the Hilbert window is defined as

$$H(\omega) = -i\,\mathrm{sgn}(\omega) \ ,$$

and the sgn function is defined as

$$\mathrm{sgn}(x) = \begin{cases} -1, & x < 0 \\ 0, & x = 0 \\ +1, & x > 0 \end{cases} \ .$$

Examples of the Hilbert transform used for FSI analysis may be found in the following papers [2, 59].

The Hilbert transform has the following key property which allows us to use it to calculate phase: For a signal of the form $s(t) = b(t)\cos\phi(t)$, if the spectra of $b(t)$ is restricted to a range of frequencies that is lower than, and does not overlap the spectra of $\cos\phi(t)$ i.e. there exists some $\omega_r$ such that

$$\mathcal{F}[b(t)] = 0 \text{ for } |\omega| > \omega_r \tag{2.2.3a}$$

$$\mathcal{F}[\cos\phi(t)] = 0 \text{ for } |\omega| < \omega_r \ , \tag{2.2.3b}$$

then the Hilbert transform of this signal is

$$\mathcal{H}[b(t)\cos\phi(t)] = b(t)\sin\phi(t) \ . \tag{2.2.4}$$

I will now show how to use this property to calculate interferometric phase from the recorded intensity during a laser frequency sweep.

By comparison with Eqn. (2.1.6) the intensity signal recorded in a laser frequency sweep may be expressed as

$$s_0(t) = a(t) + b(t)\cos\phi(t) \ , \tag{2.2.5}$$

where $a(t)$ and $b(t)$ are functions of time, to take account of variations of the amplitude of the beam from each arm of the interferometer.

If the spectra of the first and second terms on the right hand side of Eqn. (2.2.5) are sufficiently distinct, i.e. if there exists some $\omega_s$ such that

$$\mathcal{F}[a(t)] = 0 \text{ for } |\omega| > \omega_s \tag{2.2.6a}$$

$$\mathcal{F}[b(t)\cos\phi(t)] = 0 \text{ for } |\omega| < \omega_s \ , \tag{2.2.6b}$$

then the signal may be high pass filtered to get

$$s_{hpf}(t) = b(t)\cos\phi(t) \ ,$$

which is in a suitable form to make use of the Hilbert transform relationship from Eqn. (2.2.4). I show in appendix B that if it is possible to high pass filter the signal in this way, then the conditions required for Eqn. (2.2.4) to hold are automatically satisfied. i.e. if there exists an $\omega_s$ that satisfies Eqn. (2.2.6) one can always find an $\omega_r$ that satisfies Eqn. (2.2.3).

Fluctuations in the terms $a(t)$ and $b(t)$ due to variations of laser intensity generally consist of low frequencies when compared to the interferometric signal $\cos\phi(t)$. In this case the spectra of $a(t)$ and $b(t)\cos\phi(t)$ will be distinct as required. For many FSI setups, including those used to test the new FSI methods later in this thesis, it will be possible to separate the two terms in this way.

The high pass filter can be performed with a forwards and reverse Fourier transform,

multiplying by the filter window, $W(\omega)$, in frequency space

$$s_{\text{hpf}}(t) = \mathcal{F}^{-1}[\mathcal{F}[s(t)]W(\omega)] \ ,$$

where the filter window is

$$W(\omega) = \begin{cases} 0, & |\omega| < \omega_s \\ 1, & |\omega| \geq \omega_s \end{cases} \ .$$

The Hilbert transform of $s_{hpf}(t)$ is now calculated. It is often convenient, when calculating the Hilbert transform of a real signal, $s(t)$, to store the result in the imaginary part of the same signal. In this form, the signal is known as the *analytic signal*, $\hat{s}(t)$, defined as

$$\hat{s}(t) = s(t) + i\mathcal{H}[s(t)] \ .$$

As the Fourier transform is a linear operation, i.e.

$$\mathcal{F}[aA(\omega) + bB(\omega)] = a\mathcal{F}[A(\omega)] + b\mathcal{F}[B(\omega)] \ ,$$

the analytic signal may be calculated by multiplying the real signal's Fourier transform by the following window in frequency space

$$1 + iH(\omega) = 1 + \text{sgn}(\omega) \ , \tag{2.2.7}$$

where the 1 gives the original, real signal back in the real part of the result, and the $iH(\omega)$ gives the Hilbert transformed signal in the imaginary part of the result.

Furthermore, to reduce computation time, it is possible to apply the high pass filter and compute the Hilbert transform using only one set of forwards and reverse Fourier transforms. This is done by multiplying by both the filter window and the Hilbert window at the same time in frequency space.

To review, the complete calculation, starting from the original signal, $s_0(t)$, from Eqn. (2.2.5),

is

$$\hat{s}(t) = \mathcal{F}^{-1}[\mathcal{F}[s_0(t)]W(\omega)(1 + iH(\omega))].$$

Using the above results, the right hand side is rewritten,

$$\begin{aligned}
\hat{s}(t) &= \mathcal{F}^{-1}[\mathcal{F}[s_0(t)]W(\omega)(1 + iH(\omega))] \\
&= \mathcal{F}^{-1}[\mathcal{F}[s_0(t)]W(\omega)] + i\mathcal{F}^{-1}[\mathcal{F}[s_0(t)]W(\omega)H(\omega)] \\
&= \mathcal{F}^{-1}[\mathcal{F}[s_{hpf}(t)]] + i\mathcal{F}^{-1}[\mathcal{F}[s_{hpf}(t)]H(\omega)] \\
&= s_{hpf}(t) + i\mathcal{H}[s_{hpf}(t)] \\
&= b(t)\cos\phi(t) + i\mathcal{H}[b(t)\cos\phi(t)] \\
&= b(t)(\cos\phi(t) + i\sin\phi(t)) \ .
\end{aligned}$$

It is a straightforward operation to calculate $\phi(t)$ from this analytic signal, by taking the arc tangent of its real and imaginary components,

$$\begin{aligned}
\phi(t) &= \arctan\left(\frac{\mathrm{Im}[\hat{s}(t)]}{\mathrm{Re}[\hat{s}(t)]}\right) \\
&= \arctan\left(\frac{b(t)\sin\phi(t)}{b(t)\cos\phi(t)}\right).
\end{aligned}$$

As with quadrature readout, the signs of the numerator and denominator in the arc tangent are known and thus a four quadrant arc tangent may be used to calculate the phase angle modulo $2\pi$ radians.

An important point to note about this method of phase calculation is that it requires the phase to vary monotonically. If the phase does not vary monotonically, then the $\cos\phi(t)$ part of the signal must necessarily contain zero frequency components, and therefore the condition of Eqn. (2.2.3) cannot be satisfied and the Hilbert transform method does not work. In FSI, we ensure that the phase curve is monotonic by sweeping the laser's frequency quickly and monotonically, such that most of the phase change is due to the changing laser frequency, rather than any changing distance.

The phase must also vary in a known direction, as the Hilbert transform method cannot

determine this: It will always calculate an increasing phase. In an FSI measurement this is not a problem, as the majority of the phase change should be due to the changing laser frequency, which is under our control. If the laser frequency was increased during the measurement, no changes need to be made, and if the laser frequency was decreased during the measurement, this should be taken account of by multiplying the calculated phases by -1.

A useful mathematical result regarding noise when using the Hilbert transform for phase calculation is given by Tretter [62], who shows that, in the limit of a high signal to noise ratio, an additive intensity noise (such as electrical noise on the photodiode, in our case) creates an equivalent additive noise on the phase as calculated using the Hilbert transform.

### 2.2.3 Unwrapping phase

By observing the intensity of the interference pattern, the absolute phase, $\phi$, can be calculated modulo $2\pi$ using the methods described above. The fact that it is calculated modulo $2\pi$ can be represented by splitting $\phi$ into two parts: one, $2\pi f$, representing the measured fractional phase modulo $2\pi$ and the other, $2\pi N$, representing the (unknown) integer multiple of $2\pi$ that makes up the remainder of $\phi$, giving

$$\phi = 2\pi \left(N + f\right) \ , \tag{2.2.8}$$

where $N$ is an integer and $f$ is a real number in the interval $[0, 1)$.

Phase, being an angular quantity, is commonly expressed in units of radians. In this thesis it will be more convenient to express phase in units of *cycles*, where one cycle is equal to $2\pi$ radians. Thus, if we instead consider phase, $\phi'$, expressed in units of cycles, we have $\phi' = N + f$, as $N$ and $f$ are in units of cycles. As well as removing the need for a $2\pi$ constant in numerous equations this convention shall prove particularly useful in chapter 5, which contains many equations where a phase is rounded to the nearest $2\pi$ radian multiple: It is simpler to consider instead rounding to the nearest integer multiple, with phase expressed in units of cycles.

Substituting this two component phase, Eqn. 2.2.8, into the model, Eqn. (2.1.5), gives the following:

$$N_n + f_n = \frac{D_n \nu_n}{c} \ . \tag{2.2.9}$$

We now have an equation describing the *wrapped phase*, $f_n$. The $n$ subscripts index the multiple consecutive phase measurements that are usually made in an FSI measurement. In a sense they are a short-hand, e.g. $f_n \equiv f(t_n)$, $D_n \equiv D(t_n)$, i.e. they indicate the sampled value of a quantity at a time $t_n$.

If we know that the absolute phase changes continuously with time, then by looking for discontinuities in the wrapped phase, a phase unwrapping algorithm can calculate the *unwrapped phase*, $u_n$, to be

$$u_n = f_n + N_n - N_0 \ , \tag{2.2.10}$$

where the phase has been unwrapped starting from the first data point, and $N_0$, the unknown integer phase offset at this point, represents what is now a single unknown phase offset for the whole data set. Note also, that although the phase is unwrapped starting from the first data point, this does not imply that $u_0 = 0$; the unwrapped phases retain the same fractional component as the wrapped phases. Substituting Eqn. (2.2.10) into Eqn. (2.2.9) we get an equation for the unwrapped phase,

$$N_0 + u_n = \frac{D_n \nu_n}{c} \ . \tag{2.2.11}$$

Here we have manipulated and tidied up the definition of absolute phase that we started this subsection with, Eqn. (2.1.5), in order to make it easier to use later on. It describes unwrapped phase from an FSI measurement as the sum of a measured set of phase values, $u_n$, and an unknown offset, $N_0$, and equates this to be proportional to the product of interferometer OPD, $D_n$, and laser frequency, $\nu_n$.

## 2.3 Notation

In later chapters this thesis considers interferometric systems that use two frequency swept lasers and/or more than two interferometers. In order to use a single set of notation throughout, the previously used notation is extended here to accommodate these multiple laser, multiple interferometer systems.

In order to cope with systems that have two lasers in a logical manner, quantities associated with the first laser are written as before, but quantities associated with the second laser are written with a bar above them. For example, the frequency of the first laser is written, as before, as $\nu$, but the frequency of the second laser is written as $\bar{\nu}$. The unwrapped phase measured with the second laser is written as $\bar{u}$, and the unknown phase offset associated with these phase measurements is written as $\bar{N}_0$.

In order to deal with systems containing multiple interferometers a superscript is used to indicate the interferometer which the symbol is associated with. For example, $D^1$ is now the OPD of the first interferometer and $D^2$ is the OPD of the second interferometer.

Using a combination of the bar notation and the numbered superscripts it is possible to indicate which laser and which interferometer a particular symbol is associated with. For example, $N_0^2$ is the unknown phase offset from the first laser in the second interferometer, and $\bar{u}_{100}^3$ is the 101st data point (counting from 0) of the unwrapped phase from the second laser in the third interferometer.

This notation may be used to write a single expression that represents multiple equations. Instead of indicating specific interferometers by writing for example, $D^1$ or $D^2$, we may write $D^i$, which indicates that this particular statement is true for all interferometers. Similarly, instead of explicitly indicating which laser a particular quantity relates to by writing for example $\nu$ or $\bar{\nu}$, a tilde, $\tilde{\nu}$, is used to indicate that this expression is true for both lasers. For example, this notation may be used to replace the following four equations for a two laser, two interferometer system;

| | First Laser | Second Laser |
|---|---|---|
| Reference Interferometer | $N_0^1 + u_n^1 = \frac{D_n^1 \nu_n}{c}$ | $\bar{N}_0^1 + \bar{u}_n^1 = \frac{D_n^1 \bar{\nu}_n}{c}$ |
| Measurement Interferometer | $N_0^2 + u_n^2 = \frac{D_n^2 \nu_n}{c}$ | $\bar{N}_0^2 + \bar{u}_n^2 = \frac{D_n^2 \bar{\nu}_n}{c}$ |

with the following single equation;

$$\tilde{N}_0^i + \tilde{u}_n^i = \frac{D_n^i \tilde{\nu}_n}{c} \ . \tag{2.3.1}$$

# Chapter 3

# Review of interferometric methods

The previous chapter described interferometry in a somewhat abstract manner. This chapter describes several specific examples of well known interferometric methods. This will allow the reader to compare these with the new FSI methods that will be described later on. It will also provide examples of the concepts and notation introduced in the previous chapters.

I will start with methods that use fixed wavelength lasers, and move on to FSI methods, which use variable wavelength lasers.

Other reviews of interferometric measurement methods may be found in [3, 13]. A brief review of some unusual absolute distance measurement methods may be found in [37].

## 3.1 Single wavelength

Topics relating to interferometry with a single laser of fixed wavelength have already been introduced at various places in previous chapters: The underlying concepts of interferometry were described in section 1.2, the basic arrangement of optics was illustrated in Fig. 2.1, a method for calculating interferometric phase was described in section 2.2.1 and a method for unwrapping a sequence of phase measurements was described in section 2.2.3.

A fixed, single wavelength interferometer makes repeated phase measurements in order

to determine the displacement of a reflective target along the line of a laser beam. The information obtained from these repeated phase measurements may be expressed mathematically, making use of the model that was described in section 2.1. The final result of that model, once phase calculation and unwrapping has been included, was Eqn. (2.2.11),

$$N_0 + u_n = \frac{D_n \nu}{c} \ . \tag{3.1.1}$$

The $n$ subscript has been removed from $\nu_n$ here, as the method currently being considered keeps the laser wavelength fixed.

The displacement of the reflective target along the line of the laser beam between measurement $n = f$ and $n = 0$, $(D_f - D_0)$, may be calculated from the phases recorded for these measurements as follows

$$\begin{aligned}
(N_0 + u_f) - (N_0 + u_0) &= \frac{D_f \nu}{c} - \frac{D_0 \nu}{c} \\
u_f - u_0 &= \frac{(D_f - D_0)\nu}{c} \\
D_f - D_0 &= (u_f - u_0)\frac{c}{\nu} \\
\Delta D &= \Delta u \frac{c}{\nu} \ ,
\end{aligned}$$

where an upper case $\Delta$ is used to indicate a change in a quantity, for example $\Delta D = D_f - D_0$.

However, no rearrangement of Eqn. (3.1.1) can calculate the absolute value of $D_n$ in terms of only known quantities. I argued in section 1.2 on general grounds that a distance measurement system using a periodic measurement signal such as light of a single fixed wavelength would be unable to calculate absolute distance. Here we see that for this specific example this is the case: We cannot calculate absolute distance in this system because we do not know $N_0$, the integer number of cycles the measurement signal goes through whilst travelling the measurement distance.

Some key sources of uncertainty in interferometric measurements are uncertainties in the measured phases, $u_n$, and in the laser frequency, $\nu$. There is also the uncertainty in

the refractive index of the medium through which the laser beam propagates (usually air), which was mentioned in section 1.3.2 but is not considered further in this thesis. To see the impact of uncertainty in $u$ and $\nu$ upon the measured displacement, a propagation of errors calculation is performed. This is done , both here and elsewhere, using the Gaussian error propagation formula,

$$\sigma_{f(a,b,...)} = \frac{\partial f(a,b,...)}{\partial a}\sigma_a \oplus \frac{\partial f(a,b,...)}{\partial b}\sigma_b \oplus ... \ ,$$

where the symbol $\oplus$ denotes a quadrature sum, defined by $A \oplus B = \sqrt{A^2 + B^2}$ and $\sigma_X$ denotes the uncertainty in $X$. Using this method, the measurement uncertainty on $\Delta D$ is calculated as

$$\sigma_{\Delta D} = \frac{c}{\nu}\sigma_{\Delta u} \oplus \Delta D\frac{\sigma_\nu}{\nu} \ . \tag{3.1.2}$$

Re-writing this with typical numerical values of $\nu = 200$ THz, and $\Delta D = 1$ m, this becomes

$$\sigma_{\Delta D} = 1.5 \times 10^{-6}\sigma_{\Delta u} \oplus 1\frac{\sigma_\nu}{\nu} \ .$$

To give a sense of scale, measurements of phase may typically reach uncertainties of $10^{-2}$ or $10^{-3}$ of a fringe. Relative uncertainties in laser vacuum wavelength can be made very low with 1 in $10^7$ being easily achievable. Much higher relative precisions are attainable, but even at the level of 1 in $10^7$, distance measurement uncertainty in air will be dominated by uncertainty of the refractive index of air, so when measuring distance in air there is little to gain by using a laser with a lower wavelength uncertainty.

A practical advantage of this method is its relative simplicity when compared to other methods described in this chapter. The major disadvantage is its unforgiving nature: any errors in unwrapping the phase (such as a gap in the data caused by a blockage of the laser beam) mean the measurement must be restarted.

A review of single wavelength interferometry is given in [12].

## 3.2 Multiple wavelength

Dual wavelength interferometry is a good example of how more information about the measured length may be extracted with the use of a second laser source, which is also the main principle behind Dynamic FSI. Dual wavelength interferometry may also serve as an example of a measurement method with a discretised error, something that both Dynamic FSI and Cascaded FSI make use of.

An example of a dual wavelength interferometric measurement system is described in [23]. Examples of multiple wavelength interferometry systems are described in [44, 46, 17].

### 3.2.1 Dual wavelength

The measurement setup for a dual wavelength measurement is similar to that of single wavelength interferometry, but has the practical disadvantage that it is more complex: A second light source is required, along with a method of combining and separating out the two wavelengths of light. There are many possible ways of doing this, including time division multiplexing (simply alternating the wavelengths used), frequency division multiplexing (modulating each wavelength with a different frequency), and using the wavelength of the light itself to separate out light of different frequencies using a dichroic mirror.

Once light has been multiplexed, sent into the interferometer and demultiplexed at the output, the interferometric phase corresponding to each of the two wavelengths is measured. This may be done using the same methods as used for single wavelength interferometry. Using the interferometer model, Eqn. (2.3.1), we can represent the information gained from these two phase measurements as

$$\tilde{N} + \tilde{u} = \frac{D\tilde{\nu}}{c} \, . \tag{3.2.1}$$

Recall the tilde notation - e.g. $\tilde{u}$ - introduced in section 2.3, which indicates the equation is

valid for both lasers. The $n$ subscripts have been dropped for this section, as here we won't be concerned with a series of phase measurements, but only one pair of phase measurements, one for each laser. The symbol $u$ shall still be used to denote the phase measured here.

By combining the phase measurements from both lasers it is possible to perform a measurement with a longer ambiguity length than single wavelength interferometry. This is done by taking the difference of the two measured phases, $u$ and $\bar{u}$. To see what this tells us, take the difference of the two equations represented by Eqn. (3.2.1)

$$(N + u) - (\bar{N} + \bar{u}) = \frac{D\nu}{c} - \frac{D\bar{\nu}}{c} ,$$

and rearrange this to give

$$(N - \bar{N}) + (u - \bar{u}) = \frac{D(\nu - \bar{\nu})}{c} , \tag{3.2.2}$$

which may be rewritten as

$$\Delta N + \Delta u = \frac{D\Delta\nu}{c} , \tag{3.2.3}$$

by defining

$$\Delta N = N - \bar{N} - w ,$$
$$\Delta u = u - \bar{u} + w ,$$
$$\Delta\nu = \nu - \bar{\nu} ,$$

where the $w$ term, defined as

$$w = \begin{cases} 0, & u - \bar{u} \geq 0 \\ 1, & u - \bar{u} < 0 \end{cases} ,$$

is used to map $\Delta u$ into the range $[0, 1)$, as, with both $u$ and $\bar{u}$ being in the range $[0, 1)$, $(u - \bar{u})$ is in the range $(-1, 1)$. Note that including $w$ with opposite sign in the definitions of $\Delta N$ and $\Delta u$ means that this term cancels out in Eqn. (3.2.3).

Note that Eqn. (3.2.3) is in the same form as Eqn. 3.1.1 from single wavelength interferometry, with the only difference being that we have replaced various quantities with the difference of these quantities between the two lasers. Therefore it is as if we were measuring the interferometric phase corresponding to the combined, or *synthetic* frequency[1] $\Delta\nu = \nu - \bar{\nu}$. This synthetic frequency will be smaller than either of the real frequencies that are being used, and so the measurement will have a longer ambiguity length than single frequency interferometry; however it will also have a lower precision. This is an example of the trade-off between precision and ambiguity range mentioned in section 1.2. By choosing the two wavelengths used, the ambiguity length can be fixed at a desired value from micrometers to meters in length [23]. Despite the lowered precision, there are two reasons why a longer ambiguity range is useful.

Firstly, it can be beneficial for phase unwrapping: The phase can still be unwrapped with a larger distance change between measurements. This is useful for interferometers used to measure the shape of a surface, where phase is measured at multiple locations on a surface using, for example, a CCD detector, and is unwrapped with respect to adjacent pixels. Here, dual wavelength interferometry is capable of measuring steeper height changes than single wavelength interferometry.

Secondly, a longer ambiguity range makes it more feasible to perform a kind of absolute distance measurement with the interferometer. If the OPD can be measured by other means with an uncertainty significantly lower than half an ambiguity range then the interferometer measurements may be used to give a higher accuracy measurement.

Making an a-priori measurement of the OPD effectively gives an estimate of the absolute value of the interferometric phase. We could use it to estimate the interferometric phase corresponding to either laser frequency, or the synthetic phase corresponding to the synthetic frequency. If we estimate the length to be $\hat{D}$, then an estimate of the integer part of the

[1] It is common in discussions of dual wavelength interferometry and related topics to refer instead to a synthetic *wavelength*, $\Lambda = c/\Delta\nu = \lambda\bar{\lambda}/(\bar{\lambda} - \lambda)$. In this thesis it will often be algebraically more convenient to go against the more common convention and refer to a synthetic *frequency*.

synthetic phase, $\Delta\hat{N}$, may be calculated as follows;

$$\Delta\hat{N} = \frac{\hat{D}\nu}{c} - \Delta u \ ,$$

where the hats on $\Delta\hat{N}$ and $\hat{D}$ are to emphasise that these are estimates of the corresponding quantity that may be subject to experimental errors. Later, improved, estimates will be made of the same quantities and these will be distinguished by adding an extra hat, e.g. $\Delta\hat{\hat{N}}$.

This is an estimate of a discrete, integer quantity. If the estimate has an uncertainty significantly less than $\pm 0.5$, with a high confidence level, then rounding this estimate to the nearest integer will reliably (i.e. with high probability) produce the *exact* value for this integer quantity. Therefore we define a second estimator for $\Delta N$ which rounds the initial estimator to the nearest integer,

$$\Delta\hat{\hat{N}} = ||\Delta\hat{N}|| \ ,$$

where the double brackets, e.g. $||x||$, denotes the 'nearest integer' function which rounds its operand, $x$, to the nearest integer value.

Assuming that the rounding operation correctly calculated the exact value for $\Delta N$, its result may be used to calculate a refined estimate for the absolute value of the OPD,

$$\hat{\hat{D}} = \left(\Delta\hat{\hat{N}} + \Delta u\right)\frac{c}{\Delta\nu} \ . \tag{3.2.4}$$

The uncertainty on this value due to uncertainty on $u$ and $\nu$, and assuming that the rounding step calculated the correct value for $\Delta N$, is,

$$\sigma_{\hat{\hat{D}}} = \frac{\sqrt{2}}{\Delta\nu}\left(c\sigma_u \oplus D\sigma_\nu\right) \ , \tag{3.2.5}$$

where to simplify the above, it has been assumed that $\sigma_u = \sigma_{\bar{u}}$ and $\sigma_\nu = \sigma_{\bar{\nu}}$.

A similar procedure could in theory be performed for single wavelength interferometry, but it would be less practical, as it would be harder to satisfy the requirement that $\sigma_{\Delta\hat{N}} <$

0.5 with a high confidence level, due to the shorter ambiguity range of single wavelength interferometry.

### 3.2.2 Multiple wavelength

It is possible to go a step further with this method, to further refine the measurement of the OPD. The improved length estimate, $\hat{\hat{D}}$, that was just obtained by dual wavelength interferometry in Eqn. (3.2.4) may be used as the initial length estimate to measure absolute length with single wavelength interferometry.

The value of $\hat{\hat{D}}$ may be used to estimate the integer part of the absolute phase corresponding to either of the real (i.e. not synthetic) laser frequencies: The integer part of the absolute phase corresponding to the first laser frequency may be estimated to be

$$\hat{N} = \frac{\hat{\hat{D}}\nu}{c} - u \; .$$

As before, this estimate of an integer quantity is rounded to the nearest integer to give the exact value (requiring that the error on the estimate is less than $\pm 0.5$),

$$\hat{\hat{N}} = ||\hat{N}|| \; .$$

This refined estimate for $N$ is then used to calculate the absolute value of the OPD according to the measured fractional phase, $u$,

$$\hat{\hat{D}} = \left(\hat{\hat{N}} + u\right) \frac{c}{\nu} \; .$$

The uncertainty on $\hat{N}$ due to uncertainty on $u$, $\bar{u}$, $\nu$ and $\bar{\nu}$ may be calculated to be

$$\sigma_{\hat{N}} = \left(\frac{\nu \oplus \bar{\nu}}{\nu - \bar{\nu}}\right) \left(\sigma_u \oplus \frac{D}{c}\sigma_\nu\right) \; , \tag{3.2.6}$$

where, to simplify the above, it is assumed that the magnitude of the uncertainties on $u$ and

$\bar{u}$ are equal, and therefore $\sigma_u = \sigma_{\bar{u}}$. The same assumption is made for the uncertainties on the laser frequencies; $\sigma_\nu = \sigma_{\bar{\nu}}$.

The uncertainty on $\hat{\hat{D}}$ due to uncertainty on $u$ and $v$ is

$$\sigma_{\hat{\hat{D}}} = \frac{1}{\nu}\left(c\sigma_u \oplus D\sigma_\nu\right) \ . \tag{3.2.7}$$

The measurement process which calculates $\hat{\hat{D}}$ now contains two 'rounding steps' where an estimate of an integer quantity is rounded to the nearest integer. The uncertainty on the initial estimates $\hat{\Delta N}$ and $\hat{N}$ should be less than $\pm 0.5$ with a high confidence level in both cases.

The choice of laser frequencies used here is important. This fixes the size of the synthetic frequency. A small synthetic frequency leads to a large ambiguity range, and thus reduces the requirements on the initial length estimate, $\hat{D}$: It is easier to satisfy the requirement that $\sigma_{\Delta N} < 0.5$. However, note in Eqn. (3.2.6) the dependence on the synthetic frequency, which appears as the $\nu - \bar{\nu}$ term in the denominator of the first fraction. A small synthetic frequency will *increase* the uncertainty on $\hat{N}$, making it harder to satisfy the requirement that $\sigma_{\hat{N}} < 0.5$. Thus the choice of synthetic frequency is a trade-off between satisfying the uncertainty requirements for the first and the second rounding steps.

It is possible to relax these requirements, however, with an interferometer system that uses more than two lasers of different frequencies. A synthetic frequency can be associated with any pair of laser frequencies, and the preceding steps may be repeated in order to obtain successively more accurate estimates of the OPD corresponding to successively larger synthetic frequencies. Adding in more stages to the calculation relaxes the uncertainty requirements on each rounding step. In practice, when using multiple wavelength interferometry to determine lengths of the order 1 m, three wavelengths may be regarded as a practical minimum number, as otherwise the requirements on the initial length estimate are hard to meet [44].

This process has illustrated an important concept that is the basis of Cascaded FSI, that

of discretised errors. Throughout this multi-stage process that proceeds by estimating integer quantities such as $\Delta N$ and $N$ and then correcting these estimates using the nearest integer function, $||x||$, there is no build up of error, as long as the initial estimate of the integer quantity is correct to within $\pm 0.5$ at each step. This is in contrast to a multi-stage process with continuous errors at each stage, where there will be a build-up of errors. Of course, for this discretised error process, each step increases the chance that an integer quantity will be estimated wrong by more than $\pm 0.5$. I shall call this a discrete error. Thus there is a build up of the potential for making a discrete error. That is to say: the probability of making a discrete error at at least one stage will increase when more stages are added. But by making the probability of a discrete error at each stage sufficiently small, the probability of a discrete error overall may be kept to an acceptably low level. It is also possible to add additional checks in order to reject any measurements that contain a discrete error. A simple example would be to simply measure twice and reject any pair of measurements that differ by more than a specified tolerance.

An everyday example of the power and reliability of systems with discretised errors is digital communications and data storage. Data stored on computers is represented by sequences of discrete binary values; 1's and 0's. However these are both stored and transmitted as analogue quantities such as analogue voltages. Even so, we expect files containing many billions of bits to be routinely transmitted without making a single discrete error. This is achieved by first rounding the analogue voltages to the nearest expected value (say either 0 V or 5 V, for example) upon reading or receiving data, and additionally applying a whole host of checks that are sophisticated versions of the simple 'measure it twice' check suggested earlier. The entire process works because it carefully manages the discretised errors involved, in order to reduce the probability of a discrete error to be vanishingly small.

## 3.3 Single laser FSI

The previous sections described interferometric methods that used fixed frequency lasers. As was discussed in section 1.2, the periodicity of the electromagnetic wave in these methods means that they can only make ambiguous measurements of distance. This section describes the first true[2] absolute distance measurement method of this chapter: FSI using a single laser. It was argued in section 1.2 that the non-periodic signal of a frequency swept laser may be used to make an absolute distance measurement, and this section describes explicitly how this may be done.

An FSI measurement may be made using the same physical arrangement of optics as single wavelength, fixed frequency interferometry, but with the fixed frequency laser replaced with a frequency swept laser. A measurement is made by ramping the laser frequency in a continuous manner and recording the intensity on the photodiode as this is done. The distance being measured must be held constant during this process. The interferometric phase throughout the duration of the frequency sweep is then calculated from the recorded intensity values, using, for example the Hilbert transform method described in section 2.2.2. The calculated phase values are then unwrapped, and the absolute distance to the target reflector may then be calculated from these unwrapped phase values. As a simplified pedagogical example, it may be calculated by taking the difference between the first and last phase values.

According to our model, the unwrapped phase values obey the relationship of 2.2.11, which I again re-write here with the minor modification of dropping the $n$ subscript on the $D_n$, as this distance is - for now - considered a constant for the duration of the measurement,

$$N_0 + u_n = \frac{D\nu_n}{c} \ . \tag{3.3.1}$$

The difference of the unwrapped phases at the ends of the frequency sweep, corresponding

[2]i.e. not requiring an a-priori knowledge of the OPD as dual wavelength interferometry does.

to $n = 0$ and $n = f$, is then calculated, and used to evaluate the OPD,

$$\begin{aligned}(N_0 + u_f) - (N_0 + u_0) &= \frac{D\nu_f}{c} - \frac{D\nu_0}{c} \\ u_f - u_0 &= \frac{D(\nu_f - \nu_0)}{c} \\ D &= c\frac{(u_f - u_0)}{(\nu_f - \nu_0)} \\ D &= c\frac{\Delta u}{\Delta \nu}\ . \end{aligned} \tag{3.3.2}$$

Thus, the absolute value of the OPD, $D$, may be calculated as the ratio of the unwrapped phase increase to the change in laser frequency. Alternatively, the distance may be calculated in a way that makes use of all the data by fitting a line to determine the slope of unwrapped phase vs laser frequency. How to precisely determine the change in laser frequency will be discussed later.

This may be contrasted to the method of displacement interferometry using a single fixed frequency laser, as described above in section 3.1. For the fixed frequency method the change in phase was recorded in order to determine the ratio of distance change to a fixed laser wavelength, $\lambda = c/\nu$. In FSI the situation has been reversed: A change in phase is recorded, as before, but here it is used to determine the ratio of frequency change to a fixed distance.

Compare Eqn. (3.3.2) with Eqn. (3.2.3), which describes length measurement with respect to a synthetic frequency in dual wavelength interferometry. In both cases the difference between two phases is taken. The difference between the two cases is that for FSI, as we've continuously swept the tuneable laser's frequency between $\nu_0$ and $\nu_f$, we may calculate the absolute value of the difference in phase corresponding to these two frequencies via phase unwrapping. Algebraically this means that the $N_0$ cancels out for FSI, in Eqn. (3.3.2), allowing an unambiguous length measurement to be made, whereas for dual wavelength interferometry there remain two separate unknown integer phase components, $N$ and $\bar{N}$, (as the phase cannot be unwrapped) and thus the length measurement remains ambiguous.

It has been stressed several times that in order to make an FSI measurement the laser's

frequency must be varied *continuously*. i.e. there should be no discontinuous jumps in the laser's frequency. This requirement comes from the fact that we must be able to unwrap the phase throughout the frequency sweep. Continuously varying a laser's frequency over a large range is a technically difficult feat to achieve, and lasers with this capability are very expensive compared to fixed frequency lasers with otherwise similar specifications. This is one of the major factors preventing more widespread use of the FSI technique to date.

The uncertainty in calculated distance according to Eqn. (3.3.2), due to uncertainty in measured phases and laser frequency values, may be shown to be

$$\sigma_D = \frac{\sqrt{2}}{\Delta\nu} \left( c\sigma_u \oplus D\sigma_\nu \right) \ .$$

Note that this is exactly the same as Eqn. (3.2.5) from the dual wavelength interferometry section. This is due to the fact that both FSI and dual wavelength interferometry calculate distance relative to a synthetic frequency. This synthetic frequency is the difference of two fixed laser frequencies for dual wavelength interferometry, and the difference between the initial and final tuneable laser frequencies for FSI. As for dual wavelength interferometry, the precision of the distance calculation improves when there is a larger synthetic frequency. But, unlike dual wavelength interferometry, there is no trade-off requirement for a higher precision a-priori measurement when a larger synthetic frequency is used. This leads to the desire for a large synthetic frequency in FSI measurements, corresponding to a large laser frequency sweep range, in order to maximise the precision of the measurement.

A disadvantage of this type of measurement is that it takes time for the laser to sweep its wavelength between the two end values. This means that the repetition rate of measurements is much lower than that in the previously described methods, where the limit is typically due to the bandwidth of the photodiode amplifier and associated readout electronics.

Examples of wavelength swept interferometry systems are described in [16, 22, 41, 47, 58].

### 3.3.1 Reference interferometer

Earlier it was mentioned that we must be able to determine the laser frequency change $\nu_0 - \nu_n$. A common method for doing this is to use a *reference interferometer*. This is an additional interferometer, of known OPD, that some fraction of the frequency swept laser light is diverted into. With this, we may perform FSI in reverse: Using the known distance, we may calculate the frequency change.

The intensity output of the reference interferometer is measured, and the unwrapped phase calculated from this. The information gained from both interferometers can be represented as

$$N_0^i + u_n^i = \frac{D^i \nu_n}{c} \, . \tag{3.3.3}$$

Combining the four equations represented by Eqn. (3.3.3) with the four possible combinations of $i = 1, 2$ and $n = 0, f$, we find

$$D^2 = D^1 \frac{(u_f^2 - u_0^2)}{(u_f^1 - u_0^1)} \, , \tag{3.3.4}$$

and thus the measured distance may be calculated relative to the known distance of the reference interferometer.

The disadvantage of doing this, however, is that the measurements are now performed relative to a physical length standard. These typically have lower stability than frequency standards and it is also harder to achieve traceable measurements with them. Cascaded FSI, as described in chapter 5, allows measurements to be made relative to a frequency standard, improving the accuracy and traceability of the measurement.

### 3.3.2 Drift errors

It was mentioned earlier that the measured distance should be kept constant during an FSI measurement, but this is never perfectly achievable in practice; the distance will always

change by some small amount. This failure of the assumption of constant distance creates an error, known as a *drift error*, which is described in this section.

The exact amount of drift error an FSI measurement is subject to will, of course, depend upon exactly how the data is analysed. I shall calculate here the drift error encountered when data is analysed using the simplified example presented above in Eqn. (3.3.2). This shall serve as a good indication of the drift error one may expect to encounter when using other analysis methods.

It will be useful to define the following quantities, being the average values of the interferometer OPD and laser frequency for the two points used in the analysis,

$$\langle \nu \rangle = (\nu_f + \nu_0)/2 \tag{3.3.5}$$

$$\langle D \rangle = (D_f + D_0)/2 \; . \tag{3.3.6}$$

Using these definitions, it can be shown that

$$c\frac{\Delta u}{\Delta \nu} = \langle D \rangle + \Delta D \frac{\langle \nu \rangle}{\Delta \nu} \; . \tag{3.3.7}$$

Compare this with the equivalent, Eqn. (3.3.2), where the distance was assumed to be constant. Note that Eqn. (3.3.7) reduces to Eqn. (3.3.2) when $\Delta D = 0$. But when $\Delta D \neq 0$ there is an additional term in Eqn. (3.3.7), which is the error in calculated OPD caused by the change in OPD during the laser frequency scan. This error is equal to the change in distance during the laser frequency sweep, magnified by the *drift error multiplier*, $\langle \nu \rangle / \Delta \nu$. The lasers used to take data for this thesis have frequency sweep ranges in the order of 10 THz around an average frequency of approximately 200 THz, making the drift error multiplier approximately 20. It is technically very difficult to achieve such a large sweep range, and so many tuneable lasers have frequency sweep ranges in the order of 100 GHz, in which case the drift error multiplier would be 2000.

Drift errors are clearly a major contributor to measurement errors in single laser FSI. To

minimise them it is desirable to use a laser that sweeps over a large frequency range. It is also beneficial if the laser performs this sweep rapidly, as this minimises the time available for the distance to change.

Due to the influence of drift errors, single laser FSI is less accurate than a dual fixed frequency interferometry system with the same synthetic wavelength. FSI does of course have the advantage of making a true absolute distance measurement, however.

### 3.3.3 Analysis with straight line fit

So far in this section I have only considered analysis of single laser FSI data using the first and last data points. This was done to simplify the explanation, however it is possible to make use of all the data points in the analysis: Combining two copies of Eqn. (3.3.3), one corresponding to the measurement interferometer ($i = 2$), and the other corresponding to the reference interferometer($i = 1$), one may obtain

$$u_n^1 = Ru_n^2 + \left(RN_0^2 - N_0^1\right) \ , \tag{3.3.8}$$

where $R = D^2/D^1$. This is in the canonical form for a straight line, $y = mx + c$, and therefore, by fitting a straight line to the recorded unwrapped phases from the measurement and reference interferometers, the ratio of interferometer OPDs may be calculated as the gradient, $R$, of this straight line fit.

## 3.4 Dual laser FSI

The problem of drift error in single laser FSI can be removed with the use of an additional frequency swept laser. This can provide an additional measure of the phase change of the interferometer, allowing us to distinguish between phase change caused by laser frequency variation, and phase change caused by a changing OPD. A dual laser FSI measurement is performed by making two simultaneous measurements of the same interferometer with two

different frequency swept lasers. As with dual wavelength interferometry, this requires a method to multiplex and demultiplex the two laser beams.

The information gained from these two simultaneous measurements may be summarised by again writing out the model, Eqn. (2.3.1) corresponding to this particular situation:

$$\tilde{N}_0 + \tilde{u}_n = \frac{D_n \tilde{\nu}}{c} \ .$$

The measured distance plus the drift error from each laser can be expressed with the analogue of Eqn. (3.3.7), written out here for the two laser system;

$$c\frac{\Delta\tilde{u}}{\Delta\tilde{\nu}} = \langle D \rangle + \Delta D \frac{\langle\tilde{\nu}\rangle}{\Delta\tilde{\nu}} \ .$$

A drift error free measurement may be made by combining the two equations this represents. In the simplest case, if the two lasers scan through exactly opposite frequency ranges (and therefore $\langle\nu\rangle = \langle\bar{\nu}\rangle$ and $\Delta\nu = -\Delta\bar{\nu}$), then adding together the above equation corresponding to each laser gives

$$\begin{aligned} c\frac{\Delta u}{\Delta\nu} + c\frac{\Delta\bar{u}}{\Delta\bar{\nu}} &= \langle D \rangle + \Delta D \frac{\langle\nu\rangle}{\Delta\nu} + \langle D \rangle + \Delta D \frac{\langle\bar{\nu}\rangle}{\Delta\bar{\nu}} && (3.4.1) \\ &= \langle D \rangle + \Delta D \frac{\langle\nu\rangle}{\Delta\nu} + \langle D \rangle + \Delta D \frac{\langle\nu\rangle}{-\Delta\nu} && (3.4.2) \\ &= 2\langle D \rangle \ . && (3.4.3) \end{aligned}$$

The last line contains no $\Delta D$ term, as it appeared with opposite sign in the two equations that were summed. This enables a measurement that is free of drift error. In practice it may not be possible to ensure both lasers tune over exactly opposite frequency ranges, in which case a weighted average may be employed in order to correctly cancel out the drift error terms. As this particular method of dual laser FSI is not used to make measurements in this thesis, the explicit equations for this need not be shown.

A drawback of this method is that, as with so many of the other methods, the extra measurement capability comes at the price of increased complexity. In addition to the

equipment required for single laser wavelength swept interferometry, another laser is required, together with a system for demultiplexing the interferometric signals from the two lasers.

Measurement systems using two simultaneously frequency swept lasers operating in the above manner have been described previously by, for example [20, 21, 55, 66]. These systems treat the measurement from each laser independently, however. Each of these independent measurements implicitly assumes a fixed OPD during the measurement, and the results are only combined afterwards in order to correct for this failed assumption.

In another paper [39] Hartmann et. al. describe a dual laser FSI based system that measures with respect to a synthetic wavelength. Measurement precision is limited in this system due to the large value of this synthetic wavelength.

None of these systems measures the OPD continuously throughout the FSI scan, and only give a single measured distance per scan. The one exception is the system described by Yang et. al. [66], however their 'slip-window' technique still calculates distance changes as the result of an error arising from the failed assumption of fixed OPD. Dynamic FSI completely avoids making this assumption.

# Chapter 4

# Dynamic FSI

This chapter describes Dynamic FSI, a distance measurement method that does not suffer from slow measurement rate or susceptibility to drift error, two limitations commonly seen in other FSI implementations.

As with other dual laser FSI systems, it simultaneously records the interferometric phase corresponding to two lasers with different frequency sweeps. The main difference from other systems is the way the recorded phases are analysed: This enables Dynamic FSI to calculate the continuously varying distance over the entire duration of the laser frequency sweep, whereas previous methods can calculate only a single distance measurement per sweep.

The sections making up this chapter are: the theory of the measurement method, in section 4.1, a numerical analysis of the method, in section 4.2, and finally an experimental analysis of the method, in section 4.3.

Material contained within this chapter relates to PCT/GB2011/051399; a patent pending invention held by Isis Innovation Limited (www.isis-innovation.com).

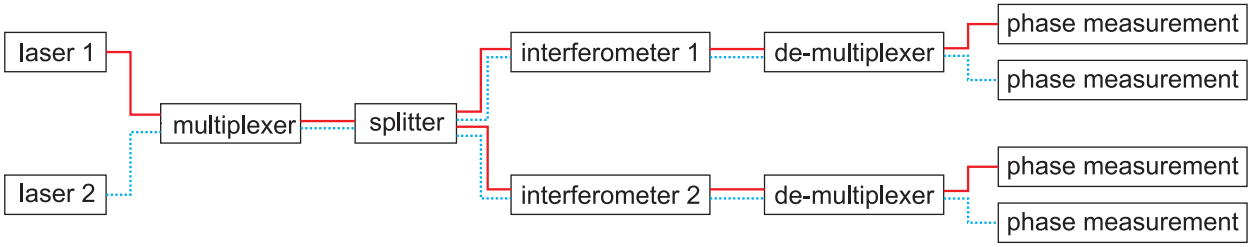


Figure 4.1: Schematic illustration of Dynamic FSI measurement setup

## 4.1 Method

The general setup required for making a Dynamic FSI measurement is shown schematically in Fig. 4.1. Light from a pair of lasers is combined and sent simultaneously into a pair of interferometers. The interferometric signals created by the two lasers are de-multiplexed such that they may be distinguished from each other. This may be done by physically separating out light from the two lasers, for example using orthogonal polarisations, or by separating the interferometric signals in electronics or software, for example by amplitude modulating each laser at different frequencies.

To make a measurement, the frequency of either one or both lasers is swept in a continuous manner whilst recording the four phases corresponding to the four combinations of laser and interferometer. There are many possible arrangements of optics which may achieve this, one of which is described in section 4.3.

The goal of the measurement is to determine the OPD of one of these interferometers, the *measurement interferometer*, relative to the known length of the other, reference interferometer. The remainder of this section describes how to analyse the interferometric phases recorded during the frequency sweep in order to reconstruct this distance ratio over the entire duration of the sweep.

The main data analysis steps performed in Dynamic FSI are summarised in Fig. 4.2. The reader may wish to refer back to this diagram from time to time whilst reading the relevant sections in the text.

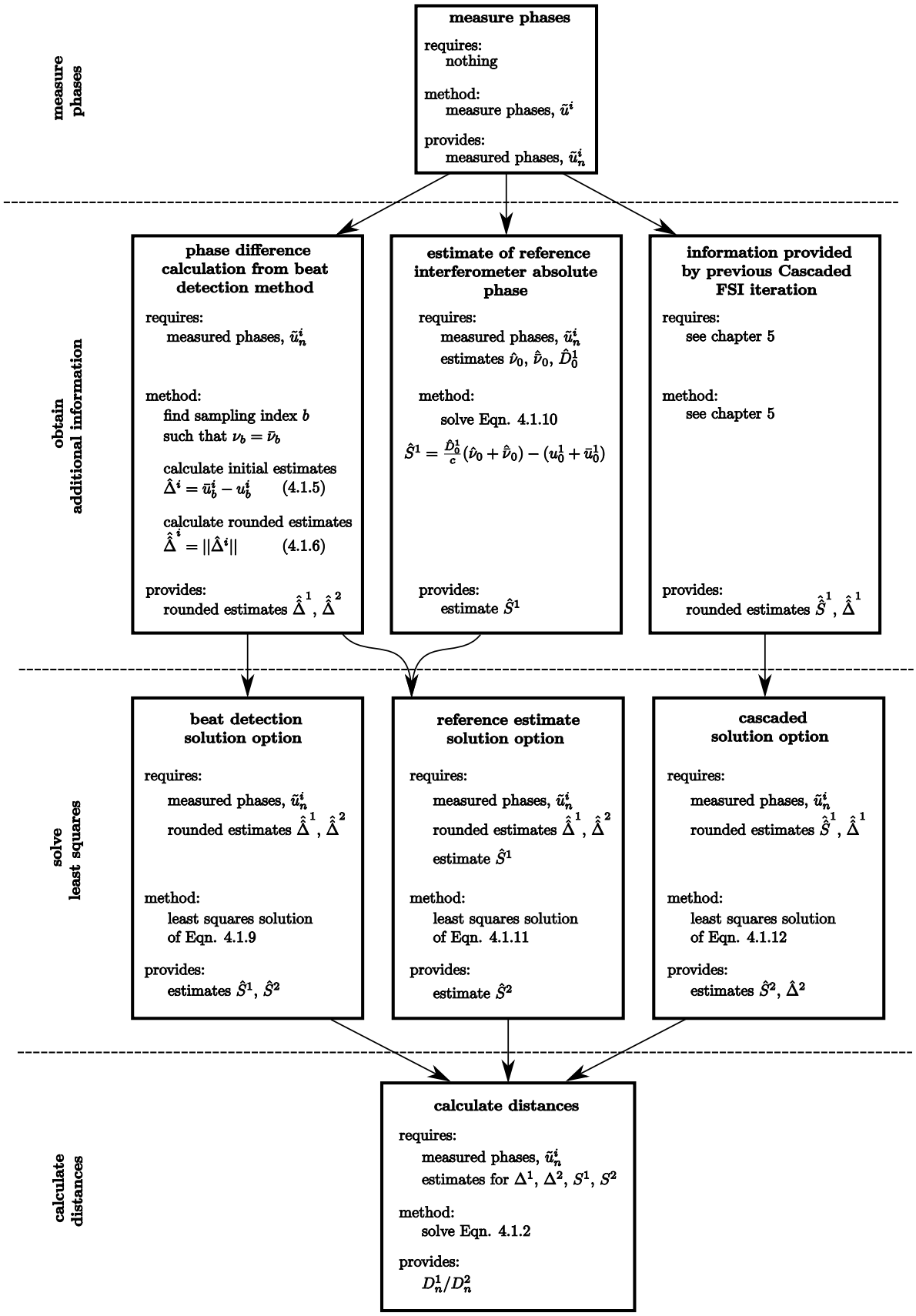


Figure 4.2: Summary of Dynamic FSI data analysis process

### 4.1.1 Distance calculation equations

The basis of Dynamic FSI is the model of Eqn. (2.3.1), which is written out here using the notation from section 2.3 for this two laser, two interferometer system,

$$\begin{array}{rll} & \text{First Laser} & \text{Second Laser} \\ \text{Measurement Interferometer} & N_0^2 + u_n^2 = (D_n^2\nu_n)/c & \bar{N}_0^2 + \bar{u}_n^2 = (D_n^2\bar{\nu}_n)/c \\ \text{Reference Interferometer} & N_0^1 + u_n^1 = (D_n^1\nu_n)/c & \bar{N}_0^1 + \bar{u}_n^1 = (D_n^1\bar{\nu}_n)/c \quad . \end{array} \tag{4.1.1}$$

Recall that the $n$ subscripts index simultaneous samplings of all four phases, $u_n^1$, $\bar{u}_n^1$, $u_n^2$ and $\bar{u}_n^2$; and also index the interferometer OPDs $D_n^1$ and $D_n^2$; and laser frequencies, $\nu_n$ and $\bar{\nu}_n$, at that sampling time.

We wish to calculate the OPD of the measurement interferometer relative to that of the reference interferometer at every sampling point, i.e. we wish to calculate $D_n^2/D_n^1$ for all $n$ in the data. Two expressions for this may be obtained immediately by dividing the entries on the first row of Eqns. (4.1.1) by the entries on the second row,

$$\frac{D_n^2}{D_n^1} = \frac{N_0^2 + u_n^2}{N_0^1 + u_n^1} \ , \tag{4.1.2a}$$

$$\frac{D_n^2}{D_n^1} = \frac{\bar{N}_0^2 + \bar{u}_n^2}{\bar{N}_0^1 + \bar{u}_n^1} \ . \tag{4.1.2b}$$

However, the unknown values on the right hand side, in the form of the four *integer phase offsets*, $\tilde{N}_0^i$, must be determined before the above equations can be evaluated. This may be done by combining the above two equations to eliminate $D_n^1$ and $D_n^2$,

$$\frac{N_0^2 + u_n^2}{N_0^1 + u_n^1} = \frac{\bar{N}_0^2 + \bar{u}_n^2}{\bar{N}_0^1 + \bar{u}_n^1} \ , \tag{4.1.3}$$

to obtain an over-constrained system of equations that may be solved, using the method of least squares, to determine the integer phase offsets. Once determined, the values are substituted into Eqn. (4.1.2), allowing the measurement interferometer OPD to be evaluated at every data sample.

The key difference between this and previous dual laser FSI methods such as that described in section 3.4 is the calculation of the integer phase offsets. Another crucial difference is that in Dynamic FSI, the OPD is never assumed to be constant. Avoiding making this assumption allows this method to accurately measure a changing OPD.

Note that there are two Eqns., (4.1.2a) and (4.1.2b), that may be used to calculate the interferometer distance ratio once the integer phase offsets are known. Such data redundancy is a requirement for the method of least squares, which will in some sense minimise the discrepancy between these two equations. A simple average of the two is a good way of using all the available data to calculate $D_n^2/D_n^1$.

Although the method as presented above seems quite straightforward, the 'devil in the detail' lies in the least squares solution of Eqn. (4.1.3): The rest of this section is dedicated to describing how this may be done successfully.

### 4.1.2 Solution options

Although Eqn. (4.1.3) easily satisfies the least squares condition that there be more equations (one per $n$ value) than unknowns (the four integer phase offsets), this alone does not guarantee that least squares will be able to accurately determine values for the integer phase offsets. A common problem in least squares is that of a *poorly constrained* system. This occurs when it is possible to vary the unknowns in such a way that the observables change very little, or not at all. In this case, least squares is unable to determine an accurate estimate for the values of the unknowns along this degree of freedom. In section 4.2 it will be shown that the least squares problem of Eqn. (4.1.3) is a poorly constrained system. This problem is remedied by determining the value or relative values of some of the integer phase offsets by other means, and including this additional information in the least squares solution, making it a well constrained problem. This section describes three methods, referred to as *solution options*, for doing this.

**'Beat detection' solution option**

If the frequencies of the two lasers are equal at some point in time, then the absolute phase corresponding to each laser will be the same in any given interferometer at that time. This fact may be used to find the differences of the integer phase offsets; $N^i - \bar{N}^i$. As this shall be a key way of determining the required extra information about the integer phase offsets, it shall be useful to consider these in terms of sum, $S^i$, and difference, $\Delta^i$, components, defined as

$$S^i = N^i + \bar{N}^i \ , \tag{4.1.4a}$$

$$\Delta^i = N^i - \bar{N}^i \ . \tag{4.1.4b}$$

From now on, mentions of the integer phase offsets refer to the four values, $S^1$, $S^2$, $\Delta^1$, $\Delta^2$. $\Delta^1$ and $\Delta^2$ may be determined by finding a point during the FSI scan at which the two laser frequencies are equal (requiring that the sweep frequency ranges are chosen such that this occurs). This point in time may be determined by combining light from both lasers directly and simultaneously onto a single photodiode and recording the optical beat frequency that may be detected when both lasers have similar frequencies. When this beat frequency goes to zero, the two lasers have the same frequency. Labelling the sampling index at this point as $b$, we may thus write $\nu_b = \bar{\nu}_b$. Substituting this, and the definition of $\Delta^i$ given in Eqn. (4.1.4b), into Eqn. (4.1.1) we may calculate an initial estimate of $\Delta^i$ as [1]

$$\hat{\Delta}^i = \bar{u}_b^i - u_b^i \ . \tag{4.1.5}$$

The true value of $\Delta^i$ is an integer (it is defined in Eqn. (4.1.4b) as the difference between two integers). Uncertainties on phase measurement can typically be made much smaller than $\pm 0.5$, and uncertainty on the timing of the point when both lasers have the same frequency

[1] A point to note here is that this result depends upon the definition of the unwrapped phase given in Eqn. (2.2.10), which fixes the phase unwrapping to start from the first data point. This choice is in-built in many equations throughout this thesis. It is perfectly possible to unwrap phase from another point, but if one chooses to do so then care must be taken to make the appropriate adjustments to equations in this thesis.

can also be made much smaller than the time it takes to accrue 0.5 cycles of phase difference between the two lasers. Therefore the above method is capable of determining $\hat{\Delta}^i$ to within $\pm 0.5$ with a high confidence level and we can then reliably determine the exact value of $\Delta^i$ by rounding $\hat{\Delta}^i$ to the nearest integer,

$$\hat{\hat{\Delta}}^i = ||\hat{\Delta}^i|| \; . \tag{4.1.6}$$

In this way, we can reliably and exactly determine two of the four degrees of freedom that the least squares Eqn. (4.1.3) solves for. Rewriting this equation in terms of the sum and difference components defined in Eqn. (4.1.4), Eqn. (4.1.3) becomes

$$\frac{S^1 + \Delta^1 + 2u_n^1}{S^1 - \Delta^1 + 2\bar{u}_n^1} = \frac{S^2 + \Delta^2 + 2u_n^2}{S^2 - \Delta^2 + 2\bar{u}_n^2} \; . \tag{4.1.7}$$

Multiplying by the denominators and subtracting the right hand side then gives

$$S^1(\Delta^2 + u_n^2 - \bar{u}_n^2) - S^2(\Delta^1 + u_n^1 - \bar{u}_n^1) - \Delta^1(u_n^2 + \bar{u}_n^2) + \Delta^2(u_n^1 + \bar{u}_n^1) - 2u_n^1\bar{u}_n^2 + 2\bar{u}_n^1 u_n^2 = 0 \; . \tag{4.1.8}$$

This equation is now solved with least squares, incorporating the known values of $\Delta^1$ and $\Delta^2$ in the solution. The normal method for incorporating an additional measurement of a parameter in a least squares model would be to include an additional equation, representing that measurement. For example, in this case, if the value of $\Delta^1$ is measured to be $\hat{\Delta}^1$, the equation $\Delta^1 = \hat{\Delta}^1$ would be included in the least squares problem. An estimate of the relative uncertainty of this compared to the other measurements would be required when solving the least squares problem.

However, in this case $\Delta^1$ and $\Delta^2$ have been determined with discretised errors. In the absence of a discrete error we know the values of $\Delta^1$ and $\Delta^2$ with a zero error. It is not possible to take account of this in the above formalism as the ratio of errors on the measured phases to the errors on $\Delta^1$ is infinite.

An alternative method for incorporating our knowledge of $\Delta^1$ and $\Delta^2$ into the least

squares solution is simply to fix their values in the model to be equal to their separately measured values, $\hat{\hat{\Delta}}^1$ and $\hat{\hat{\Delta}}^2$, and not to solve for them in the least squares solution. This is only acceptable because of the discrete nature of the errors, and if we assume that no discrete error was made.

It so happens that when this is done, it is possible to write out Eqn. (4.1.8) as a single matrix equation,

$$\begin{pmatrix} \hat{\hat{\Delta}}^2 + u_0^2 - \bar{u}_0^2 & -\hat{\hat{\Delta}}^1 - u_0^1 + \bar{u}_0^1 \\ \hat{\hat{\Delta}}^2 + u_1^2 - \bar{u}_1^2 & -\hat{\hat{\Delta}}^1 - u_1^1 + \bar{u}_1^1 \\ \vdots & \vdots \\ \hat{\hat{\Delta}}^2 + u_{K-1}^2 - \bar{u}_{K-1}^2 & -\hat{\hat{\Delta}}^1 - u_{K-1}^1 + \bar{u}_{K-1}^1 \end{pmatrix} \begin{pmatrix} S^1 \\ S^2 \end{pmatrix} = \begin{pmatrix} \hat{\hat{\Delta}}^1(u_0^2 + \bar{u}_0^2) - \hat{\hat{\Delta}}^2(u_0^1 + \bar{u}_0^1) + 2u_0^1\bar{u}_0^2 - 2\bar{u}_0^1u_0^2 \\ \hat{\hat{\Delta}}^1(u_1^2 + \bar{u}_1^2) - \hat{\hat{\Delta}}^2(u_1^1 + \bar{u}_1^1) + 2u_1^1\bar{u}_1^2 - 2\bar{u}_1^1u_1^2 \\ \vdots \\ \hat{\hat{\Delta}}^1(u_{K-1}^2 + \bar{u}_{K-1}^2) - \hat{\hat{\Delta}}^2(u_{K-1}^1 + \bar{u}_{K-1}^1) + 2u_{K-1}^1\bar{u}_{K-1}^2 - 2\bar{u}_{K-1}^1u_{K-1}^2 \end{pmatrix}, \quad (4.1.9)$$

where $K$ is the number of ADC sampling times during the measurement. This equation is then solved using least squares to calculate estimates for $S^1$ and $S^2$. How this is done is discussed in section 4.1.3. When this has been done, we have values for all four integer phase offsets, and these may be substituted into Eqn. (4.1.2) to calculate the measurement interferometer OPD.

**'Reference estimate' solution option**

It shall be seen later on that the beat detection solution option may become poorly conditioned in certain circumstances. This may be remedied by including an estimate of $S^1$ in the least squares solution. This is obtained using estimated values of the initial laser frequencies, $\nu_0$ and $\bar{\nu}_0$, and the OPD of the reference interferometer, $D_0^1$. With these, we may calculate

$S^1$ by combining Eqns. (4.1.1) and (4.1.4),

$$S^1 = \frac{D_0^1}{c}\left(\nu_0 + \bar{\nu}_0\right) - \left(u_0^1 + \bar{u}_0^1\right) \ . \tag{4.1.10}$$

Even though there may be a considerable amount of uncertainty on the value of our estimate of the laser frequencies (often tuneable lasers do not have a highly reproduceable optical frequency), it will be shown in section 4.2 that it is beneficial to include an estimate of $S^1$ obtained in this manner, and that the accuracy of the final length measurement is not necessarily limited by the uncertainty in the $S^1$ estimate.

As this estimate of $S^1$ has a continuous error distribution, it may be included in the least squares problem as an additional equation, $S^1 = \hat{S}^1$, where $\hat{S}^1$ is the estimate of the value of $S^1$. This may be appended to Eqn. (4.1.9) to give a matrix equation for this solution option,

$$\begin{pmatrix} \hat{\hat{\Delta}}^2 + u_0^2 - \bar{u}_0^2 & -\hat{\hat{\Delta}}^1 - u_0^1 + \bar{u}_0^1 \\ \hat{\hat{\Delta}}^2 + u_1^2 - \bar{u}_1^2 & -\hat{\hat{\Delta}}^1 - u_1^1 + \bar{u}_1^1 \\ \vdots & \vdots \\ \hat{\hat{\Delta}}^2 + u_{K-1}^2 - \bar{u}_{K-1}^2 & -\hat{\hat{\Delta}}^1 - u_{K-1}^1 + \bar{u}_{K-1}^1 \\ 1 & 0 \end{pmatrix} \begin{pmatrix} S^1 \\ S^2 \end{pmatrix} =$$

$$\begin{pmatrix} \hat{\hat{\Delta}}^1(u_0^2 + \bar{u}_0^2) - \hat{\hat{\Delta}}^2(u_0^1 + \bar{u}_0^1) + 2u_0^1\bar{u}_0^2 - 2\bar{u}_0^1u_0^2 \\ \hat{\hat{\Delta}}^1(u_1^2 + \bar{u}_1^2) - \hat{\hat{\Delta}}^2(u_1^1 + \bar{u}_1^1) + 2u_1^1\bar{u}_1^2 - 2\bar{u}_1^1u_1^2 \\ \vdots \\ \hat{\hat{\Delta}}^1(u_{K-1}^2 + \bar{u}_{K-1}^2) - \hat{\hat{\Delta}}^2(u_{K-1}^1 + \bar{u}_{K-1}^1) + 2u_{K-1}^1\bar{u}_{K-1}^2 - 2\bar{u}_{K-1}^1u_{K-1}^2 \\ \hat{S}^1 \end{pmatrix} . \tag{4.1.11}$$

This equation is then solved with least squares to obtain an estimate of $S^2$ and a new estimate of $S^1$.

**'Cascaded' solution option**

The final solution option requires the use of Cascaded FSI. In the next chapter, it will be shown how Cascaded FSI may determine $S^1$ and $\Delta^1$ directly, and with discretised errors. In which case, these values are incorporated into the least squares solution using the same approach as with the beat detection solution option: We assume that no discrete error has occurred, and replace $S^1$ and $\Delta^1$ with the estimates of their true values in the model equation.

When this is done, it so happens that Eqn. (4.1.8) may be written out as a single matrix equation,

$$\begin{pmatrix} -\hat{\hat{\Delta}}^1 - u_0^1 + \bar{u}_0^1 & \hat{\hat{S}}^1 + u_0^1 + \bar{u}_0^1 \\ -\hat{\hat{\Delta}}^1 - u_1^1 + \bar{u}_1^1 & \hat{\hat{S}}^1 + u_1^1 + \bar{u}_1^1 \\ \vdots & \vdots \\ -\hat{\hat{\Delta}}^1 - u_{K-1}^1 + \bar{u}_{K-1}^1 & \hat{\hat{S}}^1 + u_{K-1}^1 + \bar{u}_{K-1}^1 \end{pmatrix} \begin{pmatrix} S^2 \\ \Delta^2 \end{pmatrix} = \begin{pmatrix} \hat{\hat{S}}^1 (-u_0^2 + \bar{u}_0^2) + \hat{\hat{\Delta}}^1 (u_0^2 + \bar{u}_0^2) + 2u_0^1 \bar{u}_0^2 - 2\bar{u}_0^1 u_0^2 \\ \hat{\hat{S}}^1 (-u_1^2 + \bar{u}_1^2) + \hat{\hat{\Delta}}^1 (u_1^2 + \bar{u}_1^2) + 2u_1^1 \bar{u}_1^2 - 2\bar{u}_1^1 u_1^2 \\ \vdots \\ \hat{\hat{S}}^1 \left(-u_{K-1}^2 + \bar{u}_{K-1}^2\right) + \hat{\hat{\Delta}}^1 (u_{K-1}^2 + \bar{u}_{K-1}^2) + 2u_{K-1}^1 \bar{u}_{K-1}^2 - 2\bar{u}_{K-1}^1 u_{K-1}^2 \end{pmatrix}. \quad (4.1.12)$$

This equation is solved using least squares to obtain estimates for $S^2$ and $\Delta^2$.

### 4.1.3 Solving the least squares equations

The three solution options corresponding to Eqns. (4.1.9), (4.1.11) and (4.1.12) are all non-linear least squares problems, as they cannot be expressed in the linear least squares form $AX = b$ where $A$ is a known matrix and all the measured values are contained in the vector, $b$: For all three solution options, the $A$ matrix contains measured values, with errors.

Therefore a non-linear least squares solution is used. The details of this solution are

explained in appendix C.1. This estimator is computed with an iterative procedure that minimises the sum of the squared measurement residuals subject to the constraints provided by the solution option Eqns. (4.1.9), (4.1.11) or (4.1.12).

The non-linear least squares estimator for the remaining unknown integer phase offsets in each solution option is a maximum likelihood estimator under the assumption of unbiased, Gaussian distributed errors on the unwrapped phase values. Tretter [62] has shown, when using the Hilbert transform method for phase calculation in the limit of a high signal to noise ratio, that unbiased, Gaussian distributed errors on the measured intensities lead to unbiased, Gaussian distributed errors on the measured phase values.

## 4.2 Numerical evaluation

This section investigates the impact of random measurement errors on the Dynamic FSI solution for measurement interferometer OPD vs time.

A Dynamic FSI measurement may be considered as consisting of two stages: In the first stage, the integer phase offsets are calculated. The uncertainty in the least squares estimates of integer phase offsets is investigated here, in section 4.2.2. The second stage of the Dynamic FSI measurement is to substitute the calculated values for the integer phase offsets into Eqn. (4.1.2) in order to calculate the measurement interferometer OPD. The impact of errors on the integer phase offsets upon this calculation is investigated here in section 4.2.3.

### 4.2.1 Range of OPDs and frequency sweeps investigated

The propagation of errors calculations in section 4.2.2 are done analytically, but the analytical solution is not particularly revealing, as it is a complicated function of the interferometer OPDs, $D_n^i$, and laser frequencies, $\tilde{\nu}_n$. Therefore, uncertainties are evaluated for particular, defined choices of $D_n^i$ and $\tilde{\nu}_n$ such as those shown in Fig. 4.3.

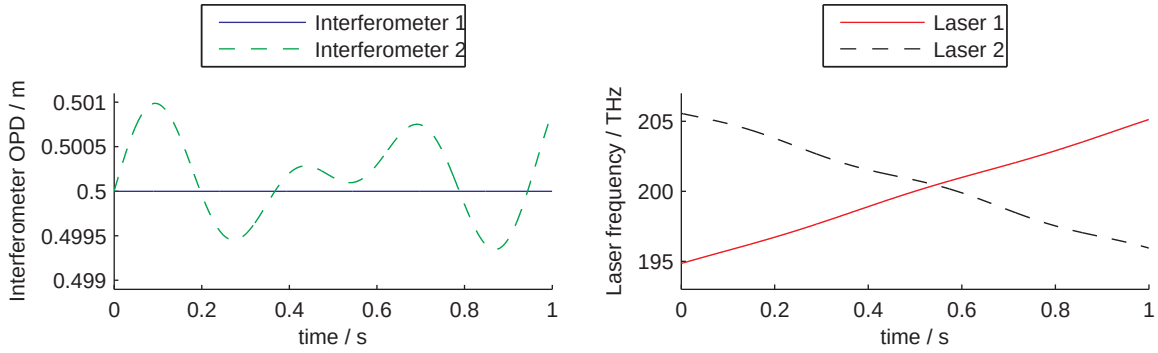


(a) Interferometer OPDs (b) Laser frequencies

Figure 4.3: Simulated interferometer OPDs and laser frequencies

It was found both experimentally and theoretically that when using the beat detection solution option the uncertainty on the integer phase offsets depends upon how much the measurement interferometer moved during the measurement, with larger movements giving (perhaps counter-intuitively) smaller uncertainties. Investigating this phenomenon required simulating various different amounts of measurement interferometer movement. The amount of movement is parameterised as the simulation's *movement scale*, and is an indication of the overall amplitude of movement. All simulations had the same shape of movement as shown in Fig. 4.3(a) and this was linearly scaled according to the value of the movement scale parameter. Figure 4.3(a) has a movement scale of 1 mm.

It was also found that the integer phase offset uncertainty has a dependence upon the lengths of the reference and measurement interferometers. This was investigated by simulating interferometers of different OPDs. In the example of Fig. 4.3(a) both interferometer OPDs are set to 0.5 m.

### 4.2.2 Errors on integer phase offsets

The joint error distribution of estimated values for the integer phase offsets has been calculated for all three solution options. This was done using a standard analytical propagation of errors method explained in appendix C.2. This method calculates the uncertainty on the least squares estimate for the integer phase offsets as a consequence of uncertainty on measured phase values. It parameterises this with a *covariance matrix* describing the probability

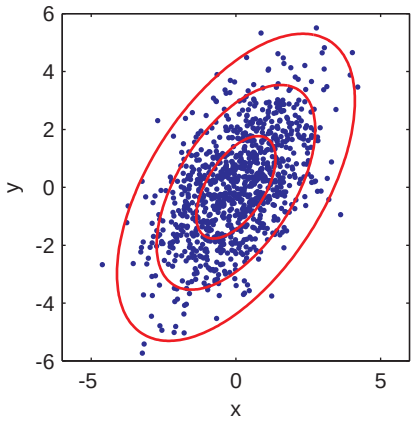


Figure 4.4: Example distribution of correlated Gaussian errors

distribution of errors on the integer phase offsets estimates.

For example, the beat detection solution option calculates least squares estimates for $S^1$ and $S^2$. The joint probability distribution of the errors on $S^1$ and $S^2$ is calculated using the method from C.2, and this calculation parametrises the distribution with a 2×2 covariance matrix.

However, it will be easier to visualise this distribution if it is expressed in a different manner. Figure 4.4 shows an example of a correlated distribution of two random variables. It contains 1000 points with random, correlated, Gaussian distributed x and y coordinates. The ellipses are contours of constant probability density at 1, 2 and 3 standard deviations away from the mean. The distribution of these points may be characterised with a 2×2 covariance matrix. Alternatively, this distribution may be completely characterised by specifying the sizes of the major and minor axes of the ellipse 1 standard deviation away from the mean together with the direction of the major axis (note that the direction of the minor axis is not required as this is necessarily orthogonal to that of the major axis). The size of the major ellipse axis shall be referred to as the *major uncertainty magnitude*, and the size of the minor ellipse axis shall be referred to as the *minor uncertainty magnitude*. The direction of the ellipse's major axis shall be referred to as the *major uncertainty direction*. This parametrisation is a more natural one to use when the errors are highly correlated (i.e. the ellipses have a high eccentricity), as they often turn out to be in the following analyses. It also lends itself to a visual representation of the error distribution, used later on, for example,

in Fig. 4.5(a).

How the ellipse parameters are calculated from the covariance matrix is described in appendix C.2.

**Beat detection solution option**

The distribution of errors on the integer phase offsets as calculated by the beat detection solution option were calculated for measurement and reference interferometer OPDs from 0.1 to 1 metres, in 0.1 metre increments, giving a 10×10 grid of results. These are displayed graphically in Fig. 4.5.

The uncertainties on the integer phase offsets are calculated as a consequence of unbiased, Gaussian distributed errors on the measured phases with a standard deviation of 1 fringe. The integer phase offset uncertainties scale linearly with the uncertainty on measured phases, so, for example, they would be 10 times smaller if the uncertainty on the measured phases was 0.1 fringes. The movement scale used for these simulations was 10 $\mu$ m. The simulated measurements each consisted of $2 \times 10^5$ samples.

Figure 4.5(a) shows the major uncertainty direction for every combination of initial interferometer length. The centre position of each line corresponds to the simulated initial interferometer lengths as indicated on the main plot axes. The direction of each line corresponds to the major uncertainty direction, as indicated by the small axes in the upper right hand corner.

The major uncertainty magnitude is shown in Fig. 4.5(b), and the minor uncertainty magnitude is shown in Fig. 4.5(c).

The most important point to note about these is not the distribution of each one within the 10×10 grid of results, but the relative scales of the major uncertainty magnitude and minor uncertainty magnitude: The major uncertainty magnitude is roughly $5 \times 10^4$ fringes for most interferometer OPDs, whereas the minor uncertainty magnitude is a comparatively tiny $\simeq$0.2 fringes. This means that the error ellipses are highly eccentric and therefore that

the orientation of the ellipses has a big impact.

In Fig. 4.5(a) it may be seen that the major uncertainty direction is always aligned toward the origin of the plot. This indicates that the major uncertainty is in the overall scale of $(S^1, S^2)$. The minor uncertainty, being perpendicular to this, is on the ratio of $S^2/S^1$. The effect of this error distribution on the final measurement interferometer OPD calculation is investigated in section 4.2.3.

**Reference estimate solution option**

Figure 4.6 displays the results for the beat detection plus reference estimate solution option in the same manner as Fig. 4.5.

From Fig. 4.6(a) it may be seen that the major uncertainty directions are the same as those of the beat detection solution option. However, Fig. 4.6(b) shows that the major uncertainty magnitude is greatly reduced for this method.

Figure 4.6(c) shows no significant difference in the minor uncertainty magnitude when compared with the beat detection solution option.

**Cascaded solution option**

Figure 4.7 displays the results for the cascaded solution option in the same manner as for the previous two solution options. Recall, however, that this method calculates a different subset of the integer phase offsets to the other two solution options, as indicated by the small axes in the upper right of Fig. 4.7(a).

From Fig. 4.7(a) we see that the major uncertainty direction always points in the direction of $S^2$, regardless of interferometer OPD ratio. This indicates that for this solution option, the errors on $S^2$ and $\Delta^2$ are uncorrelated. Hence Fig. 4.7(b) corresponds directly to the uncertainty on $S^2$, and Fig. 4.7(c) corresponds directly to the uncertainty on $\Delta^2$. Both uncertainties are small when compared to those from the other solution options, although they do increase when the measurement interferometer is significantly larger than the ref-

erence interferometer. This fact is a very important point in Cascaded FSI, and it shall be discussed further in section 5.

### Effect of movement scale

The effect of the scale of movement of the measurement interferometer during a Dynamic FSI measurement was investigated. Recall that in this analysis the measurement interferometer was modelled as moving during the measurement with a shape of movement as shown in Fig. 4.3(a), and an overall amplitude of movement given by the movement scale parameter.

Fig. 4.8 shows the variation of uncertainty on the integer phase offsets as a function of measurement interferometer movement scale for all three solution options. The uncertainties are parametrised, as before, in terms of the major uncertainty magnitude and the minor uncertainty magnitude.

The solution option with the most dependence on movement scale is the beat detection solution option, Fig. 4.8(a). Whilst the minor uncertainty magnitude is mostly unchanged with variation of movement scale, the major uncertainty magnitude grows exponentially when the movement scale is reduced. This result indicates that there is a symmetry in the Dynamic FSI equations for this method such that when there is no movement of measurement or reference interferometer (or rather, when there is no relative change in length) varying $(S^1, S^2)$ along the major uncertainty direction will not change the measured phase values at all.

This is highly undesirable: Although the major benefit of Dynamic FSI is its ability to measure a changing OPD, this result shows that when using the beat detection solution option, a changing OPD is actually a requirement! The reference estimate solution option was created as a solution to this problem. In Fig. 4.8(b), we see that, in contrast to Fig. 4.8(a), the major uncertainty magnitude does not continue to increase when the movement scale is reduced. This is due to the estimate of the value of $S^1$ that is included in the reference estimate solution option.

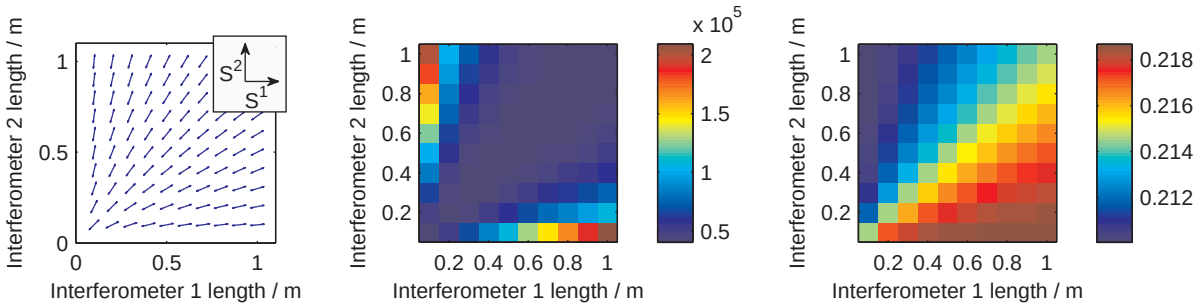


(a) Major error directions (b) Major error magnitude (c) Minor error magnitude

Figure 4.5: Uncertainties for the beat detection solution option

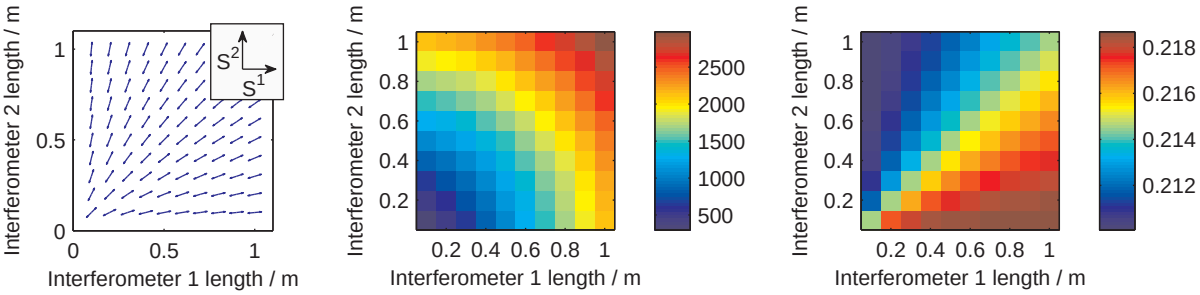


(a) Major error directions (b) Major error magnitude (c) Minor error magnitude

Figure 4.6: Uncertainties for the reference estimate solution option

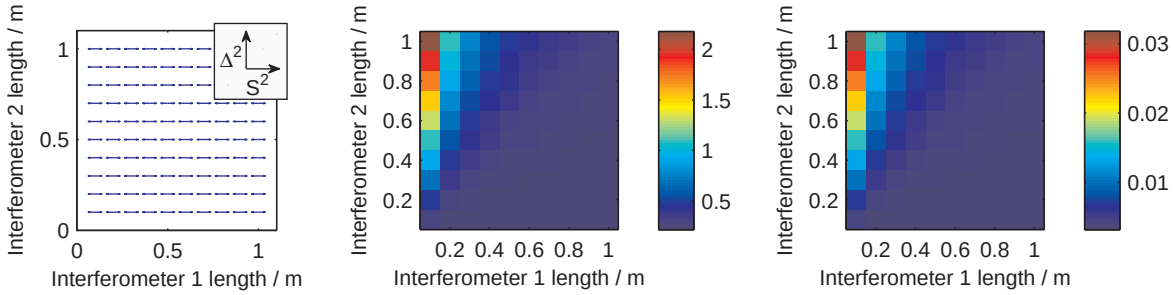


(a) Major error directions (b) Major error magnitude (c) Minor error magnitude

Figure 4.7: Uncertainties for the cascaded solution option

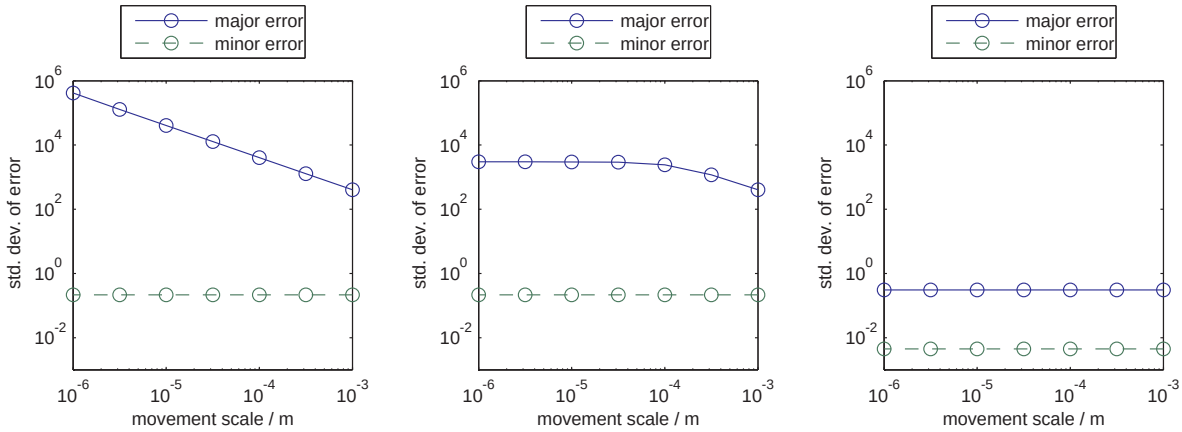


(a) Beat detection (b) Reference estimate (c) Cascaded

Figure 4.8: The effect of measurement interferometer movement on uncertainty of integer phase offset calculation

We also see that when the measurement interferometer movement scale is large enough such that the least squares solution can determine $S^1$ with less uncertainty than our estimate, $\hat{S}^1$, then this solution is able to make use of that information. This is seen on the right hand side of the plot, where for movement scales greater than $10^{-4}$ m, the major uncertainty magnitude reduces.

Finally, for the cascaded solution option, Fig. 4.8(c), we see the desirable feature that the uncertainty is unaffected by movement scale within the range of tested parameters.

### 4.2.3 Integer phase offset errors' impact on distance ratio calculations

Here I consider the effect errors on the integer phase offsets will have on the distance ratios as calculated by Eqn. 4.1.2.

This is done by adding 0, 1, 2 and 3 standard deviations of major and minor error to the true values of the integer phase offsets, and plotting the resulting error vs time in calculated measurement interferometer OPD. All plots were calculated for integer phase offset uncertainties corresponding to a movement scale of $10^{-6}$ m, and interferometer OPDs of 1 m for both reference and measurement interferometers. The variation of measurement

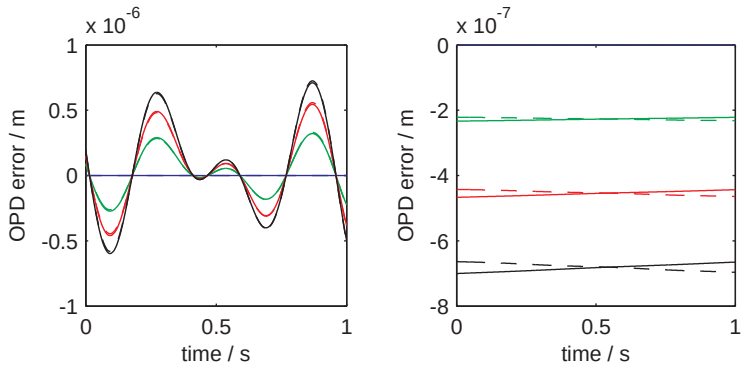


(a) Major error (b) Minor error

Figure 4.9: Measurement interferometer errors versus time for beat detection solution option

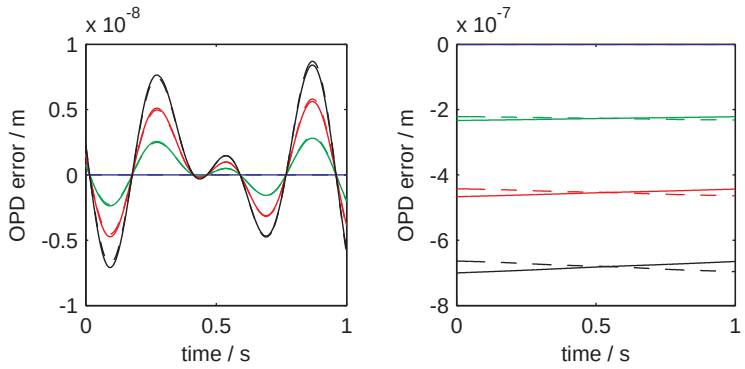


(a) Major error (b) Minor error

Figure 4.10: Measurement interferometer errors versus time for reference estimate solution option

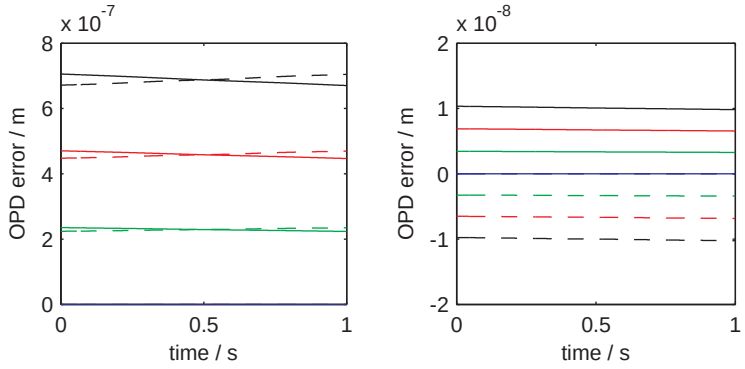


(a) Major error (b) Minor error

Figure 4.11: Measurement interferometer errors versus time for cascaded solution option

interferometer OPD with time, as for previous sections, takes the shape shown in Fig. 4.3(a).

Figure 4.9 shows the error vs time in measurement interferometer OPD when the beat detection solution option is used. Figure 4.9(a) shows the consequence of 0, 1, 2, and 3 standard deviations of the major error. These are plotted in blue, green, red, and black, respectively. The solid lines show the OPD calculated with data from the first laser, using Eqn. (4.1.2a) whereas the dashed lines show the OPD as calculated with data from the second laser, using Eqn. (4.1.2b).

As would be expected, the curves corresponding to larger errors on the integer phase offsets have larger errors in calculated distance. The error follows the shape of the measurement interferometer's actual movement, shown in Fig. 4.3(a), and is therefore an error in the calculated scale of this movement.

Figure 4.9(b) shows the consequence of 0, 1, 2, and 3 standard deviations of the minor error in the beat detection solution option. The colours and solid/dashed lines in this correspond to the same quantities as in Fig. 4.9(a). In this plot, the errors do not follow the shape of the movement, which shows that the effect of the minor errors is to produce a constant error in the calculated measurement interferometer OPD.

Figures 4.10(a) and 4.10(b) indicate that broadly similar behaviour is found in beat detection, and reference estimate options. The single significant difference is that the scale of the errors in Fig. 4.10(a) has been greatly reduced due to the influence of adding the estimate of the value of $S^1$.

The effect of errors in integer phase offsets calculated using the cascaded solution option are shown in Figs. 4.11(a) and 4.11(b). Neither of these take the shape of the actual movement, but are instead offsets that are constant for each measurement.

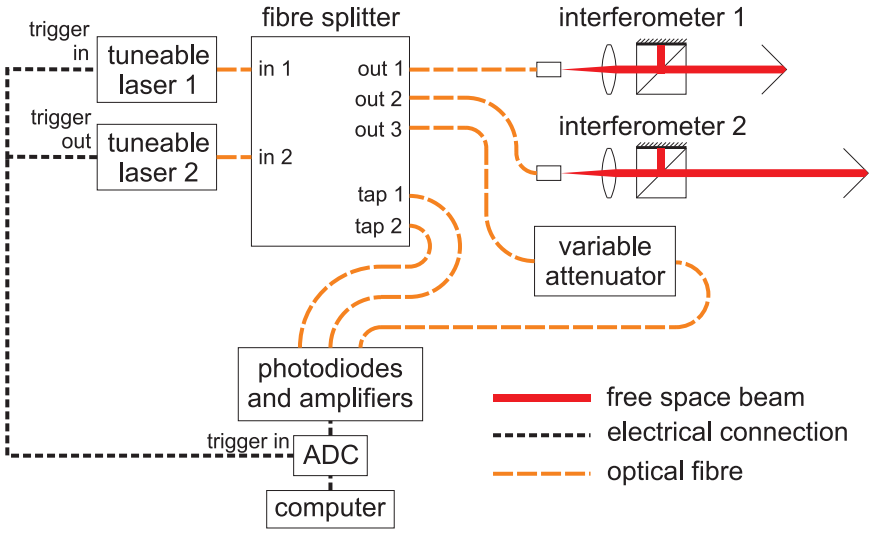


Figure 4.12: Equipment layout

## 4.3 Experimental evaluation

This section contains an experimental demonstration and evaluation of Dynamic FSI. Section 4.3.1 describes the arrangement of equipment used for experimental tests. Section 4.3.2 contains a step by step example of a Dynamic FSI measurement analysis. The ability of Dynamic FSI to measure a changing distance is investigated in section 4.3.3, and section 4.3.4 contains a comparison of the precision of Dynamic FSI and single laser FSI.

### 4.3.1 Equipment and Method

Equipment used for the following tests of Dynamic FSI was arranged as shown in Fig. 4.12.

The components may be classified in three groups; lasers, interferometers, and data acquisition components. Light is directed, combined, and shared between these using optical fibres and fibre splitters. All fibres are terminated with FC-APC connectors. These connectors have an extremely low back-reflection, which is vital when working with interferometers, as these are inherently sensitive to additional optical paths created by unwanted reflections at interfaces such as fibre ends or fibre-fibre connections.

Two lasers are required for these measurements. Laser 1 is an Agilent 81640A tuneable laser module housed in an Agilent 8164A mainframe. Laser 2 is a Santec TSL-510-A tuneable

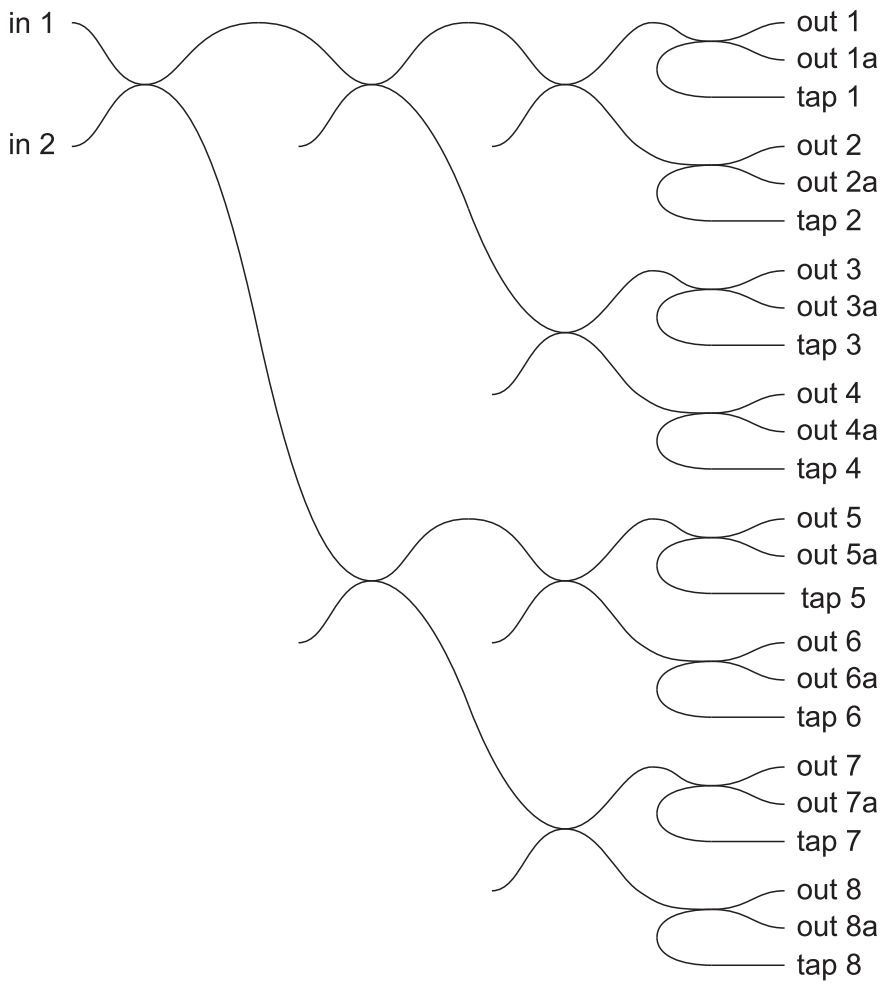


Figure 4.13: Internal structure of fibre splitter tree, which is composed of 15 individual 2×2, 50:50 splitters connected together to split light from each of the 2 inputs into 16 outputs. Half of the light entering into each numbered pair of outputs goes into the tap outputs.

laser. Both lasers have fibre coupled outputs and inbuilt optical isolators.

The optical outputs of both lasers are connected to a fibre splitter tree, which combines their light and distributes it to several outputs. The internal structure of the splitter tree is shown in Fig. 4.13. The outputs are grouped into pairs, each being associated with a *tap*, from which light returning into the splitter tree outputs may be detected. Only one output of each pair is used (e.g. out 1 is used, but out 1a is not), such that photodiodes attached to the tap outputs each receive light from one interferometer only.

Interferometer 1 is used as a reference interferometer, and interferometer 2 is the measurement interferometer. Each interferometer consists of a collimator together with a beam-splitter cube which has one face gold coated. The cube is aligned such that the reflected light from the gold coated face forms the short arm of a Michelson interferometer, and is collimated back into the fibre. The light transmitted through the beam-splitter cube forms the second arm of the interferometer. This is reflected back to the cube and collimator by an open corner cube retro-reflector. The output of the interferometer is therefore the light that returns back into the fibre, which is detected with the splitter tree tap outputs.

Output 3 of the splitter tree is sent, through a variable fibre attenuator, directly onto a fibre coupled photodiode. This is used to detect the beat signal that may be detected when the two lasers' frequencies cross. The attenuator is used to reduce the optical power to a suitable range for detection with the photodiode.

The photodiode and amplifier electronics are on a board developed in-house, with the amplified signals sent via BNC cables to the ADC, which is a National Instruments PCI-6115, 4 channel, 12 bit ADC. When more than 4 channels are needed, a second PCI-6115 ADC is used, with acquisition synchronised with the first ADC using a common clock signal.

To make a Dynamic FSI measurement, the frequency of both lasers is swept in a linear fashion whilst simultaneously recording the voltages from the amplified photodiodes with the ADC. This requires starting the laser scans and ADC acquisition simultaneously. Laser 2 is used to control the measurement start times. It is set to perform either a single or

| Parameter | Value |
|---|---|
| ADC sampling rate | 2 MS/s |
| ADC anti-aliasing filter frequency* | 500 kHz |
| ADC discretisation level | 0.977 mV |
| Laser 1 wavelength scan settings | 1555 nm → 1575 nm at +20 nm/s |
| Laser 2 wavelength scan settings | 1610 nm → 1510 nm at -100 nm/s |
| Laser power | 0.1 mW (both tuning lasers) |

Table 4.1: Summary of equipment settings for Dynamic FSI test measurements. * The anti-aliasing filter was turned off for the channel used to detect the beat signal.

repeated sweeps, and outputs a trigger signal at the start of a sweep. This is connected via BNC cables to trigger inputs on laser 1 and the ADC, which start scanning and recording respectively upon receiving a trigger signal.

### 4.3.2 Analysis

This subsection goes step by step through a Dynamic FSI analysis of data taken with the above setup. The Hilbert transform method will be used to calculate interferometric phases, and the reference estimate solution option will be used to determine the remaining unknown integer phase offsets.

For this measurement, the lasers were set to vary their wavelengths as described in table 4.1. The wavelength ranges were chosen such that the two tuning lasers will have the same optical frequency at one point during the measurement period, and a transient beat signal can be measured to determine when this happens. The wavelength variation rates were chosen such that the FSI signal frequencies produced by each laser are different from each other.

Configuration settings for the ADC are also summarised in table 4.1. The sampling rate is chosen to be high enough to record the transient beat signal occurring when both lasers have the same optical frequency.

**Phase calculation and signal separation**

The first stage of the analysis is to separate the interference signals generated by each of the two lasers. This may be done by varying each laser's optical frequency at a different rate. According to Eqn. (2.1.6) this will mean that the frequencies of the voltage signals generated from the two lasers will be different. Software band-pass filters are used to isolate the signal from each laser after all data has been acquired.

In section 2.2.2, I showed how a Hilbert transform may be used to calculate the phase from an FSI interference signal.

Both the signal separation step and the phase calculation step are done by computing the discrete Fourier transform (DFT) of the original signal, multiplying the result with a window function, and finally computing the inverse DFT of that result. To save computation time, I perform both these operations using only one pair of forward and inverse DFTs. This is done by computing the DFT of the original signal, and then multiplying the result by both the band pass filter window and the Hilbert transform window, and then computing the inverse DFT of the result.

I now present a step by step example of this combined signal separation and phase calculation analysis. The starting point for this is the ADC's record of the voltages from the amplified photodiodes during a laser frequency sweep. An example for one photodiode from a 2 millisecond period in the middle of a measurement is shown in figure 4.16. Two frequency components can clearly be distinguished in this figure. These are the interference fringes from each laser, varying at different rates proportional to the different frequency variation rates of each laser. As laser 1 is tuning at a slower rate of +20 nm/s (-2.5 THz/s) compared to laser 2's tuning rate of -100 nm/s (+12.5 THz/s) we know that the slower frequency component is interference fringes created by laser 1, and the higher frequency component is interference fringes created by laser 2. As a sanity check, one may note that the ratio of fringes (approx. 2 slow fringes compared to approx. 13 fast fringes) is roughly equal to the ratio of laser tuning rates, as would be expected.

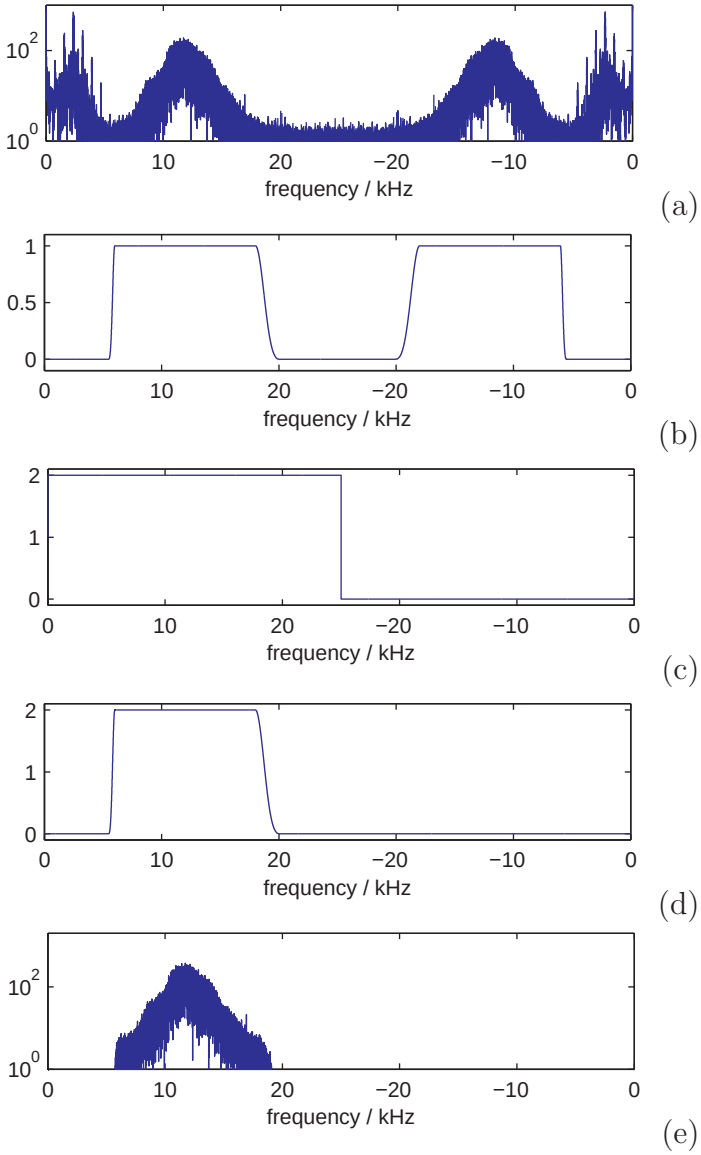


Figure 4.14: Illustration of Hilbert transforming and band pass filtering interferometer data

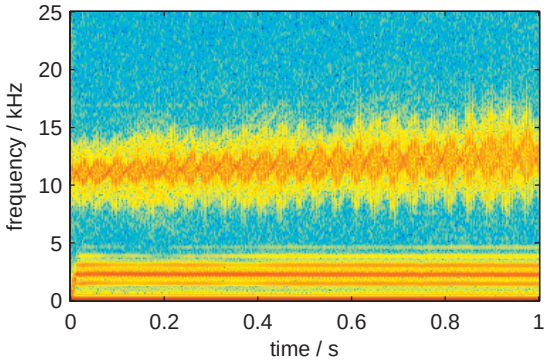


Figure 4.15: Spectrogram of interference signal

The first step in the analysis is to compute the DFT of this raw photodiode voltage signal (NB not just the 2 ms section plotted; the DFT of the entire 1 s measurement is computed). The complex amplitude of the result is plotted in Fig. 4.14(a). In order to aid illustration the time domain data used to generate these plots has been down-sampled by a factor 40. This is equivalent to dealing with the same data, but sampled at 50 kS/s instead of 2 MS/s. The actual analysis used the non down-sampled data. The entire result of the DFT is shown, including the negative frequencies that may be seen in the right half of the plot as a mirror image of the positive frequencies on the left. Note that zero frequency is to the left of this plot, with the Nyquist frequency in the centre of the horizontal axis.

Two frequency components may be identified in this figure as the two broad peaks. Each peak is the interference signal from one of the two tuning lasers. The width of these peaks is due to non-linearities in the tuning behaviour of the lasers: They are unable maintain a perfectly constant rate of change of optical frequency, and therefore the interference signal generated by the laser frequency variation is not a perfect sinusoid and the Fourier transform peaks are broadened as a result. A spectrogram of the signal, plotted in figure 4.15, provides further evidence of this.

The width of the peaks in Fig. 4.14(a) is the reason why such significantly different laser tuning rates (100 nm/s and 20 nm/s) were chosen. These very different tuning rates allowed both laser signals to be separated even though the signal from each laser is spectrally broad due to the non-linear tuning behaviour. If the lasers tuned more linearly, it would have been possible to choose more similar tuning rates.

The band-pass filter window used to isolate the signal from the faster tuning laser is plotted in Fig. 4.14(b). Note that this band-pass filter window is completely flat over the entire region of the signal peak. If this were not the case then the window would alter the signal, and therefore also alter the phase calculation results. The purpose of filtering is to isolate the signal from each laser, and should leave the selected signal unaltered. This is also the reason for the slight assymetry in this window: The lower frequency end of the window has a sharp cut-off to avoid allowing some of the signal from the slower tuning laser into the window, whereas at the higher frequency end of the window there is no other signal nearby, so it is possible to have a smoother edge to the window (in general, smooth edges to band-pass filter windows are preferred as this reduces artefacts such as ringing and edge effects).

The window function of Eqn. 2.2.7, which is used to perform the Hilbert transform and generate the analytic signal, is plotted in Fig. 4.14(c). Applying both these windows one after the other is the same as applying the product of these windows, which is shown in Fig. 4.14(d). The result of applying this window to the data is shown in Fig. 4.14(e).

The window functions for the band-pass filter were chosen such that they were flat over the width of the signal peaks. This is required in order for the Hilbert transform to work: If the signal were to be altered by a spectral window with a variable amplitude or phase response over the region of the signal, then the Hilbert transform would not perform as shown in section 2.2.2. Following the general practice of not using sharp edged filters, the windows smoothly go to zero. However, it should be noted that, for this data at least, the amplitude of the Fourier transform outside the signal peaks is much smaller than the amplitude of the peaks themselves (this data had a high signal to noise ratio): This means that the shape of the window in the regions outside the signal peaks cannot have a large effect on the resulting filtered signal. If one wished to use this method with data that has a lower signal to noise ratio, however, it may be worthwhile to investigate the impact of the way in which the window function goes to zero.

The windowed DFT'd data as shown in Fig. 4.14(e) is then inverse DFT'd, with the

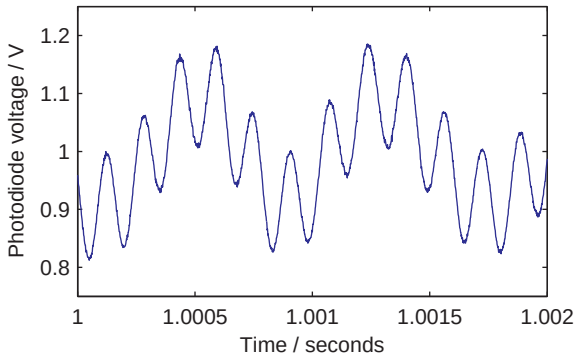


Figure 4.16: Observed intensity output of interferometer 1

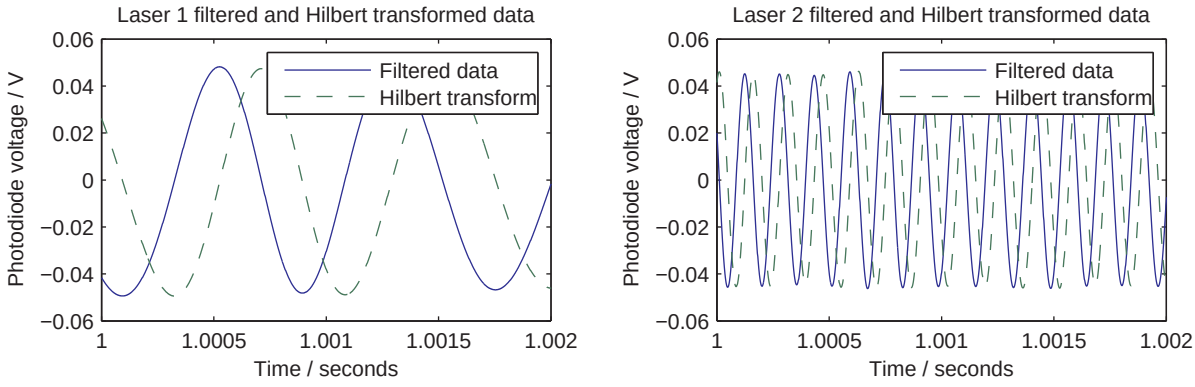


(a) (b)

Figure 4.17: Intensity data filtered and Hilbert transformed to select ,4.17(a), laser 1's signal and, 4.17(b), laser 2's signal.

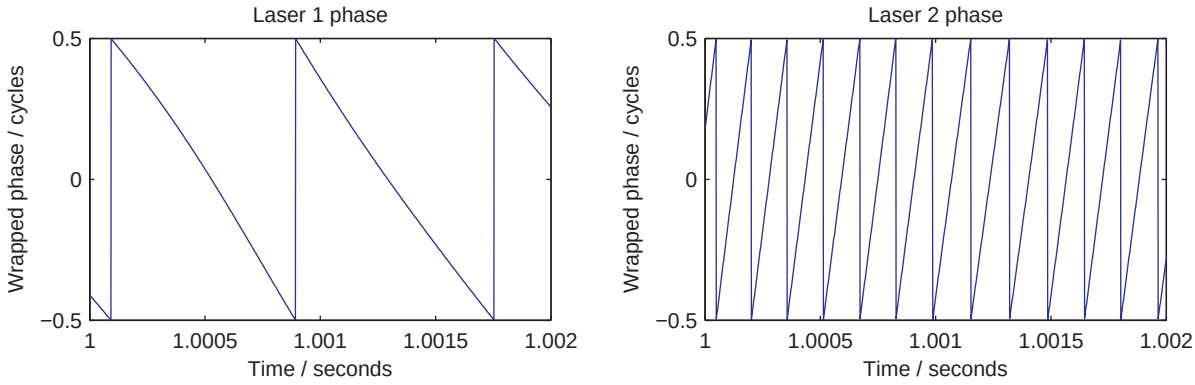


Figure 4.18: Calculated wrapped phase from, 4.18(a), laser 1 and, 4.18(b), laser 2

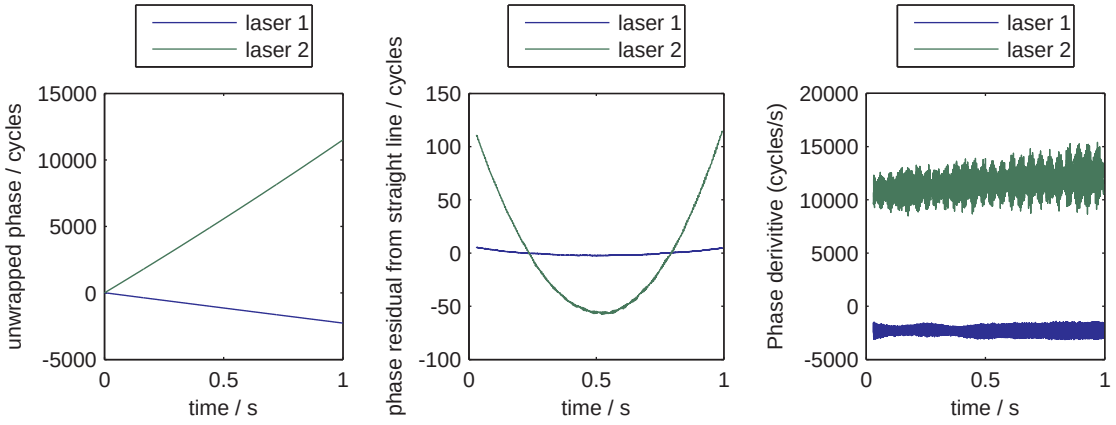


Figure 4.19: (a) Unwrapped phase from both lasers in interferometer 1, (b) Residual from a linear fit to the phase, (c) Derivative of the phase.

result shown in Fig. 4.17(b). The same band-pass filter and Hilbert transform procedure is applied for the slower tuning laser, and the result is shown in Fig. 4.17(a). For comparison, with Fig. 4.16, both these plots are shown over the same 2 millisecond time period.

The signals from each laser have now been separated. The Hilbert transform of each signal has been calculated, and included as the imaginary part of the original (real) signal, thus forming the analytic signal. The wrapped phase, shown in figure 4.18, is calculated by taking the four quadrant arc tangent of the real and imaginary components of this.

Recall from section 2.2.2 that the Hilbert transform cannot distinguish between an increasing and a decreasing interferometric phase, and always calculates an increasing phase. In this measurement we know that the phase corresponding to laser 1 is decreasing, as the laser frequency decreases during the measurement. To take this into account, the phase corresponding to laser 1 is multiplied by $-1$. No such step is required for the phase corresponding to laser 2, as this has been set to increase its optical frequency during the sweep.

Figure 4.19(a) shows the unwrapped phase from each of the lasers. This figure shows that over the entire measurement, the laser tuning is quite linear. However, upon plotting the deviation from a linear fit to each of these curves (figure 4.19(b)) the variation from linear tuning becomes apparent.

It is vital for this measurement method that the phase unwrapping process is performed

correctly. A simple check of this may be performed by plotting the derivative of the unwrapped phase (Fig. 4.19(c)). The limited range of the derivative means that the unwrapped phase is a smooth curve, with no observable jumps or discontinuities. The lack of these is not a guarantee that phase unwrapping was successful, but is a useful check nonetheless.

### Beat signal detection and Delta estimation

Recall that for the reference estimate solution option, for each interferometer, the difference in the integer phase offsets corresponding to each laser must be determined. These differences are defined as $\Delta^1$ and $\Delta^2$ for the reference and measurement interferometers, respectively. They are calculated by observing a transient beat signal that may be detected when the two lasers' frequencies cross.

One of the outputs of the fibre splitter is sent straight onto an amplified photodiode. The ranges of the laser frequency scans are chosen such that the frequencies of the two lasers cross during the measurement, and a transient beat signal may be detected for a short period of time around this crossing point. An example of such a signal is plotted in fig. 4.20. This signal was generated with the lasers scanning at +20 nm/s and -100 nm/s respectively, and was digitised with an Agilent Technologies DSO3102A Digital Storage Oscilloscope acquiring at a rate of 100 MS/s. As expected, the frequency of the beat signal increases away from the centre of the figure (which is at t = 3.5 $\mu$s) as the difference between the two lasers' optical frequencies increases. This central point, where the beat frequency goes to zero, is the point in time when the two lasers had the same frequency. The amplitude of the detected beat signal drops off as its frequency increases, due to the limited bandwidth of the photodiode amplifier.

The signal in figure 4.20 was digitised at a higher sampling rate than can practically be used for our FSI measurements. This is because we wish to sample for 1 second for these measurements, and the memory available on the ADC allows a maximum sampling rate of 2 MS/s over this time period. After testing, this sampling rate turned out to be sufficient, even though the duration of the detectable beat signal lies within only a few ADC acquisitions.

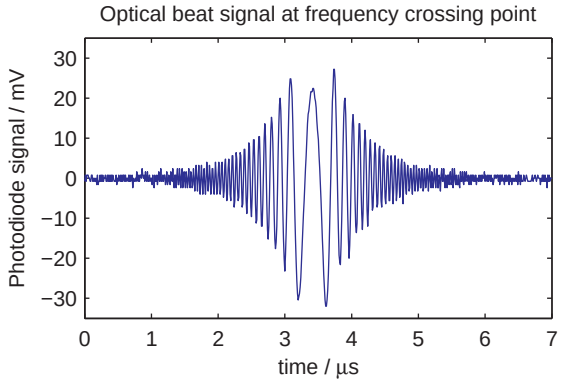


Figure 4.20: Transient beat signal between two scanning lasers

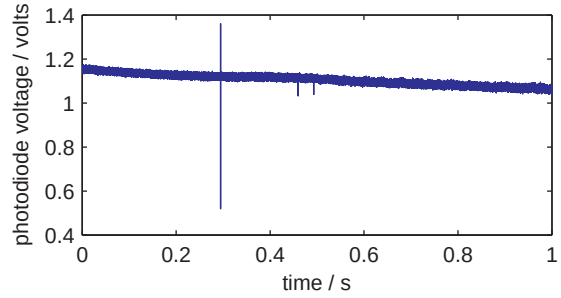


Figure 4.21: Beat signal from FSI scan

The reason that this is acceptable is the discretisation step embodied by Eqn. 4.1.6. This means that we only need to detect when the laser frequencies were the same to within ±0.5 of an interference fringe.

The signal on the beat detection photodiode recorded during the example Dynamic FSI measurement is plotted in figure 4.21. With the lower sampling rate, we cannot resolve the structure observable in Fig. 4.20. However the sharp spike in the signal near t=0.3s is sufficient to identify the time that the beat signal occurred at. To detect this signal, the data is high pass filtered and squared. The signal is then located by finding the maximum value in a range around the expected location according to the the nominal tuning behaviour of the lasers. The *beat index*, $b$, is set to be the ADC sample index for this point.

A first estimate of the difference in integer phase offsets, $\hat{\Delta}^i$ is calculated for each interferometer by taking the difference of the unwrapped phase values at the beat index, according to Eqn. 4.1.5. A second estimate, $\hat{\hat{\Delta}}^i$, with discretised error, is then calculated by rounding the value of the first estimate to the nearest whole fringe, according to Eqn. (4.1.6).

**S estimate**

For this example measurement we use an estimate of $S^1$ obtained from an estimate of the laser frequency and interferometer OPD, according to Eqn. (4.1.10).

**Least squares**

Equipped with the values of $\Delta^1$ and $\Delta^2$ and an estimate of $S^1$, the reference estimate solution option, Eqn. (4.1.11), is solved with least squares to calculate an estimate for $S^2$ and a new estimate for $S^1$.

**Distance ratios**

Now that we have values for all four integer phase offsets, $S^1$, $S^2$, $\Delta^1$, and $\Delta^2$, we may proceed to calculate the OPD of the measurement interferometer at each and every sampling point by evaluating Eqns. (4.1.2). The results of this are plotted in Fig. 4.22, where the mean measurement interferometer OPD of 0.512 m (according to laser 1 data) has been subtracted from the data. This measurement was made whilst holding the measurement interferometer OPD as constant as possible.

Perhaps the most obvious feature on this plot is the systematic discrepancy between the measurement interferometer OPD according to the two lasers. Recall that the least squares solution does in some sense attempt to minimise this discrepancy, but only has a small number of degrees of freedom to vary. The cause of this discrepancy is unknown, but a likely cause would be some wavelength dependent effect such as dispersion in the measurement medium. Laser 2 scanned over a larger wavelength range of 100 nm when compared to the 20 nm range of laser 1. Any wavelength dependent terms not taken into account in our model would therefore be more pronounced in the data from this laser.

The difference in the apparent noise level between the two lasers' data is also unknown, but a possible reason is that the intensity data from laser 1 was in a lower range of frequencies than the laser 2 data. It will therefore be subject to a higher level of 1/f noise. Also, as

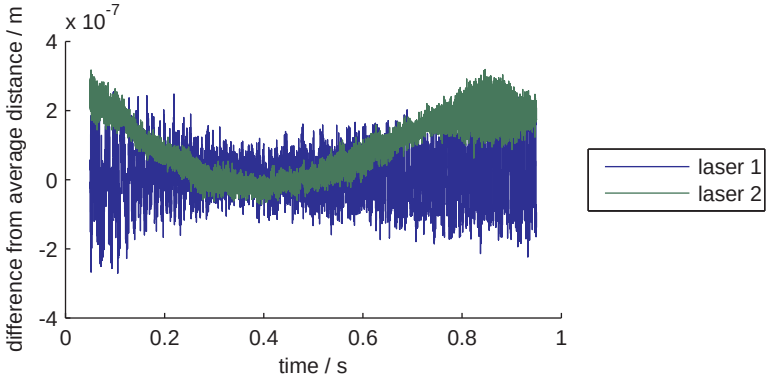


Figure 4.22: Dynamic FSI final result

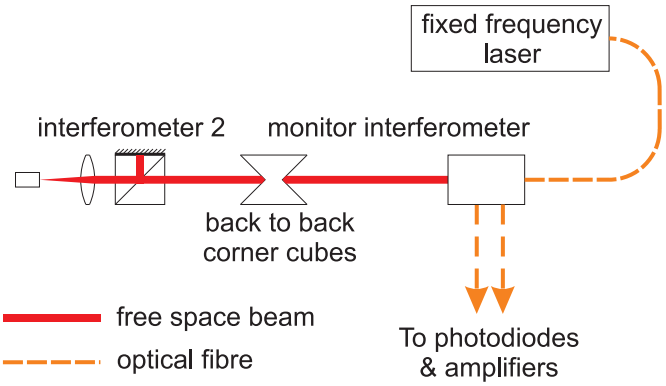


Figure 4.23: Layout of additional equipment for verification of Dynamic FSI with fixed frequency interferometry

can be seen from Fig. 4.14 (a), it is not clear that the peak corresponding to laser 1's signal is entirely separate from the lower frequency components of the signal, as is required for the Hilbert transform to work correctly. If there is a slight overlap, this would create small errors in the phase calculated by the Hilbert transform.

### 4.3.3 Measurement of changing distances

The ability of Dynamic FSI to measure a changing distance was investigated by measuring a moving target with Dynamic FSI and a conventional fixed frequency interferometer simultaneously.

### Experimental setup

The equipment setup for this test was based upon Fig. 4.12, with the addition of a *monitor interferometer* arranged as shown in Fig. 4.23. This was aligned co-linearly with the measurement interferometer (interferometer 2) by adjusting the collimators in each such that light emitted by one was received by the other when no other optics were present. A motion stage with two corner cube retro-reflectors arranged back to back was placed in between the two interferometer heads. When this motion stage is moved along an axis parallel to the beams, the change in OPD created in one interferometer is equal and opposite to the change in OPD created in the other interferometer.

The monitor interferometer is fed with light from an Orbits Lightwave Ethernal fixed frequency laser. The interferometer has two phase shifted readouts, the light from which is collected with optical fibres and sent onto fibre coupled photodiodes. These photodiodes are digitised simultaneously with data from the FSI interferometers.

A disadvantage of this setup is that the beams in interferometer 2 and the monitor interferometer have different optical paths. Therefore changes in the refractive index of air will cause an apparent discrepancy between the distance measurements using the two interferometers. To minimise this disturbance, all heat sources such as power supplies and electronics were kept away from the two interferometers and where possible the path of the beams was covered.

### Method

The motion stage was moved whilst measuring the OPD of the measurement interferometer with Dynamic FSI, and simultaneously measuring the displacement of the monitor interferometer with single wavelength interferometry.

The Dynamic FSI measurements were made as described in section 4.3.2. The single wavelength interferometry measurements were made as described in section 3.1, with the

phase shifted readouts processed with *Heydemann correction*[2] [40].

The measured displacements from single wavelength interferometry and Dynamic FSI are made with respect to different length scales: Dynamic FSI measures distances relative to the reference interferometer OPD, whereas single wavelength interferometry measures distances relative to the wavelength of the Ethernal laser. To compare measurements, the ratio of these length scales must be calibrated. This was done using one of the simultaneous Dynamic FSI and single wavelength interferometry measurements. Without calibration, both methods measure the same displacement with respect to their own length scales. Therefore the measured displacements from both methods are linearly related, with the relative magnitudes of the two measurements equal to the ratio of the length scales from each measurement. A linear fit to this data was used to calibrate the relative length scales.

The estimate of $S^1$ was calculated by solving least squares Eqn. (4.1.9) for a measurement that had a large movement of the measurement interferometer.

**Results**

Figures 4.24, 4.25 and 4.26 show comparisons of the stage displacement as measured with the monitor interferometer, and Dynamic FSI. Each plot shows (a) the displacement measured by the monitor interferometer, and by Dynamic FSI; and (b) the difference between these. In order to compare measurements from both systems, the measured values are shifted such that the displacement is zero at the first data point in each plot. Data from Fig. 4.24 was used to compute the estimate of $S^1$. This estimate was used in the analysis for the other two figures.

These plots show a very good agreement between both measurement types. With movements hundreds of microns in size, the deviation between the two measurements rarely goes above 0.1 $\mu$m.

It is believed that a major cause of the discrepancy between these measurements may

[2] A method for calculating phase in a quadrature readout system that does not have a phase shift of exactly 90°

| Parameter | Covered | Uncovered |
|---|---|---|
| ADC sampling rate | 2 MS/s | 2 MS/s |
| ADC anti-aliasing filter frequency* | 500 kHz | off |
| ADC discretisation level | 0.977 mV | 0.977 mV |
| Laser 1 wavelength scan range | 1555 nm → 1575 nm | 1555 nm → 1575 nm |
| Laser 1 wavelength scan speed | +20 nm/s | +20 nm/s |
| Laser 2 wavelength scan range | 1610 nm → 1510 nm | 1630 nm → 1530 nm |
| Laser 2 wavelength scan speed | -100 nm/s | -100 nm/s |
| Laser 1 power | 0.1 mW | 0.1 mW |
| Laser 2 power | 0.1 mW | 0.1 mW |
| Interferometer 1 approx length | 0.24 m | 1.72 m |
| Interferometer 2 approx length | 0.24 m | 0.61 m |

Table 4.2: Summary of equipment settings for Dynamic FSI test measurements. * The anti-aliasing filter was turned off for the channel used to detect the beat signal.

have been vibration in the head of the measurement interferometer (which was of less solid construction than the monitor interferometer head), excited by the forces imparted to the optical table whilst the stage was being moved. This is supported by, in Fig. 4.26 the location of spikes in the discrepancy occurring simultaneously with turning points in the stage position, when the largest forces will have been imparted to the table.

### 4.3.4 Comparison of precision with single laser FSI

The precision of measurements made with Dynamic FSI was compared with that of single laser FSI. This was done by making repeated Dynamic FSI measurements of a nominally fixed length using the setup and method as described in section 4.3.2. The same data was then analysed, using the unwrapped phases of each laser individually, with the single laser FSI technique as described in section 3.3.

This test was performed in two different situations. In one, the measurement and reference interferometers were covered with boxes. This reduces the fluctuations in the air temperature along the beam path, and thus reduces the amount of drift error in single laser FSI. In the second test, the interferometers were left uncovered and there will therefore be more fluctuations in air temperature and more drift error. Various experimental parameters for these two tests are summarised in table 4.2.

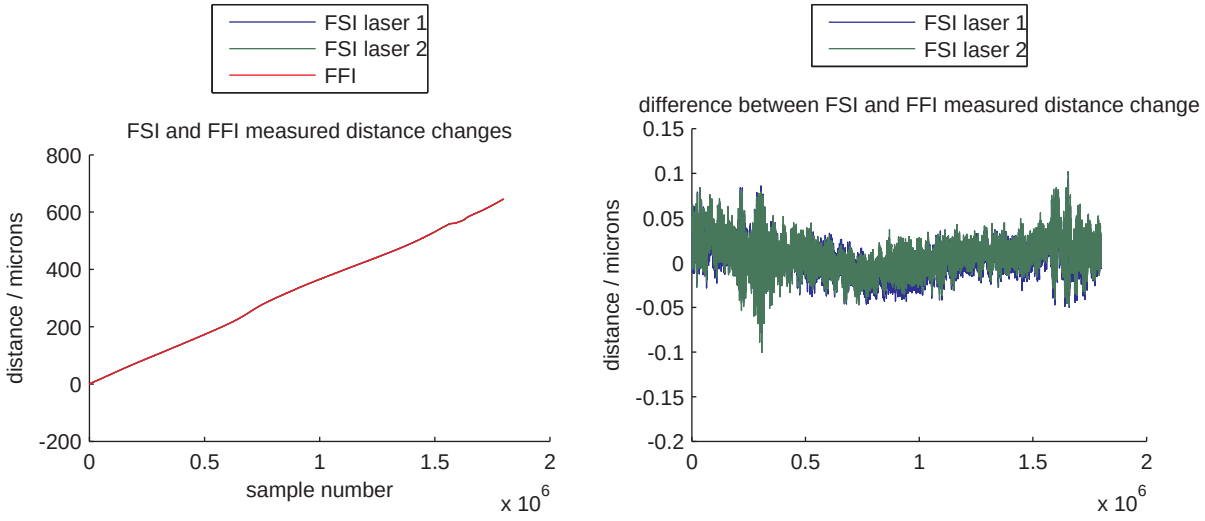


(a) Displacement (b) Difference

Figure 4.24: Movement used to calibrate $S^1$ and the reference interferometer length

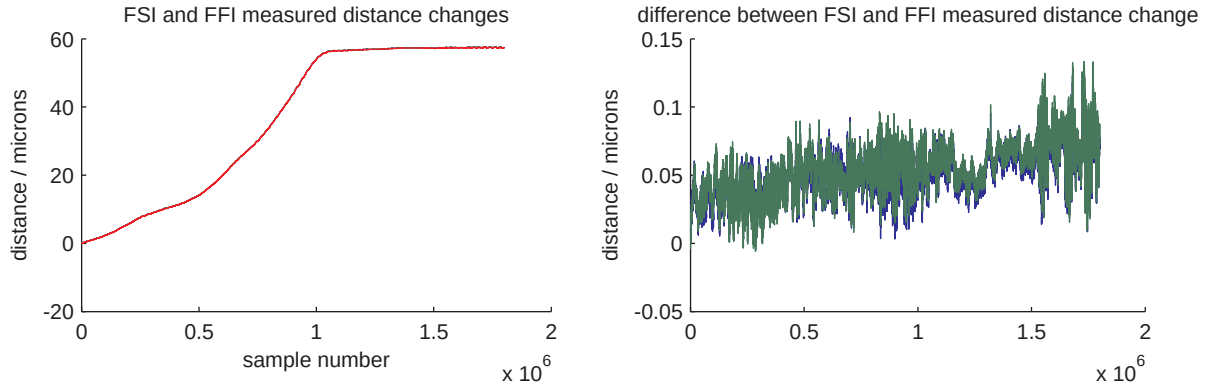


(a) Displacement (b) Difference

Figure 4.25: An unstructured movement

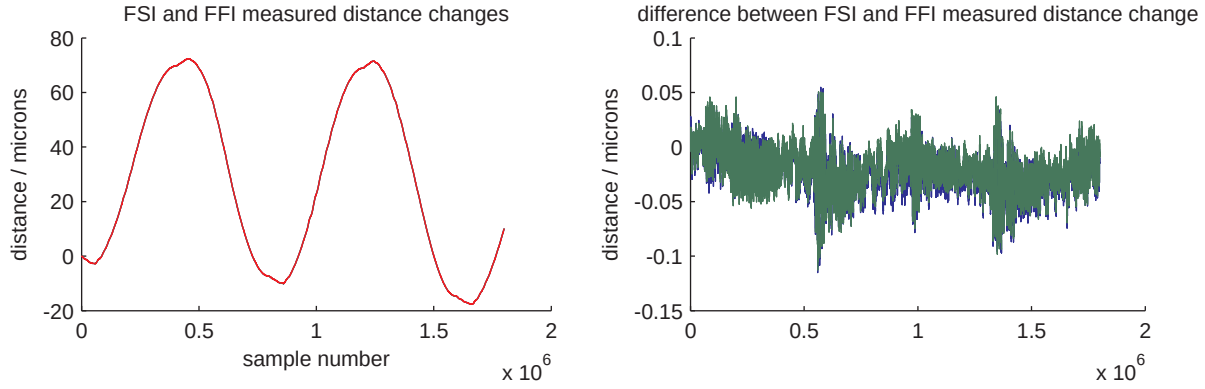


(a) Displacement (b) Difference

Figure 4.26: A cyclical movement

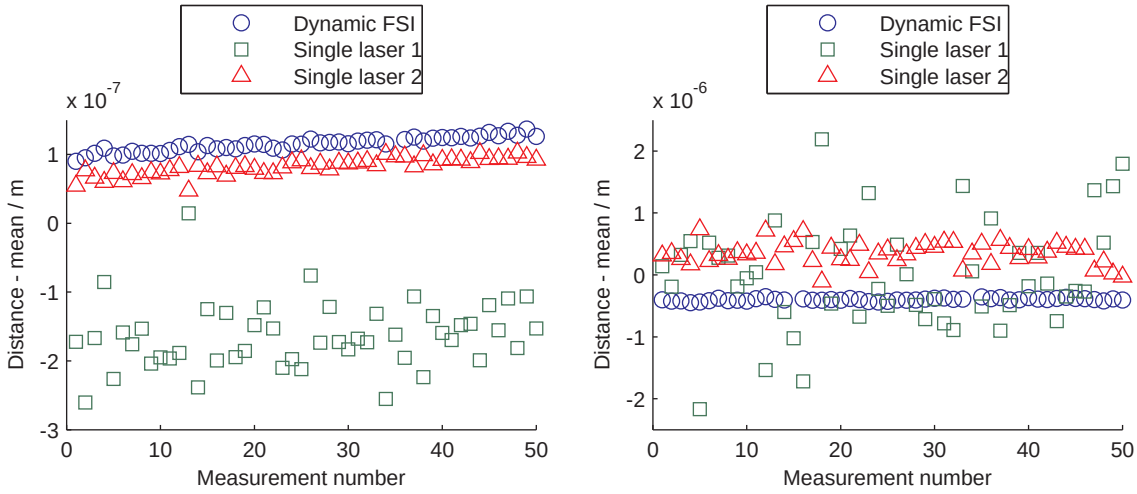


(a) Covered (b) Uncovered

Figure 4.27: Variation of repeated measurements with Dynamic FSI and single laser FSI

Figure 4.27(a) shows the results of repeated length ratio measurements when the interferometers are covered. The mean measured distance of 0.24 m has been subtracted from these values. Figure 4.27(b) shows the results of repeated length measurements when the interferometers are uncovered. The mean measured distance of 0.61 m has been subtracted from these values.

There were three outliers in the Dynamic FSI results that lie outside the range of these plots. These occurred due to an intermittent problem with laser 1, which occasionally starts its scan late and therefore the beat signal was not in the expected region of data and was not found. The location of the outliers is, in Fig. 4.27(a) (35, -1.55E-6), and in Fig. 4.27(b) (15, 8.96E-6) and (34, -7.39E-6), where the quantities in brackets indicate x and y locations, respectively.

The precision of each measurement method is determined by subtracting a straight line fit to the measured distances, and taking the standard deviation of the residuals. The results of this are listed in tables 4.3 and 4.4. In these tables, the relative precision is defined as the ratio of the standard deviation of the residuals to the mean value of measured distance.

The results in these tables are ordered as one may expect: the precision for the covered measurement is better than the precision for the uncovered measurement for any given measurement method, and for both methods, the precision of Dynamic FSI was better than

| Method | Precision (absolute) / m | Precision (relative) |
|---|---|---|
| Dynamic FSI | $3.8 \times 10^{-9}$ | $1.5 \times 10^{-8}$ |
| Laser 1 only | $4.8 \times 10^{-8}$ | $2.0 \times 10^{-7}$ |
| Laser 2 only | $6.9 \times 10^{-9}$ | $2.8 \times 10^{-8}$ |

Table 4.3: Comparison of measurement precision with covered beam paths

the precision using only laser 2, which in turn has a better precision than only using laser 1.

The uncovered measurements for the single laser analyses had a worse precision due to a larger amount of drift error in this situation. However, it is not possible to tell from this data whether the worsening of the relative precision of Dynamic FSI was due to some error source, or due to real fluctuations in the interferometer OPD caused by the greater amount of fluctuations in air refractive index.

In addition to the differences in the amount of random fluctuations in the measurements shown in Figs. 4.27(a) and 4.27(b) there is a significant systematic shift between the distances obtained with the three analyses. Any initial suspicion that this could be due to some component of drift error which is constant across all measurements must by rejected as, in this case, one would expect the Dynamic FSI results to lie in between the single laser FSI results, as these will have drift errors of opposite sign from each other. In Fig. 4.27(a) this is clearly not the case. In which case, it must be admitted that these systematic offsets are due to some systematic error or errors of unknown cause.

All three analyses ignored the effect of dispersion in air. It may be shown that single laser FSI is insensitive to dispersion as long as reference and measurement interferometers are in the same medium. However, this is not true for Dynamic FSI, which contains within it the assumption that measurements are made in a non dispersive medium. As discussed in section 1.3.2, air is only a slightly dispersive medium, and therefore this is a reasonable approximation to make. However, it may have resulted in a small error which could explain the offset in the figures.

| Method | Precision (absolute) / m | Precision (relative) |
|---|---|---|
| Dynamic FSI | $2.0 \times 10^{-8}$ | $3.3 \times 10^{-8}$ |
| Laser 1 only | $8.7 \times 10^{-7}$ | $1.4 \times 10^{-6}$ |
| Laser 2 only | $1.9 \times 10^{-7}$ | $3.1 \times 10^{-7}$ |

Table 4.4: Comparison of measurement precision with uncovered beam paths

## 4.4 Summary

In section 4.1, it was shown that, using a model based approach, one may analyse the recorded phases in a two laser, two interferometer system in such a way as to determine the OPD of the measurement interferometer at every data sampling point.

Section 4.2 contained an analysis of a crucial part of the Dynamic FSI analysis method, which is a least squares calculation. It was shown that in some situations, one proposed method of solving the least squares problem was ill conditioned. It was further shown that including an additional estimate of the parameter $S^1$ solved this problem.

An experimental demonstration and investigation of Dynamic FSI was reported in section 4.3. It was shown that the method can reconstruct a changing distance during a laser frequency sweep to better than 0.1$\mu$m precision over distances greater than 100$\mu$m. Tests were reported showing that Dynamic FSI has a higher measurement precision than single laser FSI, with repeated measurements of a fixed distance having a standard deviation of 20 nm for Dynamic FSI compared to 190 nm or 870 nm for single laser FSI with each laser, over an uncovered distance of 610 mm.

# Chapter 5

# Cascaded FSI

This chapter describes Cascaded FSI, a method that makes use of discretised errors to improve the accuracy and precision of an FSI measurement.

It uses an iterative method to estimate, in turn, the integer phase offset of a set of successively longer interferometers, utilising discrete errors to avoid a build up of measurement uncertainty during this process. This determines, with high precision, the ratios of all the interferometer OPDs and laser wavelengths involved in the measurement, allowing the use of a short, stable reference interferometer, or the use of a known wavelength as the length standard for the measurement. Either of these will enable higher accuracy measurements when compared with what I shall call *traditional* FSI methods, those which do not determine the exact value of the integer phase offset. These include the methods described in sections 3.3 and 3.4, and also Dynamic FSI as it is described in chapter 4.

The main strength of Cascaded FSI is its use of discretised errors. Other absolute distance interferometry systems that make use of discretised errors in different ways have been described in the past.

Hartmann et. al. [39] have demonstrated an absolute distance interferometry system that combines FSI with multi-wavelength interferometry. FSI is used to determine the integer phase offset corresponding to a synthetic wavelength generated by the frequency difference

between two lasers. It does this with an uncertainty less than ±0.5, and can therefore round this initial estimate to the nearest integer to obtain an improved estimate.

Coe [20] demonstrated an FSI system that has a discontinuous sweep, composed of multiple 'sub-scans'. The data from all sub-scans is processed as if they were part of a single, continuous, scan, by determining the integer number of fringes between each sub-scan with an uncertainty less than ±0.5. Rounding these initial estimates to the nearest integer calculates the correct value exactly, so the data can be treated thereafter as if it were sections from one continuous scan.

Barwood and Gill [5] have demonstrated a multi-stage absolute distance interferometry system that builds up measurement accuracy with frequency sweeps over a series of increasing ranges. All but the first sweep is discontinuous, with interferometric phase only measured at either ends of the sweep. For each sweep, the number of fringes between the two ends of the discontinuous sweep is determined unambiguously using data from the previous, smaller sweep.

The sections making up this chapter are: the theory of the measurement method, in section 5.1, an investigation of measurement uncertainties, in section 5.2, and finally an experimental analysis of the method, in section 5.3.

Material contained within this chapter relates to PCT/GB2011/051397; a patent pending invention held by Isis Innovation Limited (www.isis-innovation.com).

## 5.1 Method

The general setup required for making a Cascaded FSI measurement is shown in Fig. 5.1. The main difference from a traditional FSI setup is the addition of more interferometers.

The main data analyss steps performed in Cascaded FSI are summarised in Fig. 5.2. The reader may wish to refer back to this diagram from time to time whilst reading the relevant sections in the text.

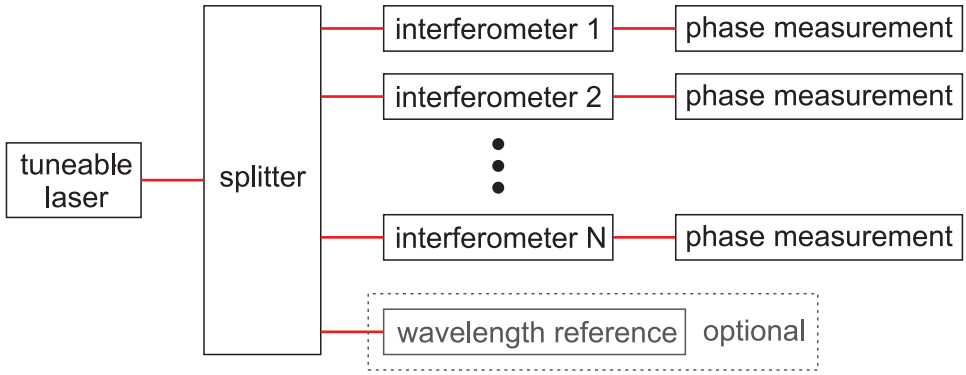


Figure 5.1: Schematic illustration of Cascaded FSI measurement setup

In traditional FSI, as described in section 3.3, there are two interferometers, each with one specific function: The measurement interferometer embodies the unknown length to be measured, and the reference interferometer acts as the reference length for the measurement. Of the multiple interferometers in Cascaded FSI, any one of interferometers 1 to N-1 may perform the function of the reference interferometer and interferometer N is the measurement interferometer.

In Cascaded FSI, interferometer 1 performs the additional function of a *bootstrap* interferometer. This is a short interferometer, such that it is possible to determine its integer phase offset exactly. In addition to these, Cascaded FSI includes multiple *intermediate* interferometers (interferometers 2 to N-1). The OPDs of the bootstrap and intermediate interferometers (numbers 1 to N-1) are arranged approximately in a geometric series (for example, the OPDs may be chosen to be $D^1 \simeq 1$ cm, $D^2 \simeq 5$ cm, $D^3 \simeq 25$ cm, $D^4 \simeq 125$ cm). The functions of the bootstrap and intermediate interferometers shall be explained in more detail later in this section.

Optionally, a wavelength reference may be included in the Cascaded FSI system. The function of this will be described later, at the end of section 5.1.1.

A Cascaded FSI measurement is made, as with both traditional FSI and Dynamic FSI, by sweeping the frequency of the laser in a continuous manner and recording the phases in all the interferometers as this is done.

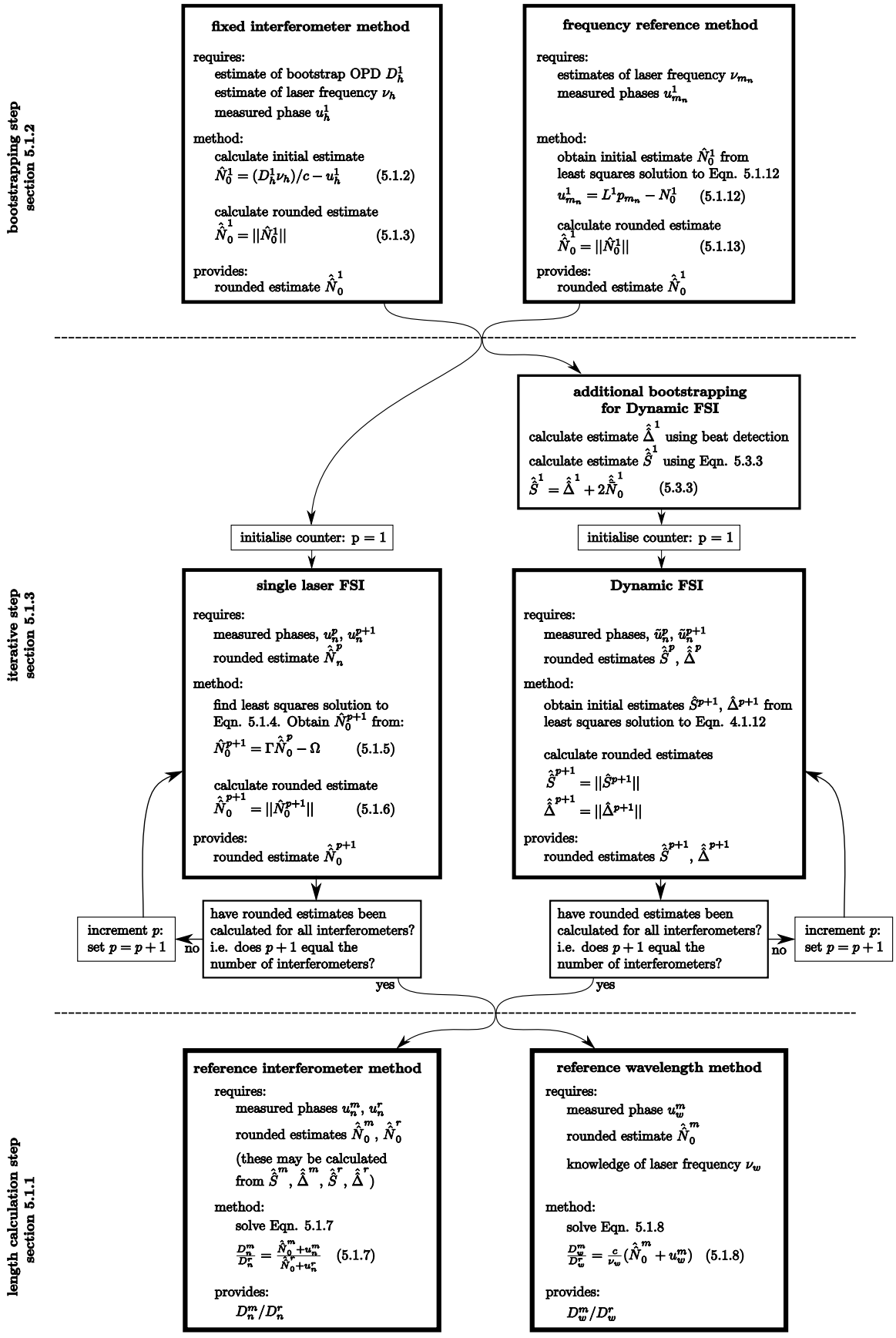


Figure 5.2: Summary of Cascaded FSI data analysis process

### 5.1.1 Summary of Cascaded FSI analysis

The phases are then analysed in a way that allows the integer phase offsets of both reference and measurement interferometer to be estimated with an uncertainty of less than ±0.5, allowing their exact values to be calculated by rounding these estimates to the nearest integer. This allows the ratios of measurement and reference interferometer OPDs to be calculated as the ratio of absolute phases of the interferometers. For a given uncertainty in phase measurement, this will give much greater precision than calculating the ratio of phase *differences* created by a scanning laser, as is done with traditional FSI methods, as the relative uncertainty on the absolute phases will be smaller than the relative uncertainty on the phase differences, as the absolute phases are much larger than the phase differences, but are known with the same absolute accuracy. This analysis procedure is an iterative one, that is initialised in what I shall call a *bootstrapping* step.

The basis of this analysis is the model of Eqn. (2.3.1), which is re-written here,

$$N_0^i + u_n^i = (D_n^i \nu_n)/c \; . \tag{5.1.1}$$

Where, as in previous chapters, $N_0^i$ is the integer phase offset, $u_n^i$ is the unwrapped phase, $D_n^i$ is the interferometer OPD, $\nu_n$ is the laser frequency and $c$ is the speed of light. The $i$ superscripts index the interferometers and the $n$ subscripts index the ADC samples. Refer back to section 2.3 for a full description of this notation.

#### Bootstrapping step

This step estimates the integer phase offset of the bootstrap interferometer. There are several ways this could be done, which shall be discussed in more detail later, but as a simple example, we could estimate this using a-priori information about the bootstrap interferometer's OPD and the laser frequency at some sampling index, $h$. Rearranging Eqn. (5.1.1) gives an estimate,

$$\hat{N}_0^1 = (D_h^1 \nu_h)/c - u_h^1 \; . \tag{5.1.2}$$

The measurement system must be arranged so that the estimate, $\hat{N}_0^1$, has an uncertainty less than $\pm 0.5$ with a high confidence level. This may be done by making the bootstrap interferometer's OPD small, for example. As the system is arranged such that the error on $\hat{N}_0^1$ is very likely to be less than $\pm 0.5$, then rounding this estimate to the nearest integer is equally likely to calculate the exactly correct value,

$$\hat{\hat{N}}_0^1 = ||\hat{N}_0^1|| \, . \tag{5.1.3}$$

**Iterative step**

Equipped with the exact value for the integer phase offset of the shortest interferometer, Cascaded FSI then proceeds to calculate the exact value for the integer phase offset of all other interferometers using an iterative procedure. With an iteration index, $p$, set initially to 1, the known integer phase offset of the $p^{\text{th}}$ interferometer, together with recorded phases during the laser frequency sweep, is used to calculate the integer phase offset of the next, $(p+1)^{\text{th}}$ interferometer. There are several ways in which this could be done, which are discussed in more detail later in section 5.1.3.

One method is to take the recorded phases from the pair of interferometers, $p$ and $(p+1)$, and to perform a straight line fit to these phases as is done for standard single laser FSI, described in section 3.3.3. The equation for this straight line fit, Eqn. (3.3.8), is rewritten here,

$$u_n^{p+1} = (D^{p+1}/D^p)u_n^p + \left((D^{p+1}/D^p)N_0^p - N_0^{p+1}\right) . \tag{5.1.4}$$

A least squares fit may be used to estimate the gradient, $\Gamma$, and offset, $\Omega$ of this line. $\Gamma$ is thus an estimate of $(D^{p+1}/D^p)$, and $\Omega$ is an estimate of $((D^{p+1}/D^p)N_0^p - N_0^{p+1})$. Given that we have an estimate for $N_0^p$ from the previous iteration (or from the bootstrap calculation, if this is the first iteration) we may then calculate an initial estimate of $N_0^{p+1}$ by combining the estimates of $\Gamma$ and $\Omega$ to eliminate $(D^{p+1}/D^p)$ and rearranging to obtain

$$\hat{N}_0^{p+1} = \Gamma \hat{\hat{N}}_0^p - \Omega \, . \tag{5.1.5}$$

The system is arranged such that the estimate of $\hat{N}_0^{p+1}$ has an uncertainty less than $\pm 0.5$ with a high confidence level (the requirements for this are discussed later in section 5.1.3). Therefore rounding $\hat{N}_0^{p+1}$ to the nearest integer is very likely to give the exact value for the integer phase offset,

$$\hat{\hat{N}}_0^{p+1} = ||\hat{N}_0^{p+1}|| \ . \tag{5.1.6}$$

This process is iterated over, incrementing $p$ each time, until improved estimates, $\hat{\hat{N}}_0^{p+1}$, have been calculated for all interferometers, including the measurement interferometer.

**Length calculation step**

Once all the integer phase offsets are determined, the OPD of the measurement interferometer, $m$, can be determined relative to either the OPD of the reference interferometer, or relative to a known wavelength[1].

To determine the measurement OPD relative to the reference interferometer OPD, copies of Eqn. (5.1.1) for these two interferometers are combined to obtain

$$D_n^m = D_n^r \frac{N_0^m + u_n^m}{N_0^r + u_n^r} \ , \tag{5.1.7}$$

where the $r$ superscript identifies the reference interferometer. Note the similarity to the single laser FSI distance calculation, Eqn. (3.3.4), with the difference being that here, the OPD ratios are calculated as the ratio of the absolute phases of the interferometers.

Also note the similarity to the Dynamic FSI distance calculation, Eqns. (4.1.2). The difference here is that the integer phase offsets, $N_0^m$ and $N_0^r$ have been determined with discretised errors and are therefore known more precisely than in Dynamic FSI.

From Eqn. (5.1.7) it is possible, as with Dynamic FSI, to calculate the measurement interferometer OPD at every sampling point. However this does not mean that Cascaded FSI has an inbuilt immunity to drift error, as Dynamic FSI does: If only one laser is used,

[1]The measurement interferometer is still interferometer number $N$, but for ease of reading it shall be referred to from now on with a superscript, $m$, for 'measurement'.

as with the analysis of Eqn. (5.1.4), then a measurement interferometer OPD that varies above some threshold level during the laser scan will create a drift error large enough such that the wrong value for $N_0^m$ will be calculated, and the measurement will give an incorrect result.

To determine the measurement OPD relative to a known wavelength, the optional wavelength reference must be included. This will provide information that at some sampling index, $w$, the laser had a known frequency, $\nu_w$. The OPD of the measurement interferometer may then be determined relative to this known frequency by rearranging Eqn. (5.1.1) to obtain

$$D_w^m = \frac{c}{\nu_w}\left(N_0^m + u_w^m\right) \ . \tag{5.1.8}$$

**Comments**

Cascaded FSI is in some ways similar to Dynamic FSI, in that it is a measurement technique that contains two steps: the first step for both methods is to obtain estimates for the integer phase offsets of interferometers in the system. Once these are obtained, the ratios of interferometer OPDs may be calculated from Eqn. (4.1.2) for Dynamic FSI, or from Eqn. (5.1.7) for Cascaded FSI. Alternatively, Cascaded FSI may calculate length relative to a wavelength standard, using Eqn. (5.1.8).

The key part of the Cascaded FSI method is the rounding step. This exploits the discrete nature of the integer phase offset to enable a higher precision measurement of interferometer OPDs, provided we have an initial estimate of the integer phase offset with an uncertainty of less than $\pm 0.5$ to a high confidence level. Traditional FSI measurements only measure the *ratio* of two interferometer OPDs, and therefore also only the *ratio* of the integer phase offsets. A rounding step cannot be used here, as this requires an estimate of the *absolute* value of the integer phase offset. However, if we are able to estimate the absolute value of the integer phase offset for any one interferometer, as is done in the bootstrapping step, then we may multiply this with the FSI-obtained ratio of integer phase offsets to estimate the absolute value of the integer phase offset in any other interferometer. If this estimate

has a low enough uncertainty, we may make use of a rounding step to further reduce its uncertainty.

The reason for the iterative nature of this method is the combination of three factors: We must be able to estimate the integer phase offset of the bootstrap interferometer with an uncertainty less than $\pm 0.5$; it is easier to do this with a short bootstrap interferometer; and the uncertainty of FSI measurements scales with the ratio of interferometer lengths.

The rest of this section shall describe the bootstrapping and iteration steps in more detail, presenting more sophisticated methods for computing estimates of $N_0^i$, and investigating what conditions must be met to keep the uncertainty on these estimates below the $\pm 0.5$ fringe threshold.

### 5.1.2 Bootstrapping step

The Cascaded FSI analysis starts by determining the integer phase offset of the bootstrap interferometer. A simple way of doing this was presented above in the form of Eqn. (5.1.2). Both a 'fixed interferometer method' and an alternative, 'frequency reference', method will be described here. The 'frequency reference' method will be used in the experimental investigation of Cascaded FSI, in section 5.3.

#### Fixed interferometer method

The integer phase offset of the bootstrap interferometer, $N_0^1$, may be calculated directly if the bootstrap interferometer OPD, $D_h^1$, and laser frequency, $\nu_h$, are known for some ADC sampling index, $h$. The calculation for this was given above, as Eqn. (5.1.2).

However, the bootstrapping step must determine the integer phase offset with an uncertainty less than $\pm 0.5$. The standard uncertainty on the estimate of Eqn. (5.1.2) is

$$\sigma_{\hat{N}_0^1} = \frac{D_h^1}{c}\sigma_{\nu_h} \oplus \frac{\nu_h}{c}\sigma_{D_h^1} \oplus \sigma_{u_h^1} \ . \tag{5.1.9}$$

The uncertainty in phase measurement, $\sigma_{u_h^1}$, can easily be made significantly less than $\pm 0.5$, so this term may safely be neglected. This leaves the terms due to uncertainty in laser frequency and interferometer OPD. Both these terms may be made small by choosing a sufficiently short length for the bootstrap interferometer: This directly reduces the $\sigma_{\nu_h}$ term, which is proportional to $D_h^1$, and a shorter interferometer will also be more stable, reducing $\sigma_{D_h^1}$, so we can rely on having measured $D^1$ beforehand using an independent method. This measurement can be thought of as a calibration step.

A practically achievable set of values for this equation could be: a bootstrap interferometer OPD of $D_h^1 = 0.1$ m; a laser frequency of approximately $\nu_h = 200$ THz; an uncertainty in laser frequency of $\sigma_{\nu_h} = 600$ MHz; an uncertainty on the bootstrap interferometer OPD of 1 in $10^6$ of its length, $\sigma_{D_h^1} = 0.1$ $\mu$m and a phase measurement uncertainty of $\sigma_{u_h^1} = 0.01$. In this case the uncertainty on $\hat{N}_h^1$ would be 0.21, which is smaller than the $\pm 0.5$ upper limit.

Although this method seems feasible, it does require a well calibrated and carefully stabilised OPD for the bootstrap interferometer. This must be stable enough to maintain its length sufficiently between calibrations, which could be a time period of weeks or months. If one wished to put this method into practice, an alternative and potentially more robust option may be to use dual wavelength interferometry to determine the integer phase offset of the bootstrap interferometer, which will greatly reduce the requirements on the uncertainty of the bootstrap interferometer OPD due to the longer ambiguity range of this method. However, this comes at the expense of a more complicated measurement setup.

### Frequency reference method

An alternative method of calculating the integer phase offset of the bootstrap interferometer, $N_0^1$, is available if we know the absolute frequency of the tuning laser at two or more different points during the frequency sweep.

The laser's absolute frequency may be determined by splitting off some of its light, and measuring the fraction of this optical power that is transmitted through a gas absorption

cell. These cells are transparent cylinders with closed ends, filled with a specified gas at a known pressure, for a given temperature. For most frequencies in the range of the laser's sweep, this gas is transmissive, but in narrow bands around certain frequencies the gas will absorb the laser light. These bands are known as absorption peaks. The frequencies at which these absorption peaks occur are determined by the physics of the light-gas interaction. For most gasses this is fairly insensitive to external conditions such as temperature and thus the frequencies are highly reproducible. Once they have been calibrated, they may be used as accurate frequency references. By finding the times during the laser frequency sweep that match the centres of absorption peaks, we may accurately determine the frequency of the tuning laser at those times. The sampling indices at these points are labelled as $m_1$, $m_2$, etc. such that the frequencies $\nu_{m_1}$, $\nu_{m_2}$, etc. are known values.

The integer phase offset of the bootstrap interferometer is determined by fitting a straight line to bootstrap interferometer phase, $u^1_{m_n}$, versus absolute laser frequency, $\nu_{m_n}$, for all sampling indices, $m_n$, for which the absolute laser frequency is known. When doing this, we must explicitly take account of the refractive index of the medium the bootstrap interferometer is in. Equation (5.1.1) is therefore rewritten here with the refractive index, $n(\nu)$, included explicitly,

$$N^1_0 + u^1_n = \frac{2L^1 n(\nu_n)\nu_n}{c} \ . \tag{5.1.10}$$

It shall be convenient to define a quantity, $p_{m_n}$, as follows,

$$p_{m_n} = \frac{2n(\nu_{m_n})\nu_{m_n}}{c} \ . \tag{5.1.11}$$

Using this definition, Eqn. (5.1.10) is written in the canonical form for a straight line $y = mx + c$,

$$u^1_{m_n} = L^1 p_{m_n} - N^1_0 \ . \tag{5.1.12}$$

A least squares fit is made to this line to calculate estimates for $L^1$ and $N^1_0$. In this way, the frequency reference method calculates an initial estimate for the integer phase offset of the bootstrap interferometer, $\hat{N}^1_0$.

An improved estimate for $N_0^1$ is then calculated by rounding the first estimate to the nearest integer value,

$$\hat{\hat{N}}_0^1 = ||\hat{N}_0^1|| \ . \tag{5.1.13}$$

For this step to have the desired effect, the uncertainty on the initial estimate should be less than $\pm 0.5$.

A simple calculation for the uncertainty on the initial estimate, $\hat{N}_0^1$, is given here, considering the case that we only make use of two known frequencies in the laser scan, with sampling indices $m_1$ and $m_2$. In reality we may make use of more, which should decrease the uncertainty on our estimate, so this calculation can be considered as an upper bound on the uncertainty. In this case an initial estimate for the integer phase offset of the bootstrap interferometer is made without the use of least squares as,

$$\hat{N}_0^1 = \frac{u_{m_1}^1 \nu_{m_2} - u_{m_2}^1 \nu_{m_1}}{\nu_{m_1} - \nu_{m_2}} \ .$$

The standard uncertainty on this estimate is

$$\sigma_{\hat{N}_0^1} = \frac{\nu_{m_1} \oplus \nu_{m_2}}{\nu_{m_1} - \nu_{m_2}} \left( \sigma_u \oplus \frac{D}{c} \sigma_\nu \right) \ .$$

This bootstrapping method was investigated experimentally, with results presented in section 5.3.4. Using the furthest separated pair of absorption features in this experiment as an example to provide values for $\nu_{m_1}$ and $\nu_{m_2}$, the above equation becomes

$$\sigma_{\hat{N}_0^1} = 70.8 \left( \sigma_u \oplus \frac{D}{c} \sigma_\nu \right) \ .$$

The absorption peak width is approx 300 MHz, so if their centres can be located with a modest uncertainty of $1/10^{\text{th}}$ of their width, then $\sigma_\nu = 30$ MHz. Neglecting the uncertainty due to $\sigma_u$, the requirement that $\sigma_{\hat{N}_0^1} < 0.5$ leads to a requirement on $D$: $D < 0.07$ m. Making use of more than two absorption features should only decrease the uncertainty on this estimate, so therefore this simple calculation indicates that this method is feasible, and

provides an indication of what a sufficiently short length for a bootstrap interferometer is.

### 5.1.3 Iterative step

This section describes the procedure whereby the integer phase offset of the $(p+1)^{\text{th}}$ interferometer is calculated, using knowledge of the integer phase offset of the $p^{\text{th}}$ interferometer and measured phases during the laser scan. This process is initialised using the bootstrapping step to calculate the integer phase offset of the $1^{\text{st}}$ interferometer.

Two alternative methods for performing the iterative step are described. The first uses single laser FSI, and second makes use of Dynamic FSI. This second method is the one used in the experimental investigation of section 5.3.

#### Single laser FSI

The iterative step may be performed with a linear fit to the recorded phases during a laser frequency sweep, as in Eqn. (5.1.5). The estimate of $N_0^{p+1}$ obtained from this must have an uncertainty less than $\pm 0.5$ at every iteration.

A simple expression for the uncertainty on this estimate may be obtained by considering a calculation only using the initial and final phase measurements, $u_0^i$ and $u_f^i$. In reality, we will likely make use of more than two phase measurements, which will reduce the uncertainty due to random phase errors. For just two phase measurements, the estimate may be computed without least squares as

$$\hat{N}_0^{p+1} = \frac{\hat{\hat{N}}_0^p(u_0^{p+1} - u_f^{p+1}) + u_f^p u_0^{p+1} - u_0^p u_f^{p+1}}{u_0^p - u_f^p} \ .$$

The standard uncertainty on this estimate is

$$\sigma_{\hat{N}_0^{p+1}} = \left(\frac{\nu_0 \oplus \nu_f}{\nu_0 - \nu_f}\right)\left(1 \oplus \frac{D^{p+1}}{D^p}\right)\sigma_u \ .$$

As an example, consider a laser frequency scan of $\Delta\nu = 10$ THz with a central frequency of 200 THz, with a phase measurement uncertainty of $1/500^{\text{th}}$ of a fringe, $\sigma_u = 0.005$. Inserting these values into the above expression and requiring that $\sigma_{\hat{N}_0^{p+1}} < 0.5$ gives

$$\frac{D^{p+1}}{D^p} < 3.5 \ ,$$

and thus the iterative step would be expected to work reliably if the ratio of interferometer OPDs at each iteration was less than 3.5. We may choose, therefore, to have the OPD ratios of the intermediate interferometers equal to 2 at each step, forming a geometric series of length with factor 2.

### Dynamic FSI

An alternative method for the iterative step makes use of Dynamic FSI. To do this, we use two tuning lasers instead of one, and record the phase corresponding to both of them in all interferometers as their frequencies are swept. Having done this, the iterative step can then make use of the unwrapped phases from two lasers, using part of the Dynamic FSI analysis method.

In order to use Dynamic FSI for the iteration steps, the bootstrapping step must determine the integer phase offset in the bootstrap interferometer corresponding to both lasers. This may be done using either of the methods described in section 5.1.2, or using an alternative method that will be introduced in section 5.3.4. With this done, we have estimates $\hat{\hat{S}}^1$ and $\hat{\hat{\Delta}}^1$, as required for the first iteration (recall that $S^i$ and $\Delta^i$ are an alternative way of expressing $N_0^i$ and $\bar{N}_0^i$ in terms of sum and difference components).

The measured values used by each iterative step are, the integer phase offsets of the $p^{\text{th}}$ interferometer, $\hat{\hat{S}}^p$ and $\hat{\hat{\Delta}}^p$, and the unwrapped phases from both lasers in the $p^{\text{th}}$ and $(p+1)^{\text{th}}$ interferometer, $\tilde{u}_n^p$ and $\tilde{u}_n^{p+1}$ respectively. This information is inserted into the Dynamic FSI 'cascaded' solution option, Eqn. (4.1.12). Solving this least squares problem obtains estimates for $S^{p+1}$ and $\Delta^{p+1}$.

These initial estimates are then rounded to the nearest integer to compute estimates with discretised errors:

$$\hat{\hat{S}}^{p+1} = ||\hat{S}^{p+1}|| \,,$$
$$\hat{\hat{\Delta}}^{p+1} = ||\hat{\Delta}^{p+1}|| \,.$$

These estimates are then used as the known values of integer phase offsets for the next iteration. The process is repeated until estimates have been obtained for the integer phase offsets of all interferometers.

## 5.2 Uncertainty analysis

This section presents an analysis comparing the uncertainty of Cascaded FSI with that of traditional FSI.

### 5.2.1 Uncertainty equations

Expressions shall be found here for the uncertainty on the calculated length in traditional and Cascaded FSI, due to uncertainties in measured phase values, lengths, and wavelengths.

#### Traditional FSI

As described in section 3.3.1, in single laser FSI, the length of the measurement interferometer, $D^m$, may be calculated as the length of the reference interferometer, $D^r$, multiplied by the ratio of phase advances in each interferometer $\Delta u^m/\Delta u^r$, measured during the laser frequency sweep,

$$D^m = D^r \frac{\Delta u^m}{\Delta u^r} \,.$$

This equation is chosen to represent traditional FSI methods because it is simple and captures the essential features of these methods. Drift error shall not be included in this calculation.

The standard uncertainty on the above length calculation is

$$\frac{\sigma_{D^m}}{D^m} = \frac{\sigma_{D^r}}{D^r} \oplus \frac{\sigma_{\Delta u^m}}{\Delta u^m} \oplus \frac{\sigma_{\Delta u^r}}{\Delta u^r}$$

rearranging, and making use of Eqn. (5.1.1), this may be rewritten as

$$\sigma_{D^m} = D^m \left( \frac{\sigma_{D^r}}{D^r} \oplus \frac{\sqrt{2}\Lambda\sigma_{u^r}}{D^r} \right) \oplus \sqrt{2}\Lambda\sigma_{u^m} \ ,$$

where $\Lambda$ is the synthetic wavelength created by the laser wavelengths at the beginning, $\lambda_0$, and end, $\lambda_f$ of the laser frequency sweep, $\Lambda = c/\Delta\nu = \lambda_0\lambda_f/(\lambda_0 - \lambda_f)$.

**Cascaded FSI using reference interferometer**

In Cascaded FSI, length may be calculated relative to a physical length standard as stated in Eqn. (5.1.7),

$$D^m = D^r \frac{N_0^m + u^m}{N_0^r + u^r} \ .$$

The standard uncertainty on the above estimate of $D^m$ is

$$\frac{\sigma_{D^m}}{D^m} = \frac{\sigma_{D^r}}{D^r} \oplus \frac{\sigma_{(N_0^m+u^m)}}{N_0^m + u^m} \oplus \frac{\sigma_{(N_0^r+u^r)}}{N_0^r + u^r} \ , \tag{5.2.1}$$

where the $n$ subscript has been omitted as it is not needed here. Assuming that the integer phase offsets were calculated correctly in the rounding step, there is no error on these, and so $\sigma_{(N_0^m+u^m)} = \sigma_{u^m}$, and similarly $\sigma_{(N_0^r+u^r)} = \sigma_{u^r}$. Inserting these, and making use of Eqn. (5.1.1), the uncertainty may be rewritten as

$$\sigma_{D^m} = D^m \left( \frac{\sigma_{D^r}}{D^r} \oplus \frac{\lambda\sigma_{u^r}}{D^r} \right) \oplus \lambda\sigma_{u^m} \ .$$

A more in depth-analysis should of course take into account the probability of making an error in determining the integer phase offset. However, I propose, backed up by the experimental investigation of section 5.3, that it is possible to reduce the probability of

making such an error in a system using discrete errors to be vanishingly small, as is the case in the example field of digital communications and data storage that was mentioned earlier in this thesis. The goal of this section is to show what measurement uncertainties are possible if this is achieved, and for this reason the possibility of discrete errors are neglected in the above calculation, and throughout this section.

**Cascaded FSI using reference wavelength**

In Cascaded FSI, length also may be calculated relative to a known wavelength, as stated in Eqn. (5.1.8),

$$D^m = \frac{c}{\nu_h} \left( N_0^m + u_h^m \right) \ .$$

Assuming that no discrete error has been made, there is no uncertainty on the $N_0^m$ term, so the standard uncertainty on the above estimate of $D^m$ is then

$$\sigma_{D^m} = D^m \left( \frac{\sigma_{\lambda_{cal}}}{\lambda} \oplus \frac{\sigma_{\lambda_{meas}}}{\lambda} \right) \oplus \lambda \sigma_{u^m} \ .$$

Here, two contributions to the wavelength uncertainty are included explicitly: $\sigma_{\lambda_{meas}}$ is the uncertainty in the measurement of the ratio of our laser's wavelength and the calibrated value of the reference wavelength, whereas $\sigma_{\lambda_{cal}}$ is the uncertainty in the calibrated value of the reference wavelength.

### 5.2.2 Comparison

I shall now compare the uncertainties of the three methods considered above. For convenience, these results are collected together here,

$$\sigma_{D^m} = D^m \left( \frac{\sigma_{D^r}}{D^r} \oplus \frac{\sqrt{2}\Lambda\sigma_{u^r}}{D^r} \right) \oplus\sqrt{2}\Lambda\sigma_{u^m} \quad \text{(traditional)} \quad (5.2.2)$$

$$\sigma_{D^m} = D^m \left( \frac{\sigma_{D^r}}{D^r} \oplus \frac{\lambda\sigma_{u^r}}{D^r} \right) \oplus\lambda\sigma_{u^m} \quad \text{(Cascaded, reference interferometer)} \quad (5.2.3)$$

$$\sigma_{D^m} = D^m \left( \frac{\sigma_{\lambda_{cal}}}{\lambda} \oplus \frac{\sigma_{\lambda_{meas}}}{\lambda} \right) \oplus\lambda\sigma_{u^m} \quad \text{(Cascaded, reference wavelength)} \quad (5.2.4)$$

The above equations all have the same form. They all contain three terms that can be interpreted as having similar causes for each of the methods. Each of these terms shall now be considered in turn.

#### Knowledge of reference length

The first term on the left of each equation (e.g. $D^m\sigma_{D^r}/D^r$ for traditional FSI) is the uncertainty in the calibration of the length standard used for the measurement.

The first two methods use a reference interferometer as a length standard, so this term has exactly the same form for these. For these methods, the presence of this term simply shows that the relative uncertainty on the measured length is at least equal to the relative uncertainty on the reference length.

So, to minimise this contribution we would like to minimise the relative uncertainty on the knowledge of the reference interferometer OPD, $\sigma_{D^r}/D^r$. Assuming that reasonable effort is put into calibrating this length, the dominant factor on this uncertainty is likely to be the stability of the reference interferometer: Changes in ambient conditions, most importantly temperature, will cause the reference interferometer to change its OPD over time, leading to uncertainty in what its length is at any given time. In order to minimise this uncertainty, we would like to be able to monitor or control these ambient conditions, which will be easier to

do if the reference interferometer is short. Therefore a small $D^r$ will make a small $\sigma_{D^r}/D^r$ practically easier to achieve. However, there is also a disadvantage to using a short reference interferometer, as shall be seen when we consider the next term.

The third method measures length relative to a known wavelength, so the uncertainty term from this is the relative uncertainty in the knowledge of this wavelength. As was discussed in section 1.3.1, wavelength references generally offer better stability than physical length references, and for this reason wavelength referenced Cascaded FSI has the potential for the smallest uncertainty in this first term.

**Realisation of reference length**

The second term in each equation (e.g. $D^m\sqrt{2}\Lambda\sigma_{\Delta u^r}/D^r$ for traditional FSI) relates to how well each method can *realise* its reference length.

This is most straightforward to appreciate for the third method, Cascaded FSI using a reference wavelength. We may use a gas absorption cell, for example, with the frequency of a certain absorption peak having been accurately calibrated. However, if we were to use a noisy photodiode, and not correct for laser intensity variations, then we would have a large uncertainty on the location of this peak in our data. In this case we will not benefit from the accuracy of the calibration as we have poorly realised our reference length in the measurement.

So, for Cascaded FSI using a reference wavelength, this term is simply the relative uncertainty in determining the tuning laser's wavelength relative to the wavelength reference.

For the other two methods, that use physical length artefacts, the uncertainty on the realisation of the reference length is due to uncertainty on phase measurements in the reference interferometer. The difference in these two methods is due to the fact that Cascaded FSI determines the integer phase offset of the reference interferometer. This means that Cascaded FSI calculates the ratio of reference interferometer OPD to laser frequency, whereas traditional FSI determines the ratio of reference interferometer OPD to the synthetic frequency

created by the frequency difference during the laser scan. This means that the uncertainty on the phase measurement accuracy is multiplied by $\lambda/D^r$ for Cascaded FSI, as opposed to $\Lambda/D^r$ for traditional FSI.

The uncertainty term for Cascaded FSI is smaller than the term for traditional FSI by the ratio $\Lambda/\lambda$. The size of this ratio is determined by the tuning range of the laser. The most widely tuneable lasers currently available have tuning ranges of approximately 100 nm around 1550 nm, making this ratio approximately 15. Therefore, for such a laser, this uncertainty term would be 15 times smaller for Cascaded FSI than for traditional FSI.

These terms are also inversely proportional to the length of the reference interferometer. With this above example, this means that with Cascaded FSI, the reference interferometer could be made up to 15 times shorter before the uncertainty from this term equals that for traditional FSI. As was mentioned previously, there are advantages to having a small reference interferometer. Because this term is so much smaller for Cascaded FSI, it is therefore possible for Cascaded FSI to use a short reference interferometer without this term dominating the uncertainty of the measurement.

**Realisation of measurement length**

The third term in each equation does not scale with measurement distance, and is due to uncertainty in phase calculation in the measurement interferometer. This term is the same for both forms of Cascaded FSI here, so in this case there is a simple distinction between traditional, and Cascaded FSI. Traditional FSI does not determine the integer phase offset of the measurement interferometer, and so measures relative to the synthetic wavelength, $\Lambda$. Therefore the measurement uncertainty is multiplied by this. Cascaded FSI determines the integer phase offset of the measurement interferometer, and therefore measures relative to the actual laser wavelength, $\lambda$. As was stated above, this will be a factor of at least 15 times smaller than the synthetic wavelength, and therefore these uncertainty terms will be smaller by this ratio for the Cascaded FSI measurements.

## 5.3 Experimental test

This section contains an experimental demonstration and investigation of Cascaded FSI. Of the various options discussed in section 5.1, the frequency reference method is used for the bootstrapping step, and Dynamic FSI is used for the iterative step.

### 5.3.1 Equipment layout

The experimental setup is shown in Fig. 5.3. It is similar to the setup used for Dynamic FSI (Fig. 4.12), with the main differences being the inclusion of two additional interferometers, and a gas absorption cell filled with acetylene $^{12}C_2H_2$ (labelled 'acetylene cell'). Various experimental parameters are summarised in table 5.1.

As with the Dynamic FSI setup, the optical outputs of the two fibre coupled, tuneable lasers are connected to a fibre splitter tree. Laser 1 is an Agilent 81640A tuneable laser module housed in an Agilent 8164A mainframe, and laser 2 is a Santec TSL-510-A tuneable laser. The internal structure of the splitter tree is shown in Fig. 4.13.

Some of the light from laser 2 is split off, using a 50:50 fibre splitter and sent into the acetylene cell, which is a Thorlabs CQ09050-CH12 gas cell, 5cm in length, and filled with acetylene $^{12}C_2H_2$ to a pressure of 6.7 kPa (50 Torr). The remaining light entering the fibre splitter is sent through a variable attenuator, adjusted such that the light entering the splitter from both lasers has approximately equal power.

The combined light from both lasers exits the splitter tree from outputs 1-5. Outputs 1-4 are sent to Michelson interferometers, of which 1-3 are labelled in order of increasing OPD, and interferometer 4 has a variable OPD.

Light from output 5 of the splitter tree was sent through a variable attenuator then directly onto a photodiode. This was used to detect a beat signal that is observable with this photodiode when both tuning lasers have frequencies within a few MHz of each other, as described in section 4.3.2.

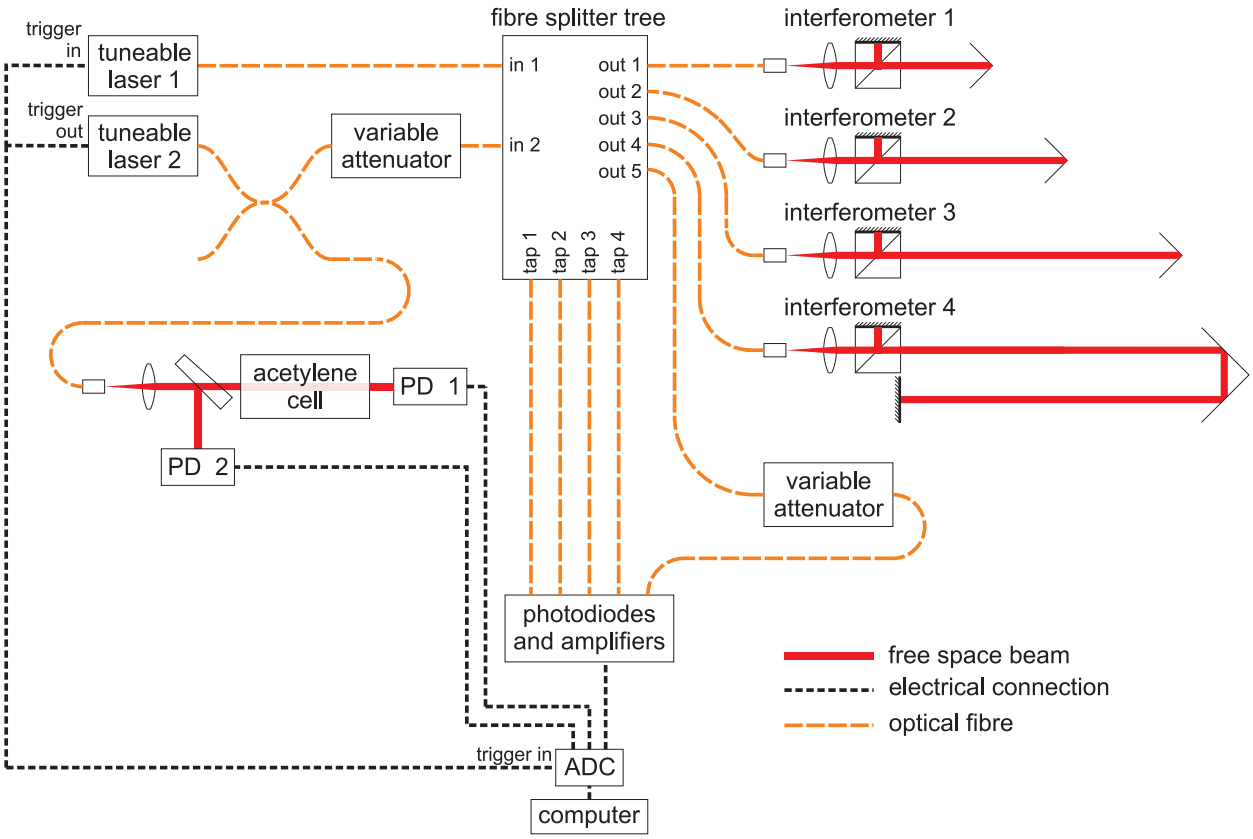


Figure 5.3: Experimental setup for investigation of Cascaded FSI

Light split off from laser 2 is collimated and sent through a wedged 50:50 plate beam-splitter. The transmitted light from this is sent through the acetylene cell onto photodiode 1. The reflected light from the beam-splitter is sent directly onto photodiode 2. This is used to compensate for laser intensity variations. Photodiodes 1 and 2 are Thorlabs PDA400s.

Apart from the two numbered photodiodes used in the acetylene cell part of the setup, the photodiode and amplifier electronics are on a board developed in-house, with the amplified signals sent via BNC cables to the ADC, which is a pair of National Instruments PCI-6115, 4 channel, 12 bit ADCs with acquisition synchronised using a common clock signal. The sampling rate of 2 MS/s is chosen to be high enough to record the transient beat signal occurring when both lasers have the same optical frequency.

To make a measurement, the frequency of both lasers is swept in a continous manner in opposite directions and with significantly different speeds whilst simultaneously recording the voltages from all the photodiodes with the ADC. This requires starting the laser scans

| Parameter | Value |
|---|---|
| ADC sampling rate | 2 MS/s |
| ADC anti-aliasing filter frequency* | 500kHz |
| Laser 1 wavelength scan settings | 1550 nm → 1570 nm at +20nm/s |
| Laser 2 wavelength scan settings | 1610 nm → 1510 nm at -100nm/s |
| Laser 1 power | 0.2 mW |
| Laser 2 power | 2.0 mW |
| Interferometer 1 length | (45 ± 5) mm |
| Interferometer 2 length | (65 ± 5) mm |
| Interferometer 3 length | (205 ± 5) mm |
| Interferometer 4 length | variable |

Table 5.1: Summary of equipment settings for Cascaded FSI test measurements. The interferometer lengths are rough estimates from ruler measurements. * The anti-aliasing filter was turned off for the channel used to detect the beat signal.

and ADC acquisition simultaneously. Laser 2 is used to control the measurement start times. It is set to perform either a single or repeated sweeps, and outputs a trigger signal at the start of a sweep. This is connected via BNC cables to trigger inputs on laser 1 and the ADC, which start scanning and recording respectively upon receiving a trigger signal.

The lasers were set to vary their wavelengths as described in table 5.1. The wavelength ranges were chosen such that the two tuning lasers will have the same optical frequency at one point during the measurement period, and a transient beat signal can be measured to determine when this happens. Information gained from this is used in the Dynamic FSI part of the iterative step. The wavelength variation rates were chosen such that the FSI signal frequencies produced by each laser are different from each other, and can thus be separated in the frequency domain as described in section 4.3.2.

Laser 2 is set to a higher output power than laser 1 as half of this power is redirected to the acetylene cell via a 50:50 fibre splitter. The 2 mW power of laser 2 was chosen to match the gains of photodiodes PD1 and PD2 in Fig. 5.3, a high power being desirable in order to maximise the signal to noise ratio on these channels. Note that the power entering the fibre splitter tree from laser 2 was adjusted using a variable attenuator to be approximately equal to the 0.2 mW power level of laser 1. This was done by observing the amplitude of the interference signals from the two lasers whilst adjusting the variable attenuator. The purpose of equalising the laser powers entering the splitter tree is to equalise the signal to

noise ratio for each of the laser's signals from the interferometers.

### 5.3.2 Dynamic vs single laser FSI

The experimental evaluation reported in this section was done using Dynamic FSI to perform the iterative step, as explained in section 5.1.3. This was chosen over the single laser FSI alternative (which was explained in section 5.1.3) because it offered higher measurement precision. This is particularly true for an uncovered beam path, and for these measurements it was not practical to cover the path of interferometer 4, as this interferometer's length needed to be changed many times during a set of measurements.

Attempts were made to perform the experimental evaluation reported in this section using single laser FSI, but for this experimental setup at least, this method did not offer sufficient precision: It was found that the initial estimates of the interferometer integer phase offset, $\hat{N}_0^i$, varied by more than $\pm 0.5$ on subsequent measurements. Therefore the rounding step could not be expected to calculate the correct value for the integer phase offset, and the interative method would fail.

This casts doubt onto the suitability of single laser FSI as a method for performing the iterative step in Cascaded FSI. However, just because it did not offer the required precision when using the experimental setup described here does not mean that it cannot do so in other situations. For example, these measurements used a laser with a maximum tuning speed of 100 nm/s, but lasers are now commercially available with tuning speeds of 1000 nm/s and above. A higher tuning speed will decrease the measurement's susceptability to errors caused by a changing OPD during the measurement, and it is possible that using a faster tuning laser could improve the measurement precision enough for single laser FSI to be a viable method for the iterative step in Cascaded FSI.

### 5.3.3 Systematic errors

It shall be seen from the experimental data presented later (for example, in Fig. 5.9) that there were systematic errors on the initial estimates, $\hat{N}_0^i$, that remain the same from one measurement to the next. The underlying cause is not yet understood, and investigating this further would be a priority for future work. This section describes a method for coping with these systematic errors in a way that makes it possible to perform an experimental evaluation of the technique despite the presence of the errors.

As has been stated previously, the initial estimate, $\hat{N}_0^i$, should have an uncertainty less than $\pm 0.5$. This corresponds to a probability distribution for $\hat{N}_0^i$ similar to that shown in Fig. 5.4(a)(i). In this example there is no systematic error on $\hat{N}_0^i$, and the random variation is such that a negligible fraction of the initial estimates will lie outside the required $\pm 0.5$ of the true value, $N_0^i$. We may investigate the width of the distribution of errors on $\hat{N}_0^i$ experimentally by plotting the distribution, over multiple measurements, of the correction made when the initial estimate, $\hat{N}_0^i$, is rounded to the nearest integer to get the second estimate, $\hat{\hat{N}}_0^i$. This is the difference between the initial and second estimates, $\hat{N}_0^i - \hat{\hat{N}}_0^i$ (A plot of the distribution of $\hat{N}_0^i$ alone is not useful as the laser tuning repeatability is such that the value of $N_0^i$ will likely not be the same from one measurement to the next). Such a plot is shown, for this theoretical example, in Fig. 5.4(a)(ii). If we make the assumption that the distribution of errors, $\hat{N}_0^i - N_0^i$, is roughly Gaussian in form then the fact that the distribution in this figure goes to a negligibly small value at the extremes of the horizontal axis provides a good indication that the random uncertainty on $\hat{N}_0^i$ is below the required $\pm 0.5$.

The effect of a systematic error on $\hat{N}_0^i$ is illustrated in Fig. 5.4(b)(i), where the distribution of $\hat{N}_0^i$ is now centred on $N_0^i - \alpha^i$: There is a systematic error of $-\alpha^i$ on the initial estimates. This means that a significant proportion of initial estimates are now closer to $N_0^i - 1$ than $N_0^i$: The rounding step will round these to $N_0^i - 1$, and will therefore calculate the wrong value. This situation may be detected experimentally by plotting the distribution of $\hat{N}_0^i - \hat{\hat{N}}_0^i$ for a set of repeated measurements. An example of what may be seen in such a plot is shown

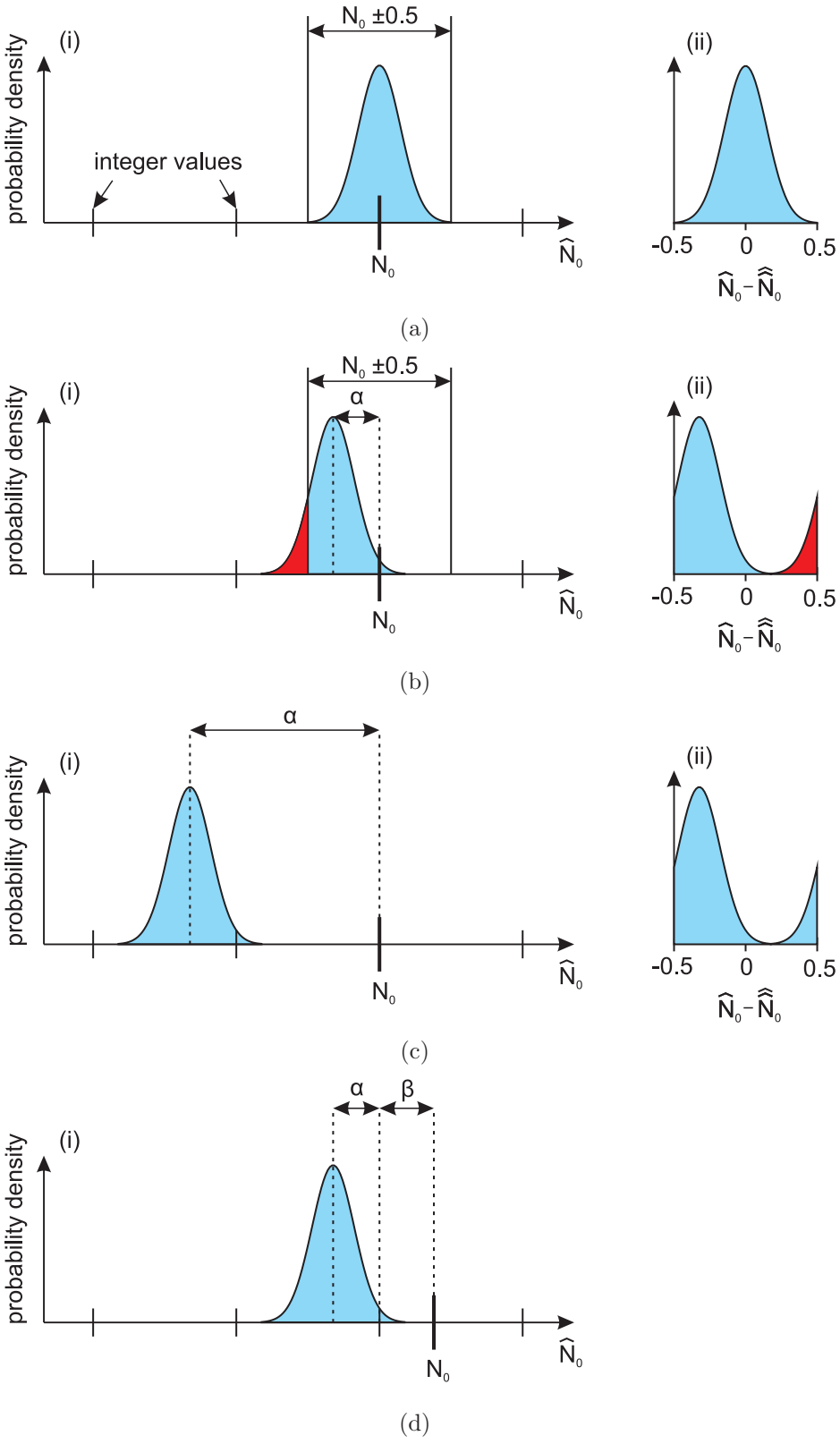


Figure 5.4: The rounding step in the presence of systematic errors

in Fig. 5.4(b)(ii). The initial estimates that lie in the darker, red shaded region to the right of this figure have been rounded, incorrectly, to $N_0^i - 1$.

We may attempt to correct for the systematic error by including a correction for it in the rounding step, redefining it as

$$\hat{\hat{N}}_0^i = ||\hat{N}_0^i + \alpha^i|| \, . \tag{5.3.1}$$

We may obtain a value for $\alpha^i$ by observing the shift away from zero on the peak of the distribution of $\hat{N}_0^i - \hat{\hat{N}}_0^i$. However, this only gives us an ambiguous estimate for $\alpha^i$: As Fig. 5.4(c) shows, if $\alpha^i$ differs by an integer value when compared to the example of Fig. 5.4(b) then exactly the same distribution of $\hat{N}_0^i - \hat{\hat{N}}_0^i$ is observed (in Fig. 5.4(c)(ii)). Therefore this method may only determine the fractional part of $\alpha^i$, leaving the integer part undetermined.

An additional complication is a slight, but important, departure from the model as used so far. We have previously assumed that $N_0^i$ are exact integer values. This is true for an ideal theoretical model, such as that presented in chapter 2, but a better agreement with the experimental results presented later in this section is achieved if we instead empirically model $(N_0^i - \beta^i)$ to be exact integer values, where $\beta^i$ is a constant associated with each interferometer.

One candidate for the cause of this discrepancy is the small but non-zero dispersion of air, which was not taken into account in the model of chapter 2. This causes the OPD of an interferometer to vary with laser wavelength. Further work is required to determine whether this is the true cause of the experimentally determined discrepancy: The following argument is presented merely as an example of a possible mechanism for the discrepancy from the ideal model that is seen in the experimental results.

We originally modelled $D$ as being independent of laser frequency. However, the dispersion of air will give $D$ a dependence upon laser frequency. This may be modelled by including a term proportional to laser frequency in the OPD, $D = D_0(1 + \zeta\nu)$, so that the

relationship between phase and laser frequency then becomes

$$\phi = D_0\nu/c + D_0\zeta\nu^2/c \; .$$

We only measure interferometric phase over a narrow range of frequencies (up to 10 THz) when compared to the absolute frequency of the laser (approximately 200 THz), so therefore the phase behaviour we observe may be well approximated with a Taylor expansion around a frequency in the centre of the laser tuning range, $\nu_0$,

$$\begin{aligned}\phi(\nu) &\simeq \phi(\nu_0) + \left.\frac{\partial\phi}{\partial\nu}\right|_{\nu_0}(\nu - \nu_0) \\ &= D_0(1 + 2\zeta\nu_0)\nu/c - D_0\zeta\nu_0^2/c \; .\end{aligned}$$

Next, the phase is written as the sum of its integer and fractional parts, as was done in section 2.2.3, and rearranged,

$$\begin{aligned}N_0 + u &= D_0(1 + 2\zeta\nu_0)\nu/c - D_0\zeta\nu_0^2/c \\ (N_0 + D_0\zeta\nu_0^2/c) + u &= D_0(1 + 2\zeta\nu_0)\nu/c \\ N_0' + u &= D'\nu/c \; .\end{aligned}$$

Where $N_0'$ and $D'$ are the apparent 'integer' phase offset and OPD, respectively, which differ from the earlier definition due to dispersion in the medium. Due to the $\zeta$ term, $N_0'$ is not guaranteed to be an exact integer.

The magnitude of this effect is estimated, taking the dispersion of air to be $dn/d\lambda = 8 \times 10^{-7}$ $\mu\text{m}^{-1}$, then $\zeta = 6 \times 10^{-23}$ $\text{Hz}^{-1}$. With an optical path difference $D_0 = 1$ m, and a laser frequency $\nu = 200$ THz, the correction factor is

$$D_0\zeta\nu_0^2/c = 8 \times 10^{-3} \; .$$

This is significantly smaller than 0.5 and therefore this effect alone is not enough to explain

the requirement to introduce a $\beta$ term. However, other frequency dependent effects may well have a larger impact. One such effect could be dispersion in the optics that collimate the beams for the interferometers. The collimators used for experiments in this thesis used a single lens in a pre-aligned package with the optical fibre end at the focal point of the lens. Dispersion in this lens will cause the geometry of the beam in the interferometer to vary as a function of wavelength. This could include changes in the focus of the beam and changes in the beam direction. This will cause the interferometer OPD to vary as a function of laser frequency, creating the same effect as was described above for the dispersion of air.

In the presence of an effect like this, the apparent value of $N_0^i$ may be as shown in Fig. 5.4(d). Here, instead of $N_0^i$ being an integer, $(N_0^i - \beta^i)$ is an integer. This may be taken account of by redefining the rounding step as

$$\hat{\hat{N}}_0^i = ||\hat{N}_0^i + \alpha^i|| + \beta^i \ , \tag{5.3.2}$$

where the $\alpha^i$ and $\beta^i$ terms together can both compensate for a systematic error and correct for $N_0$ having a 'shifted' integer value. However, we cannot determine the value of both $\alpha^i$ and $\beta^i$ from the peak in the distribution of $\hat{N}_0^i - \hat{\hat{N}}_0^i$. A method for determining $\alpha^i$ and $\beta^i$ non-ambiguously for one of the interferometers is described at the end of section 5.3.5.

The need to include the $\alpha^i$ and $\beta^i$ corrections is a significant complication, but, as shall be shown, this does not stop Cascaded FSI working altogether. This is clearly an area which requires further work, for which the key priority should be to clearly identify the cause of the discrepancy from the simpler model of chapter 2. There are two options for dealing with this issue: If the $\alpha^i$ and $\beta^i$ parameters are found to be stable over long time periods (such as months or years) then may be calibrated and corrected for. Alternatively it may prove possible to construct interferometers or analyse data in such a way as to make the correction terms negligible ($\alpha^i, \beta^i \ll 0.5$).

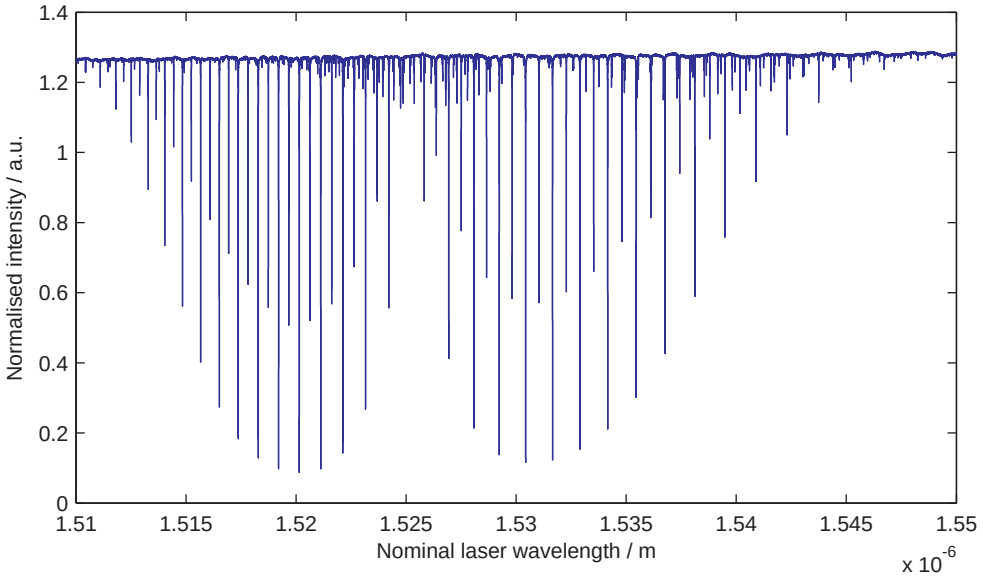


Figure 5.5: Acetylene absorption spectrum. The 'normalised intensity' is the ratio of voltages on photodiodes 1 and 2. This is higher than 1 in places because the split ratio of the beam-splitter is not exactly 50:50, and there are small differences in coupling efficiency and gain levels for photodiodes 1 and 2.

### 5.3.4 Bootstrapping using acetylene cell

The first part of a Cascaded FSI measurement is the bootstrapping step, which determines the integer phase offset of one of the bootstrap interferometer. This section contains an investigation of the frequency reference method of bootstrapping, which was described in section 5.1.2.

As the optical frequency of tuneable laser 2 is swept, the power transmitted through the acetylene cell is monitored with photodiode 1, as shown in Fig. 5.3. Photodiode 2 monitors the power of the laser. The transmittance of the acetylene cell is calculated as the ratio of the voltages from photodiodes 1 and 2. This reduces fluctuations in the measured transmittance due to laser intensity variations.

The transmittance calculated in this way during a portion of a laser frequency sweep is shown in Fig. 5.5. The multiple sharp dips in this data are the absorption peaks of the acetylene gas. The centre frequencies of 56 of these lines have been measured by NIST [31] for a 5 cm long cell filled with acetylene $^{12}C_2H_2$ to a pressure of 6.7 kPa (50 Torr). The gas cell used in this investigation was a Thorlabs CQ09050-CH12 gas cell, which is also 5cm

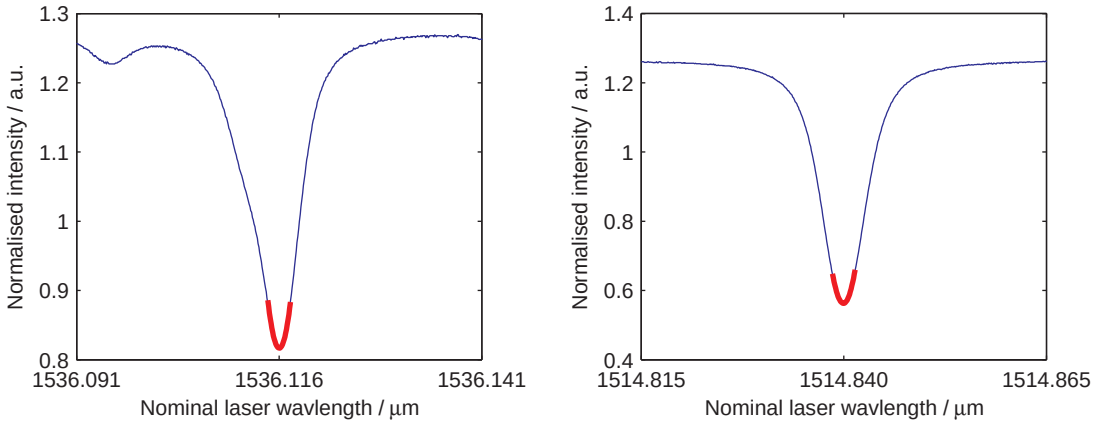


(a) peak P18 (b) peak R21

Figure 5.6: Examples of fits to acetylene absorption peaks. The labels P18 and R21 correspond to the labelling used in [31].

long, and filled with acetylene $^{12}C_2H_2$ to a pressure of 6.7 kPa (50 Torr).

By locating the centre of the 56 calibrated absorption peaks in our data we can determine points during the laser frequency scan when laser 2 has a known frequency, corresponding to the calibrated values. The centres were found by fitting a quadratic curve around the central region of the peaks. Examples of two such peak fits are shown in Fig. 5.6. The shape of an isolated absorption peak is theoretically a Voigt profile [31]. Figure 5.6(b) is a good example of such a profile. However, several of the absorption peaks do not have this shape, due to the presence of other nearby or overlapping absorption features, as may be seen in Fig. 5.6(a). For this reason, a quadratic fit of a small region around the centre of each absorption peak was chosen as a simple yet robust method of locating the centre of each peak. The second and penultimate peaks, labelled R28 and P28 in [31], are the smallest and were not fitted as reliably as the other peaks and for this reason, they are not used.

Fitting the peaks allows us to identify a set of ADC sampling indices, $m_n$, where the laser has a known absolute frequency. In general, the exact location of fitted peak centre will lie between sampling points. In this case interpolation between the neighboring points is used to generate an additional interpolated data point that lies at the exact location of the peak centre. Linear interpolation was used for these measurements.

With these interpolated data points calculated, corresponding $p_{m_n}$ values are calculated

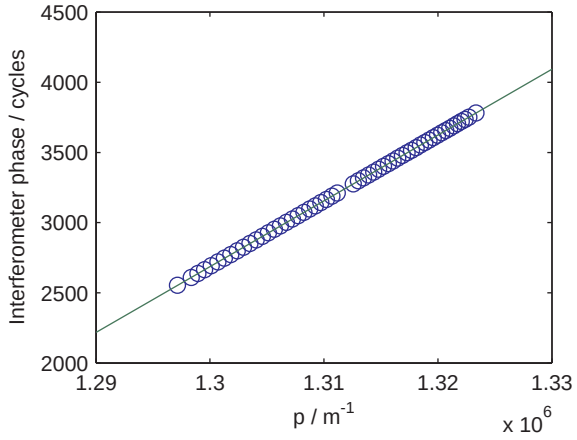


Figure 5.7: Linear fit to unwrapped phase vs $p$

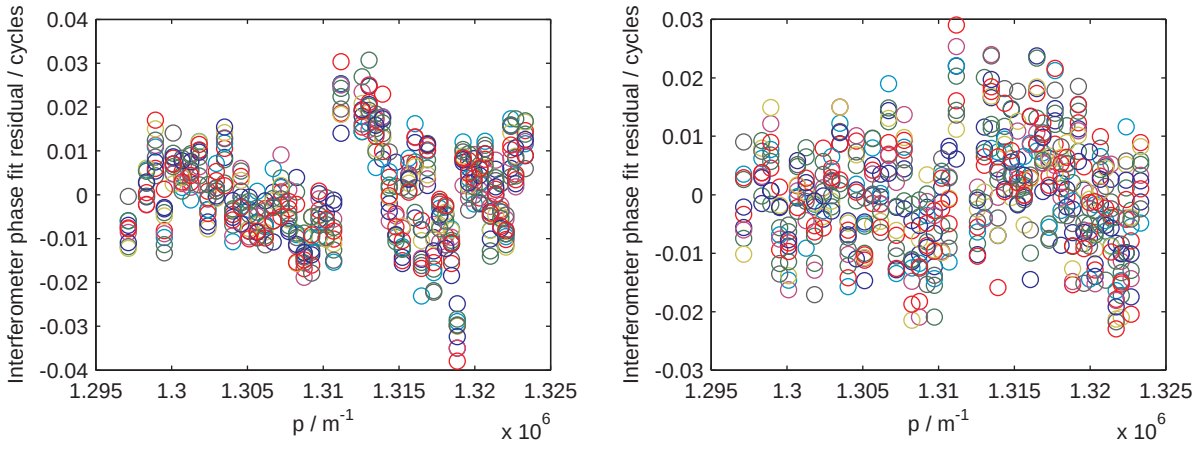


(a) interferometer 1 (b) interferometer 2

Figure 5.8: Residuals from straight line fit of unwrapped phase vs $p$

according to Eqn. (5.1.11). From Eqn. (5.1.12), these have a linear relationship with the unwrapped phases, $u_{m_n}$. The next analysis step is to fit a straight line to the pairs of values ($p_{m_n}$, $u_{m_n}$), to determine the integer phase offset of the bootstrap interferometer, $N_0^1$. An example of such a fit is shown in Fig. 5.7. In order to investigate the functioning of this bootstrap method, it is used to determine the integer phase offset of other interferometers as well as the bootstrap interferometer. Figure 5.8 shows the residuals of 10 fits to unwrapped phases from interferometer 1, and interferometer 2. In addition to the random variation of these residuals from measurement to measurement, it may be seen that there is a systematic component to the residuals in each figure. This could be due to systematic errors in the location of the absorption peak centres, or systematic errors in the calculated phase from each interferometer. It is currently unknown which, if either, is the dominant contribution. This is an issue that would benefit from further investigation.

The straight line fit returns two values: a gradient and an offset. The offset, multiplied by -1, is the first estimate of the integer phase offset, $\hat{N}_0^1$. A second estimate for the integer phase offset is calculated by rounding $\hat{N}_0^1$ to the nearest integer value, according to Eqn. 5.1.13. Figures 5.9, 5.10 and 5.11 show the difference between the initial, and rounded estimates, $(\hat{N}_0^i - \hat{\hat{N}}_0^i)$, for interferometers 1, 2, and 3 respectively. They are shown for 100 measurements, (a) as a time series, and (b) as a histogram. Ideally these should values should be distributed with a mean of zero and a standard deviation significantly less than $\pm 0.5$.

From the histograms it may be seen that the amount of *random* variation in these corrections is just below the required $\pm 0.5$ for interferometers 1 and 2. From this it is concluded that the random error on these estimates $\hat{N}_0^1$ and $\hat{N}_0^2$ is lower than $\pm 0.5$. However, for interferometer 1 there is clearly also a significant systematic shift of the corrections away from the desired mean value of zero. Using the alternative rounding step of Eqn. (5.3.2), and choosing $\alpha^1 = -0.5$, $\beta^1 = 0$, the size of the correction step for interferometer 1 (Fig. 5.9) is replotted in Fig. 5.12. In this figure it may be seen that the distribution of correction sizes goes to zero before $\pm 0.5$.

For interferometer 3, it is seen that the amount of random variation of the correction is

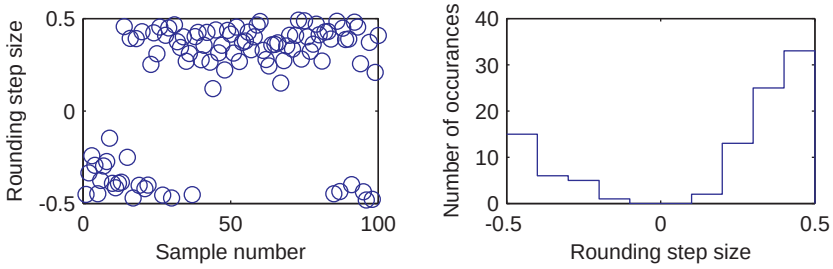


(a) (b)

Figure 5.9: Rounding step correction sizes for interferometer 1

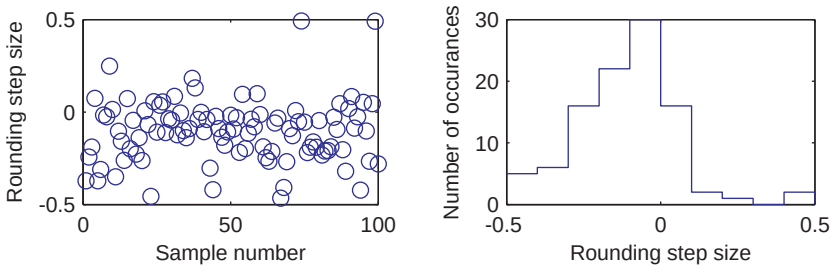


(a) (b)

Figure 5.10: Rounding step correction sizes for interferometer 2

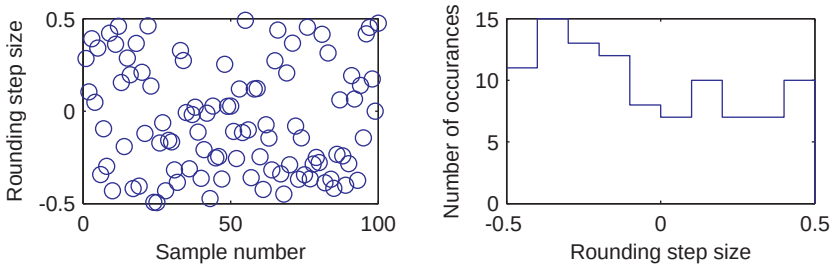


(a) (b)

Figure 5.11: Rounding step correction sizes for interferometer 3

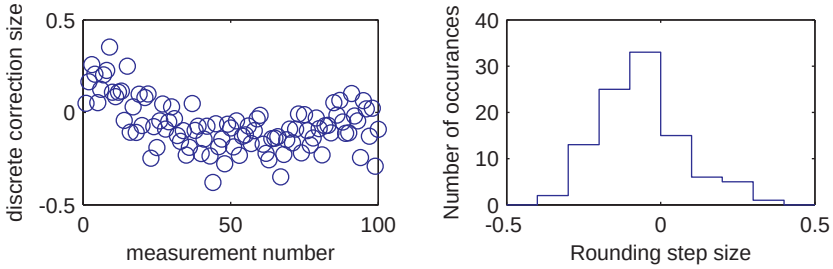


(a) (b)

Figure 5.12: Rounding step correction sizes for interferometer 1 with $\alpha^1 = -0.5$

greater than $\pm 0.5$, and hence the rounding step cannot be used here to improve the estimate $\hat{N}_0^3$. This is also the case for interferometer 4 (not plotted).

#### Bootstrapping for Dynamic FSI

For the iterative steps, described next, Dynamic FSI is used. This means that the bootstrapping calculation must determine not just $N_0^1$, but also $\bar{N}_0^1$. Recall that we chose to express these two values in terms of their sum and difference, $S^1$ and $\Delta^1$, according to the definitions of Eqns. (4.1.4).

This investigation calculated these using the 'beat detection' method from section 4.1.2 to determine $\Delta^1$. The improved, rounded estimate, $\hat{\hat{\Delta}}^1$ was used here. The acetylene cell method described above has determined a rounded estimate, $\hat{\hat{N}}_0^1$. These two values may be combined to calculate an estimate for $S^1$ as follows,

$$\hat{\hat{S}}^1 = \hat{\hat{\Delta}}^1 + 2\hat{\hat{N}}_0^1 \ . \tag{5.3.3}$$

We now have the two estimates, $\hat{\hat{S}}^1$ and $\hat{\hat{\Delta}}^1$, as required to initialise the iterative steps when using Dynamic FSI.

### 5.3.5 Iteration

Once the bootstrapping procedure has been done, the integer phase offset of all other interferometers in the system is calculated using an iterative process that is investigated in this section.

Dynamic FSI is used for this iterative procedure, but with a slight difference to the method as described in section 5.1.3. This experimental investigation was done with a two step process. The first step uses Dynamic FSI to determine the ratios of the integer offsets, $S^2/S^1$, $S^3/S^2$ and $S^4/S^3$. The second step uses these ratios in an iterative process to determine precise and absolute values of $S^i$ for all interferometers.

The reason for using this two step process was the amount of processing time required to calculate the ratios, which takes several tens of seconds per ratio calculation, relative to the amount of processing time required to go through the iterative process once the ratios have been calculated, which takes only a very small fraction of a second. It shall be seen that in the iterative process we shall need to make more corrections for systematic errors similar to the correction made for the bootstrapping step. This shall require recalculating the iterative steps multiple times, trying out different values for the correction factors. This would have been impractical if the ratios had been recalculated every time, due to the large amount of processing time required for this. Thankfully it has been possible to split the calculation into two steps, which allows many different values for the correction factors to be trialled in a reasonable length of time.

The calculations performed for this thesis were performed in Matlab, and the emphasis was on accuracy, making use of all the data available. As such, little effort has been spent on increasing the speed of these computations. It is envisaged that great increases in the speed of computation should be possible, and these may require only a small trade-off by way of a decrease in accuracy. There are two methods which could acheive this: Firstly, downsampling the data will increase computation speed, but should not decrease accuracy much as the original data was quite highly oversampled. Secondly, it is possible to treat the least squares Eqns. (4.1.8), (4.1.11) and (4.1.12) as linear least squares equations of the form $Ax = B$, if we ignore the fact that the $A$ matrix is composed of measured values, containing errors (whereas a true linear least squares problem should have an $A$ matrix that consists entirely of known values that are free from error). This would certainly lead to a faster solution, but some effort would be required to justify this approach and investigate what magnitude of error results.

### Determining S ratios

Dynamic FSI was used to determine the ratios of integer phase offsets for pairs of interferometers, $S^2/S^1$, $S^3/S^2$ and $S^4/S^3$. Dynamic FSI (as opposed to single laser FSI) was chosen

due to its improved precision when measuring an uncovered beam path (demonstrated in section 4.3.4). This made making large numbers of repeated measurements where the length of interferometer 4 was changed between measurements much more practical.

In order to describe the calculation of these ratios, consider determining the ratio $R^p$, defined as $R^p = S^{p+1}/S^p$. To calculate this ratio, we use the phases from the relevant pair of interferometers, $\tilde{u}_n^p$ and $\tilde{u}_n^{p+1}$, and estimates of $S^p$ and $\Delta^p$. These values are inserted into the 'cascaded' solution option least squares problem, Eqn. (4.1.12).

The value of $\Delta^p$ used was calculated using the beat detection method as described for the 'beat detection' solution option in section 4.1.2. The rounded estimator, $\hat{\bar{\Delta}}^p$, was used here.

To obtain a value for $S^p$, first a value for $\bar{N}_0^p$ was determined using the frequency reference bootstrapping method, as described above in section 5.3.4 (recall that this method may be used to obtain information about interferometers other than the bootstrap interferometer). For this calculation, the initial estimate, $\hat{\bar{N}}_0^p$, was used, as this estimate does not have sufficiently small uncertainty in every interferometer to make use of the rounding step. The estimate $\hat{S}^p$ was then calculated as

$$\hat{S}^p = \hat{\bar{\Delta}}^p + 2\hat{\bar{N}}_0^p \,. \tag{5.3.4}$$

Using these estimates, the 'cascaded' solution option of Eqn. (4.1.12) is solved using least squares problem to compute estimates for $\Delta^{p+1}$ and $S^{p+1}$. The ratio $S^{p+1}/S^p$ is then calculated, using the estimates that we now have for both values.

### Iteration using S ratios

Equipped with the $R^p$ values, we may calculate precise estimates for the absolute value of $S^p$ for all interferometers using the following iterative procedure:

The rounded estimate, $\hat{\bar{S}}^1$, is calculated using the acetylene cell method, including the

correction factor, $\alpha^1 = -0.5$. This is used to initialise the iterative procedure. From this, an estimate of $S^2$ is calculated as

$$\hat{S}^2 = R^1 \hat{\hat{S}}^1 \ . \tag{5.3.5}$$

This estimate is then rounded to the nearest integer,

$$\hat{\hat{S}}^2 = ||\hat{S}^2|| \ . \tag{5.3.6}$$

From this, we obtain a precise estimate for the integer phase offset of the second interferometer, $\hat{\hat{S}}^2$. The general case for these two steps may be written as,

$$\hat{S}^{p+1} = R^p \hat{\hat{S}}^p \ , \tag{5.3.7}$$

$$\hat{\hat{S}}^{p+1} = ||\hat{S}^{p+1}|| \ . \tag{5.3.8}$$

This process is iterated over, increasing the value of $p$ upon each iteration until rounded estimates for the integer phase offset of all interferometers have been calculated.

**Results of iterative step**

We may investigate if this step has sufficient precision, as was done for the bootstrapping step, by making repeated measurements and plotting the size of the rounding correction, $(\hat{S}^i - \hat{\hat{S}}^i)$. This is shown for the first iterative step in Fig. 5.13.

As was the case in Fig. (5.9), the mean of the distribution is not zero, indicating a systematic error in the calculation of $R^1$. However, the width of the distribution is very narrow, indicating that the precision is good enough.

Using the rounded values for $S^2$ calculated from this process, the next iteration is performed, with the size of the rounding correction here plotted in Fig. 5.14. As before, there is a systematic offset. Note that, even though there was a systematic error in the previous iteration, the distribution of corrections in this iteration is still narrow.

Using corrections as described in section 5.3.3 we can shift these distributions so that they

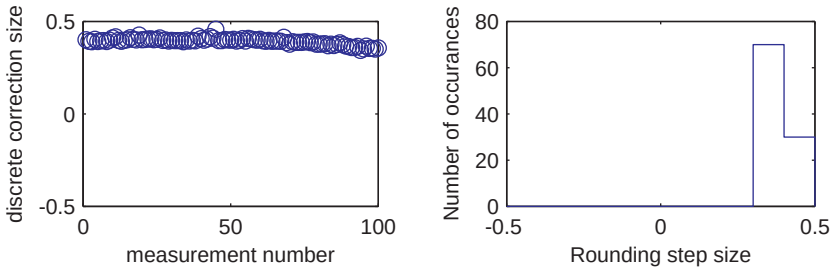


(a) (b)

Figure 5.13: Iterative step correction sizes for interferometer 2

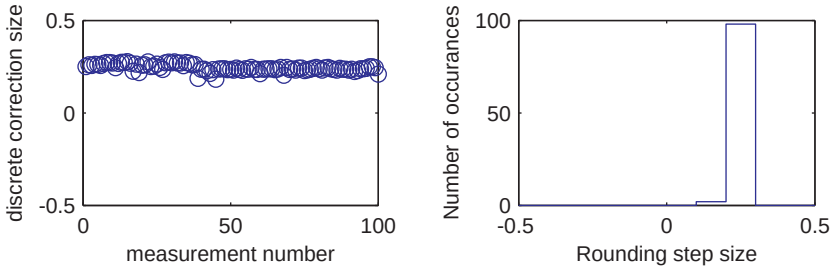


(a) (b)

Figure 5.14: Iterative step correction sizes for interferometer 3

are centred around zero. Remember, though, that the choice of values for these correction terms is ambiguous, so by introducing them, we decrease the chance of a discrete error, but do not necessarily improve the accuracy of the measurement.

With $\alpha^2 = -0.4$, $\beta^2 = 0$ and $\alpha^3 = -0.3$, $\beta^3 = 0$, the iterations are recalculated, and the sizes of the correction terms replotted in Figs. 5.15 and 5.16.

### Iterative step with different lengths

It is possible to investigate the accuracy of these measurements as well as the precision, by measuring a variety of different lengths as follows: As was described for the single laser FSI method of performing the iterative step, in section 5.1.3, the Cascaded iterative step can be thought of as a straight line fit of the known, absolute phase of the $p^{\text{th}}$ interferometer, $N_0^p + u_n^p$, to the unwrapped phase of the $(p+1)^{\text{th}}$ interferometer, $u_n^{p+1}$. The linear relationship

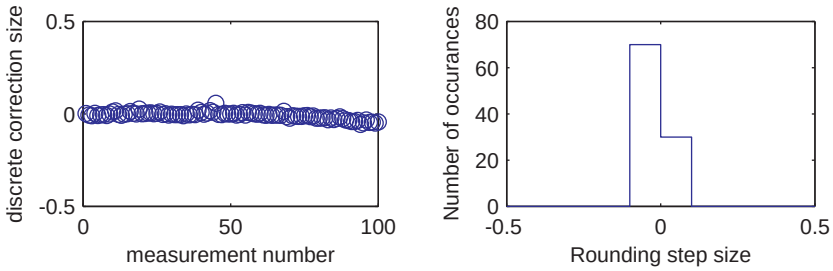


(a) (b)

Figure 5.15: Iterative step correction sizes for interferometer 2 with $\alpha^2 = -0.4$, $\beta^2 = 0$

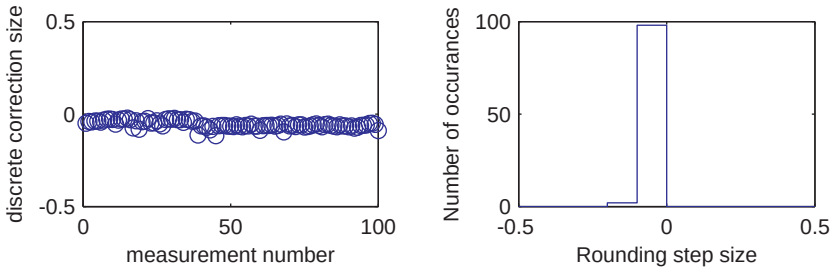


(a) (b)

Figure 5.16: Iterative step correction sizes for interferometer 3 with $\alpha^3 = -0.3$, $\beta^3 = 0$

between the two may be expressed in the form $y = mx + c$,

$$u_n^{p+1} = \frac{D^{p+1}}{D^p} u_n^p + \left( \frac{D^{p+1}}{D^p} N_0^p - N_0^{p+1} \right) ,$$

However, as was mentioned in section 5.3.3, we suspect that $N_0^p$, may not necessarily be an exact integer value, and that instead, $(N_0^p - \beta^p)$ is an integer. If we do not correct for $N_0^p$ being a non-integer value, then the relationship between the rounded estimate, $\hat{\hat{N}}_0^p$, and the true value, $N_0^p$ is

$$\hat{\hat{N}}_0^p = N_0^p + \beta^p ,$$

Substituting this into the iterative step of Eqn. (5.1.5), we obtain,

$$\begin{aligned} \hat{N}_0^{p+1} &= \Gamma \hat{\hat{N}}_0^p - \Omega \\ \hat{N}_0^{p+1} &= \Gamma \left( N_0^p + \beta^p \right) - \Omega \\ \hat{N}_0^{p+1} &= N_0^{p+1} + (D^{p+1}/D^p)\beta^p . \end{aligned}$$

This shows that if $N_0^p$ is not an integer value and we do not include a $\beta^p$ term to correct for it, there will be an error on $\hat{N}_0^{p+1}$ that is scaled by the ratio of interferometer OPDs, $D^{p+1}/D^p$. This will affect the rounded estimate as follows,

$$\begin{aligned}\hat{\hat{N}}_0^{p+1} &= ||\hat{N}_0^{p+1}|| \\ &= ||N_0^{p+1} + (D^{p+1}/D^p)\beta^p|| \\ &= ||N_0^{p+1} - \beta^{p+1} + \beta^{p+1} + (D^{p+1}/D^p)\beta^p|| \\ &= N_0^{p+1} - \beta^{p+1} + ||\beta^{p+1} + (D^{p+1}/D^p)\beta^p|| \,.\end{aligned}$$

The difference between the initial and rounded estimates is then

$$\hat{N}_0^{p+1} - \hat{\hat{N}}_0^{p+1} = (D^{p+1}/D^p)\beta^p + \beta^{p+1} - ||(D^{p+1}/D^p)\beta^p + \beta^{p+1}|| \,. \tag{5.3.9}$$

This gives us a way of unambiguously determining $\beta^p$: We make multiple measurements with interferometer 4 having different lengths in each measurement, and then plot the size of the rounding correction vs OPD of interferometer 4. According to Eqn. (5.3.9), a non-zero value of $\beta^3$ should show up as a gradient in the line of rounding correction vs interferometer 4 OPD.

Measurements were made with interferometer 4 having different OPDs in different measurements. The size of the rounding correction is plotted vs OPD for interferometer 4 in Fig. 5.17. As predicted above, there is a linear relationship between OPD and correction size. Correction size is an ambiguous quantity, being determined in the range $[-0.5, 0.5)$ and the final point of the upper right of this figure has been wrapped round.

This final point is manually unwrapped by subtracting 1 from it, and a linear fit is made to this data, shown in Fig. 5.18. The gradient of this line is $\beta^3$. Using this value to correct the final stage in the iterative process, the correction size is recalculated for interferometer 4, shown in Fig. 5.19.

An additional check was made to ensure that there is only one value of $\beta^3$ that would give

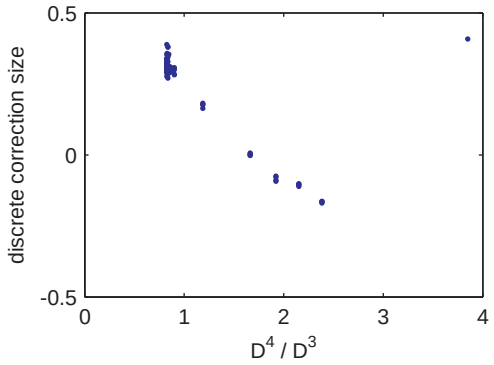


Figure 5.17: Rounding step discrepancy vs distance

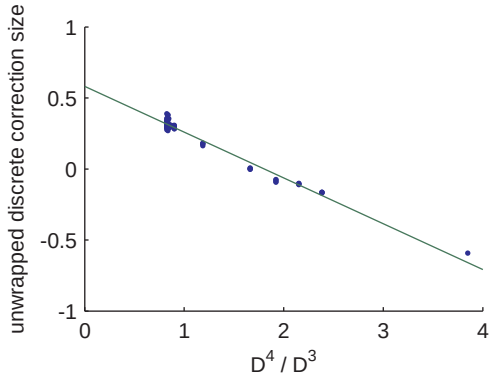


Figure 5.18: Linear fit to rounding step discrepancy vs distance

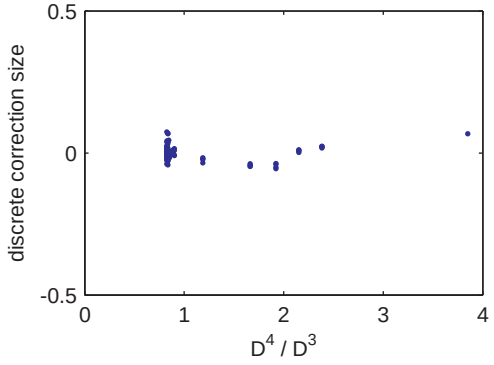


Figure 5.19: Rounding step discrepancy vs distance after correction

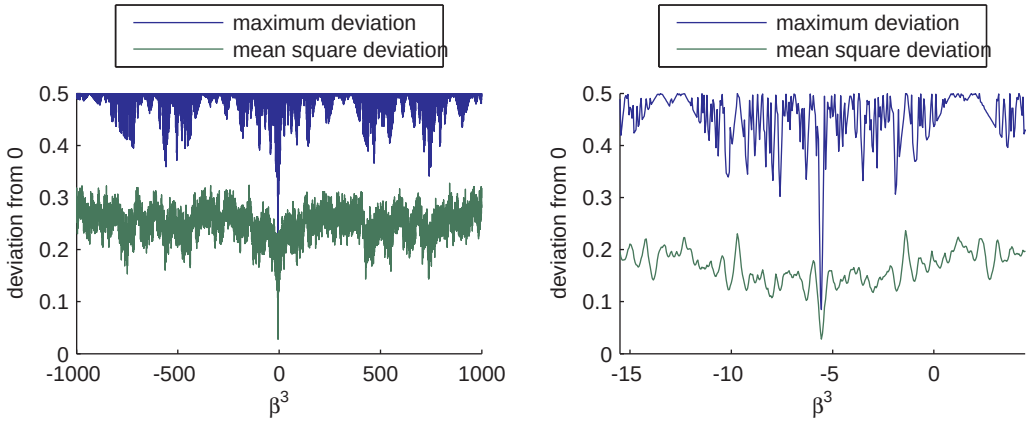


Figure 5.20: Rounding step discrepancy vs correction size

a reasonable correction. The distribution of correction values $(\hat{N}_0^4 - \hat{\hat{N}}_0^4)$ was evaluated as a function of $\beta^3$, with the result shown in Fig. 5.20. As can be seen, there is only one significant dip in these curves, showing that the value of $\beta^3$ that will give a reasonable correction is not ambiguous.

## 5.4 Summary

In section 5.1, a measurement method is proposed that has the ability to measure absolute distance with the precision and accuracy of displacement interferometry. Its precision is obtained by it being able to exactly determine the integer phase offset of an interferometer, such that distance measurement error is directly linked to phase measurement error. Its accuracy is obtained by measuring length relative to a stable wavelength reference. The uncertainty of measurements made with this method is investigated theoretically in section 5.2.

An experimental demonstration of the method is described in section 5.3. Although this showed the presence of systematic errors in the iterative part of the method, that required correcting by hand, it was still possible to verify that the method works as intended with measurements of multiple different distances remaining internally consistent.

# Chapter 6

# Summary

## 6.1 Summary of the methods

This thesis proposes two new methods for absolute distance measurement using frequency swept lasers, Dynamic FSI and Cascaded FSI, which each offer several advantages over previous FSI methods.

Dynamic FSI can measure a changing distance throughout a laser frequency sweep, and is therefore capable of a much higher measurement rate than other FSI implementations. As with other dual-laser FSI methods, it does not suffer from the problem of drift error. Dynamic FSI was successfully experimentally demonstrated, being able to measure a changing distances during the laser frequency sweep as claimed. Under measurement conditions containing random OPD fluctuations due to air turbulence, Dynamic FSI was shown to have a higher measurement precision than single laser FSI. There were, however, unexplained systematic discrepancies between the single laser FSI and Dynamic FSI measurements in this experiment. This would be a worthwhile area for further investigation.

Cascaded FSI can measure with high precision by calculating the exact value of the integer phase offset for the measurement interferometer. It also has the potential to measure with high accuracy, due to its ability to measure distance with respect to a stable wavelength

reference. This method was demonstrated experimentally, however this demonstration was hampered by the presence of unexplained systematic errors. An initial investigation of the cause of these was undertaken, where it was suggested that the dispersion of air could be a potential cause. Despite the systematic errors, it was possible to experimentally demonstrate the underlying principle behind Cascaded FSI, which is the iterative method of determining interferometer integer phase offsets.

## 6.2 Points for further investigation

The most pressing point for further investigation is the presence of systematic errors that have been encountered in both Dynamic FSI and Cascaded FSI. In Dynamic FSI, these occurred as a discrepancy between the measured distance as calculated by Dynamic FSI, and as calculated by single laser FSI. In Cascaded FSI these were apparent in the rounding step.

Both techniques, and especially Cascaded FSI, provide a very good basis for investigating these kinds of errors. An investigation of these errors using Cascaded FSI would not merely be beneficial to that method, but the lessons learned should be relevant to other forms of absolute distance interferometry using swept frequency lasers. As the dispersion of air in the measurement path has been identified as a potential cause of these errors, a theoretical investigation of the effect of this may be a promising starting point for future work on this topic.

The limits of the Taylor expansion approximation made in the 'time delay model' of section 2.1.2 is also worth further investigation. Recall that obtaining the simplified expression for interferometric phase, Eqn. 2.1.5, required dropping a term, $\pi(\partial\nu(t')/\partial t')\tau^2$, which has a magnitude proportional to the laser tuning speed, and the square of the interferometer OPD. Therefore, the approximation becomes less valid for measurements made with faster tuning lasers, or over longer distances. Lasers with tuning speeds of 1000 nm/s are now commercially available, and new kinds of laser, such as frequency shifted feedback lasers [51],

are being developed that have inherently faster tuning rates. Such an investigation would also be relevant for any space based applications that may require measurement over particularly large distances. Any such investigation would undoubtedly result in a model with a more complicated relationship between phase, laser frequency, and interferometer OPD. This may merely be a required extra complication to take account of, but it is possible that this different relationship could be exploited to enable a better measurement to be made.

# Appendix A

# Nomenclature

There are a large number of names that have been used to refer to methods for absolute distance measurement using a frequency swept laser. Those that I am aware of are summarised in Table A.1.

| | |
|---|---|
| FSI | Frequency Scanning [20] / Sweeping [4] Interferometry |
| WSI | Wavelength Scanning [65] / Shifting [24] / Sweeping [58] Interferometry |
| FMCW | Frequency Modulated Continuous Wave [53] |
| OFDR | Optical Frequency Domain Reflectometry [33] |
| VSW | Variable Synthetic Wavelength [7] |

Table A.1: Summary of names and their acronyms that have been used to describe absolute distance measurements with a frequency swept laser.

OFDR has been used to describe both 'coherent OFDR', which varies the optical frequency of the laser as in FSI, and 'incoherent OFDR' which is not an interferometric method and instead modulates the intensity of the beam in order to time reflections from a target.

FSI has also been referred to as Absolute Distance Interferometry (ADI) [61], although this is commonly used as a more generic term.

# Appendix B

# Hilbert transform signal requirements

I stated in section 2.2.2 that if it is possible to high pass filter the FSI signal in the desired way, then the conditions required for the Hilbert transform property of Eqn. (2.2.4) to hold are automatically satisfied. In this section I show that this is the case.

High pass filtering the signal requires that there exists some $\omega_s$ such that

$$\mathcal{F}[a(t)] = 0 \text{ for } |\omega| > \omega_s \tag{B.0.1a}$$

$$\mathcal{F}[b(t)\cos\phi(t)] = 0 \text{ for } |\omega| < \omega_s \tag{B.0.1b}$$

Eqn. (2.2.4) is derived using Bedrosian's product theorem for Hilbert transforms [8]:

**Theorem 1** (Part of Bedrosian's product theorem)**.** *Let $f(t)$ and $g(t)$ denote generally complex functions of the real variable $t$. If these functions can be separated in the frequency domain by a frequency $\omega_r$, such that*

$$\mathcal{F}[f(t)] = 0 \text{ for } |\omega| > \omega_r$$

$$\mathcal{F}[g(t)] = 0 \text{ for } |\omega| < \omega_r,$$

*then the Hilbert transform of their product is given by*

$$\mathcal{H}[f(t)g(t)] = f(t)\mathcal{H}[g(t)].$$

Thus in order for Eqn. (2.2.4) to be valid we require there to be an $\omega_r$ such that

$$\mathcal{F}[b(t)] = 0 \text{ for } |\omega| > \omega_r \tag{B.0.2a}$$

$$\mathcal{F}[\cos\phi(t)] = 0 \text{ for } |\omega| < \omega_r, \tag{B.0.2b}$$

I will now show that satisfying condition (B.0.1) guarantees that condition (B.0.2) is also satisfied.

Let $\omega_a$, $\omega_b$ and $\omega_c$ be positive constants such that the spectra of $a(t)$, $b(t)$ and $\cos\phi(t)$ are limited in the following ways:

$$\mathcal{F}[a(t)] = 0 \text{ for } |\omega| > \omega_a$$

$$\mathcal{F}[b(t)] = 0 \text{ for } |\omega| > \omega_b$$

$$\mathcal{F}[\cos\phi(t)] = 0 \text{ for } |\omega| < \omega_c,$$

where $\omega_a$, $\omega_b$ are chosen to have the minimal possible value, and $\omega_c$ is chosen to have the maximal possible value that satisfies the above condition.

Considering the Fourier transform convolution theorem ($\mathcal{F}(pq) = \mathcal{F}(p) \otimes \mathcal{F}(q)$) we see that the spectrum of $b(t)\cos\phi(t)$ is limited as follows:

$$\mathcal{F}[b(t)\cos\phi(t)] = 0 \text{ for } |\omega| < \omega_c - 2\omega_b.$$

Therefore, to satisfy condition (B.0.1), we require

$$\omega_a < \omega_c - 2\omega_b. \tag{B.0.3}$$

However, as $\omega_a$ is at least zero, then for condition (B.0.3) to be satisfied requires $2\omega_b < \omega_c$, regardless of the value of $\omega_a$. Given this, $\omega_r$ can be chosen anywhere in the range $(2\omega_b, \omega_c)$ and this will satisfy (B.0.2).

# Appendix C

# The method of least squares

## C.1 Least squares estimator

This section describes a method for computing what is in some sense a 'best' estimate of the remaining unknown integer phase offsets for the three Dynamic FSI solution option Eqns. (4.1.9), (4.1.11) and (4.1.12). The mathematical results in this section are based upon [64].

### C.1.1 Non-linear least squares

Least squares is a formalism for computing an estimate for a set of unknown values contained within a vector, $\boldsymbol{x}$, when there is a known relationship between these unknowns and some directly observable values, also contained within a vector, $\boldsymbol{l}$. In Dynamic FSI, the unknown values are some combination of $S^1$, $S^2$, $\Delta^1$ and $\Delta^2$, whereas the observable values are the unwrapped phases, $u_n^i$, together with the remaining $S^1$, $S^2$, $\Delta^1$ and $\Delta^2$ that aren't unknowns.

This relationship is defined with a set of equations, each one expressing a relationship between some elements of $\boldsymbol{x}$ and some elements of $\boldsymbol{l}$. The entire set of equations may be

expressed as a vector function, $\boldsymbol{f}$, such that

$$\boldsymbol{f}(\boldsymbol{x}, \boldsymbol{l}) = 0. \tag{C.1.1}$$

For Dynamic FSI, the relationship between $\boldsymbol{x}$ and $\boldsymbol{l}$ is defined by Eqns. (4.1.9), (4.1.11) and (4.1.12). Each of these equations may be put into the above form by subtracting the right hand side.

If we could measure without errors and our model was a perfect description of reality, then we should like to find some $\boldsymbol{x}$ that satisfies Eqn. (C.1.1) exactly. Doing this will give us the exactly correct values for the unknowns, $\boldsymbol{x}$ (If there is a unique $\boldsymbol{x}$ that satisfies Eqn. (C.1.1)). However, in reality, due to measurement error and imperfections in the model, there will not in general exist an $\boldsymbol{x}$ that satisfies Eqn. (C.1.1) exactly if we set $\boldsymbol{l}$ to be equal to the measured values of the observables. For this reason the observables are separated into two components; the measured values, $\boldsymbol{y}$, plus a *residual vector*, $\boldsymbol{\epsilon}$, such that $\boldsymbol{l} = \boldsymbol{y}+\boldsymbol{\epsilon}$. Given a set of measured values, $\boldsymbol{y}$, it will now be possible to find pairs ($\boldsymbol{\epsilon}$, $\boldsymbol{x}$), that *do* satisfy Eqn. (C.1.1) exactly.

### C.1.2 Maximum likelihood

However, there is not a unique choice of values ($\boldsymbol{\epsilon}$, $\boldsymbol{x}$) that satisfies Eqn. (C.1.1): We need to find a way of identifying the 'best' choice. If we trust our model and our measurements, then intuitively it seems sensible to try to keep the elements of the residual vector, which is our estimate of the measurement errors, as small as possible. There is a statistical justification for this intuition: Under the assumption of unbiased, Gaussian distributed errors on the measurements, it may be shown that an estimate, ($\boldsymbol{\epsilon}$, $\boldsymbol{x}$), that minimises a weighted sum of the residuals given by Trace($\boldsymbol{\epsilon}^T P \boldsymbol{\epsilon}$) corresponds to the most likely values of the unknowns, given some measured values, $\boldsymbol{y}$. (The matrix $P$ shall be defined shortly). This kind of estimate is known as a *maximum likelihood* estimator.

I will now show this for the simpler, but less general case, where the measurement errors are independent from each other. The joint probability density of obtaining a set of errors,

$\boldsymbol{\epsilon}$, where these errors are unbiased and Gaussian distributed, is

$$dP = \prod_{i=1}^{n} \frac{1}{\sqrt{2\pi\sigma_i^2}} \exp\left(-\frac{\boldsymbol{\epsilon}_i^2}{2\sigma_i^2}\right), \tag{C.1.2}$$

A least squares estimator finds values ($\boldsymbol{\epsilon}$, $\boldsymbol{x}$) that maximise the above probability density, whilst remaining consistent with the model equation, Eqn. (C.1.1). Maximising the probability density is equivalent to maximising the logarithm of the probability density, which is

$$\log(dP) = n\frac{1}{\sqrt{2\pi\sigma^2}} - \frac{1}{2}\sum_{i=1}^{n}\left(\frac{\boldsymbol{\epsilon}_i^2}{\sigma_i^2}\right). \tag{C.1.3}$$

Maximising the above is equivalent to minimising the sum;

$$\sum_{i=1}^{n}\left(\frac{\boldsymbol{\epsilon}_i^2}{\sigma_i^2}\right). \tag{C.1.4}$$

This sum may be written as Trace($\boldsymbol{\epsilon}^T P \boldsymbol{\epsilon}$), where $P$ is a diagonal *weight matrix* with $P_{ii} = 1/\sigma_i^2$.

### C.1.3 Bias

It should be noted that the estimator used here is not guaranteed to be an unbiased estimator. That is to say that the expectation value of the estimator is not necessarily equal to the true value. All three of the Dynamic FSI model equations considered here are non-linear models, and it is commonly accepted that maximum likelihood estimators are in general biased for non-linear models [14].

### C.1.4 Linearisation

In general it is not straightforward to find a closed form solution for the maximum likelihood estimator. In this case, it is common to use an iterative solution that refines an initial estimate based upon a local, linear approximation of the model of Eqn. (C.1.1), constructed

by Taylor expanding the function $\boldsymbol{f}(\boldsymbol{x},\boldsymbol{l})$ around the point ($\boldsymbol{x}=\boldsymbol{x}^0$, $\boldsymbol{\epsilon}=0$),

$$\begin{aligned}\boldsymbol{f}(\boldsymbol{x},\boldsymbol{l}) &\simeq \underbrace{\boldsymbol{f}(\boldsymbol{x}^0,\boldsymbol{y})}_{W}+\underbrace{\left.\frac{\partial \boldsymbol{f}}{\partial \boldsymbol{x}}\right|_{\boldsymbol{x}^0,\boldsymbol{y}}}_{A}\boldsymbol{\delta x}+\underbrace{\left.\frac{\partial \boldsymbol{f}}{\partial \boldsymbol{l}}\right|_{\boldsymbol{x}^0,\boldsymbol{y}}}_{B}\boldsymbol{\epsilon}\\ &= W+A\boldsymbol{\delta x}+B\boldsymbol{\epsilon}\ , \end{aligned} \tag{C.1.5}$$

where $\boldsymbol{\delta x}=\boldsymbol{x}-\boldsymbol{x}^0$.

The operation where a vector function is differentiated with respect to a vector argument is defined as follows,

$$\frac{\partial \boldsymbol{f}(\boldsymbol{x})}{\partial \boldsymbol{x}}=\begin{pmatrix} \frac{\partial \boldsymbol{f}_1(\boldsymbol{x})}{\partial \boldsymbol{x}_1} & \frac{\partial \boldsymbol{f}_1(\boldsymbol{x})}{\partial \boldsymbol{x}_2} & \cdots \\ \frac{\partial \boldsymbol{f}_2(\boldsymbol{x})}{\partial \boldsymbol{x}_1} & \frac{\partial \boldsymbol{f}_2(\boldsymbol{x})}{\partial \boldsymbol{x}_2} & \\ \vdots & & \ddots \end{pmatrix}\ .$$

For the case of Dynamic FSI, Eqns. (4.1.9), (4.1.11) and (4.1.12) can all be expressed in the following form,

$$\boldsymbol{f}(\boldsymbol{x},\boldsymbol{l})=\alpha(\boldsymbol{l})\boldsymbol{x}-\beta(\boldsymbol{l})=0\ . \tag{C.1.6}$$

Consider as an example, Eqn. (4.1.9), which may be written in the following form,

$$\begin{pmatrix} \hat{\hat{\Delta}}^2+u_0^2-\bar{u}_0^2 & -\hat{\hat{\Delta}}^1-u_0^1+\bar{u}_0^1 \\ \hat{\hat{\Delta}}^2+u_1^2-\bar{u}_1^2 & -\hat{\hat{\Delta}}^1-u_1^1+\bar{u}_1^1 \\ \vdots & \vdots \\ \hat{\hat{\Delta}}^2+u_{K-1}^2-\bar{u}_{K-1}^2 & -\hat{\hat{\Delta}}^1-u_{K-1}^1+\bar{u}_{K-1}^1 \end{pmatrix}\begin{pmatrix} S^1 \\ S^2 \end{pmatrix}-$$
$$\begin{pmatrix} \hat{\hat{\Delta}}^1(u_0^2+\bar{u}_0^2)-\hat{\hat{\Delta}}^2(u_0^1+\bar{u}_0^1)+2u_0^1\bar{u}_0^2-2\bar{u}_0^1u_0^2 \\ \hat{\hat{\Delta}}^1(u_1^2+\bar{u}_1^2)-\hat{\hat{\Delta}}^2(u_1^1+\bar{u}_1^1)+2u_1^1\bar{u}_1^2-2\bar{u}_1^1u_1^2 \\ \vdots \\ \hat{\hat{\Delta}}^1(u_{K-1}^2+\bar{u}_{K-1}^2)-\hat{\hat{\Delta}}^2(u_{K-1}^1+\bar{u}_{K-1}^1)+2u_{K-1}^1\bar{u}_{K-1}^2-2\bar{u}_{K-1}^1u_{K-1}^2 \end{pmatrix}=0\ .$$

So, in this case,

$$\alpha(\boldsymbol{l}) = \begin{pmatrix} \hat{\bar{\Delta}}^2 + u_0^2 - \bar{u}_0^2 & -\hat{\bar{\Delta}}^1 - u_0^1 + \bar{u}_0^1 \\ \hat{\bar{\Delta}}^2 + u_1^2 - \bar{u}_1^2 & -\hat{\bar{\Delta}}^1 - u_1^1 + \bar{u}_1^1 \\ \vdots & \vdots \\ \hat{\bar{\Delta}}^2 + u_{K-1}^2 - \bar{u}_{K-1}^2 & -\hat{\bar{\Delta}}^1 - u_{K-1}^1 + \bar{u}_{K-1}^1 \end{pmatrix}$$

$$\beta(\boldsymbol{l}) = \begin{pmatrix} \hat{\bar{\Delta}}^1(u_0^2 + \bar{u}_0^2) - \hat{\bar{\Delta}}^2(u_0^1 + \bar{u}_0^1) + 2u_0^1\bar{u}_0^2 - 2\bar{u}_0^1u_0^2 \\ \hat{\bar{\Delta}}^1(u_1^2 + \bar{u}_1^2) - \hat{\bar{\Delta}}^2(u_1^1 + \bar{u}_1^1) + 2u_1^1\bar{u}_1^2 - 2\bar{u}_1^1u_1^2 \\ \vdots \\ \hat{\bar{\Delta}}^1(u_{K-1}^2 + \bar{u}_{K-1}^2) - \hat{\bar{\Delta}}^2(u_{K-1}^1 + \bar{u}_{K-1}^1) + 2u_{K-1}^1\bar{u}_{K-1}^2 - 2\bar{u}_{K-1}^1u_{K-1}^2 \end{pmatrix}$$

Linearising this, the matrices $A$ and $B$ corresponding to the linearised form of Eqn.(C.1.5) are

$$\begin{aligned} A &= \left.\frac{\partial \boldsymbol{f}}{\partial \boldsymbol{x}}\right|_{\boldsymbol{x}^0,\boldsymbol{y}} \\ &= \alpha(\boldsymbol{y}), \end{aligned}$$

$$\begin{aligned} B &= \left.\frac{\partial \boldsymbol{f}}{\partial \boldsymbol{l}}\right|_{\boldsymbol{x}^0,\boldsymbol{y}} \\ &= \sum_i \boldsymbol{x}_i^0 \left.\frac{\partial \alpha_{(:,i)}}{\partial \boldsymbol{l}}\right|_{\boldsymbol{y}} - \left.\frac{\partial \beta}{\partial \boldsymbol{l}}\right|_{\boldsymbol{y}}, \end{aligned}$$

where the notation $\boldsymbol{x}_i^0$ indicates the $i^{\text{th}}$ element of the vector $\boldsymbol{x}^0$, and $\alpha_{(:,i)}$ indicates the $i^{\text{th}}$ column of the matrix $\alpha$. Note that, for this case of Dynamic FSI, the matrix $\alpha$ has the useful property that it is independent of the current estimate, $\boldsymbol{x}^0$. This means that it only needs to be calculated once in the iterative procedure.

In the example of Eqn. (4.1.9), the elements of $\boldsymbol{y}$ are arranged as,

$$\boldsymbol{y} = \left[u_0^1, \bar{u}_0^1, u_0^2, \bar{u}_0^2, u_1^1, \bar{u}_1^1, u_1^2, \bar{u}_1^2 ...\right]^T$$

and the partial derivatives of $\alpha$ and $\beta$ are,

$$\left.\frac{\partial \alpha_{(:,1)}}{\partial \boldsymbol{l}}\right|_{\boldsymbol{y}} = \begin{pmatrix} 0 & 0 & 1 & -1 & & & & & \\ & & & & 0 & 0 & 1 & -1 & \\ & & & & & & & & \ddots \end{pmatrix}$$

$$\left.\frac{\partial \alpha_{(:,2)}}{\partial \boldsymbol{l}}\right|_{\boldsymbol{y}} = \begin{pmatrix} -1 & 1 & 0 & 0 & & & & & \\ & & & & -1 & 1 & 0 & 0 & \\ & & & & & & & & \ddots \end{pmatrix}$$

$$\left.\frac{\partial \beta}{\partial \boldsymbol{l}}\right|_{\boldsymbol{y}} = \begin{pmatrix} -\Delta^2 + 2\bar{u}_0^2 & -\Delta^2 - 2u_0^2 & \Delta^1 - 2\bar{u}_0^1 & \Delta^1 + 2u_0^1 & & \\ & & & & & \ddots \end{pmatrix}$$

Using the linearised model, an improvement to the current estimate may be computed to be

$$\hat{\boldsymbol{x}} = \boldsymbol{x}^0 + \hat{\boldsymbol{\delta x}} \tag{C.1.7}$$

where $\hat{\boldsymbol{\delta x}}$ is

$$\hat{\boldsymbol{\delta x}} = -\left(A^T \left(BP^{-1}B^T\right)^{-1} A\right)^{-1} A^T \left(BP^{-1}B^T\right)^{-1} W. \tag{C.1.8}$$

This method is iterated by computing a new linearised model (i.e. a new set of $A$, $B$, and $W$ matrices) by Taylor expanding around the new estimate, $\hat{\boldsymbol{x}}$, and then computing a new best estimate by solving Eqn. (C.1.8) again. This procedure is iterated over until some stop condition is reached such as the correction being below some limit or a maximum number of iterations being reached.

## C.2 Least squares uncertainty

It is possible to calculate an unbiased estimate of the covariance matrix of $\hat{\boldsymbol{x}}$, given the covariance matrix of the observations, $\boldsymbol{y}$. This may be shown to be:

$$\Sigma_{\hat{\boldsymbol{x}}} = \left(A^T (BP^{-1}B^T)^{-1} A\right)^{-1} \tag{C.2.1}$$

The covariance matrix gives information about the distribution of errors in terms of the uncertainty on each element of $\hat{\boldsymbol{x}}$, and their correlation. With this information, and the assumption of Gaussian distributed errors, the joint probability distribution $f(\boldsymbol{x}_1, \boldsymbol{x}_2)$ may be calculated, where $f(x_1, x_2)$ is the probability density of a particular measurement calculating $\hat{x} = [x_1, x_2]^T$. If one were to draw contours of equal probability density, these would take the form of ellipses, with the size and orientation of the ellipse given by the elements of the covariance matrix.

It will be convenient to express the size and orientation of the error ellipse in a different way than that used in the covariance matrix. An alternative way of parameterising this is in terms of the following quantities:

- direction of the major axis of the ellipse
- size of the error ellipse along the major axis
- size of the error ellipse along the minor axis

This alternative way of describing the error ellipse may be calculated using an eigenvalue decomposition of the covariance matrix (or, very similarly, an eigenvalue decomposition of the design matrix, as the eigenvalue decomposition of a matrix and its inverse are very similar).

A matrix, $\Sigma$, may be factorised thus: $\Sigma = QVQ^T$. Where Q is a matrix containing the eigenvectors of A, and V is a matrix containing the eigenvalues of $\Sigma$ along its diagonal.

Upon performing an eigenvalue decomposition of the covariance matrix, the eigenvectors will point along the major and minor axes of the error ellipse and the eigenvalues will be the variance of the estimator $\hat{\boldsymbol{x}}$ along the direction given by the corresponding eigenvectors. This is all the information required to parametrise the error ellipse in the alternative way described above.

# Bibliography


[1] "In Orbit Formation Flying Experiment for PROBA 2: Feasibility Study". Technical report, ESA, 2004.

[2] Ahn T J and Kim D Y. "Analysis of nonlinear frequency sweep in high-speed tunable laser sources using a self-homodyne measurement and Hilbert transformation." *Applied optics*, 46(13):2394–400, 2007. ISSN 0003-6935.

[3] Amann M C, Bosch T, Lescure M, Myllyla R, and Rioux M. "Laser ranging: a critical review of usual techniques for distance measurement". *Optical Engineering*, 40(1):10, 2001. ISSN 00913286. doi:10.1117/1.1330700.

[4] Barwood G, Gill P, and Rowley W. "Laser diodes for length determination using swept-frequency interferometry". *Measurement Science and Technology*, 4:988–994, 1993.

[5] Barwood G, Gill P, and Rowley W. "High-accuracy length metrology using multiple-stage swept-frequency interferometry with laser diodes". *Measurement Science and Technology*, 9(7):1036–1041, 1998.

[6] Battaglia M, de Roeck A, Ellis J R, and Schulte D. *Physics at the CLIC Multi-TeV Linear Collider : report of the CLIC Physics Working Group*. CERN, Geneva, 2004.

[7] Bechstein K h and Fuchs W. "Absolute interferometric distance measurements applying a variable synthetic wavelength". *Journal of Optics*, 29:179, 1998.

[8] Bedrosian E. "A product theorem for Hilbert transforms". *Proceedings of the IEEE*, 1962.

[9] Berkovic G, Rotter S, Shafir E, Scandale W, and Todesco E. "Wavelength-modulated fiber optic sensor for high precision displacement measurement". *Review of Scientific Instruments*, 73(10):3687, 2002. ISSN 00346748. doi:10.1063/1.1502001.

[10] Boashash B. "Estimating and interpreting the instantaneous frequency of a signal - Part 1: Fundamentals". *Proceedings of the IEEE*, 80(4):520–538, 1992. doi:10.1109/5.135376.

[11] Boashash B. "Estimating and interpreting the instantaneous frequency of a signal - Part II: Algorithms and applications". *Proceedings of the IEEE*, 80(4):540–568, 1992. ISSN 00189219. doi:10.1109/5.135378.

[12] Bobroff N. "Recent advances in displacement measuring interferometry". *Measurement Science and Technology*, 4(9):907–926, 1993. ISSN 0957-0233. doi:10.1088/0957-0233/4/9/001.

[13] Bosch T and Lescure M. *Selected papers on laser distance measurement*. SPIE, 1995. ISBN 9780819420107.

[14] Box M J. "Bias in nonlinear estimation". *Journal of the Royal Statistical Society*, 33(2):171–201, 1971.

[15] Brau J, Okada Y, and Walker N. "ILC Reference Design Report". Technical report, ILC Global Design Effort, 2007.

[16] Cabral A and Rebordao J. "Accuracy of frequency-sweeping interferometry for absolute distance metrology". *Optical Engineering*, 46(7):073 602, 2007. ISSN 00913286. doi:10.1117/1.2754308.

[17] Cheng Y Y and Wyant J C. "Multiple-wavelength phase-shifting interferometry." *Applied optics*, 24(6):804, 1985. ISSN 0003-6935.

[18] Ciddor P E. "Refractive index of air: new equations for the visible and near infrared". *Applied Optics*, 35(9):1566, 1996. ISSN 0003-6935. doi:10.1364/AO.35.001566.

[19] Cioci A, Spinetti A, Carosso L, and Atzeni C. "Digital Three-Dimensional Modeling of Heritage by Frequency-Modulated Laser Radar: the case of Donatellos David". In "The 6th International Symposium on Virtual Reality, Archaeology and Cultural Heritage", 2005.

[20] Coe P A. *An Investigation of Frequency Scanning Interferometry for the alignment of the ATLAS semiconductor tracker*. Dphil thesis, University of Oxford, 2001.

[21] Coe P A, Howell D F, and Nickerson R B. "Frequency scanning interferometry in ATLAS: remote, multiple, simultaneous and precise distance measurements in a hostile environment". *Measurement Science and Technology*, 15(11):2175–2187, 2004. ISSN 0957-0233. doi:10.1088/0957-0233/15/11/001.

[22] Dale J. *A Study of Interferometric Distance Measurement Systems on a Prototype Rapid Tunnel Reference Surveyor and the Effects of Reference Network Errors at the International Linear Collider*. Dphil thesis, University of Oxford, 2009.

[23] Dändliker R, Thalmann R, and Prongué D. "Two-wavelength laser interferometry using superheterodyne detection." *Optics letters*, 13(5):339–41, 1988. ISSN 0146-9592.

[24] Deck L L. "Absolute distance measurements using FTPSI with a widely tunable IR laser". *Proceedings of SPIE*, 4778:218–226, 2002. ISSN 0277786X. doi:10.1117/12.473544.

[25] Edmundson K and Baker L. "Photogrammetric measurement of the Arecibo primary reflector surface". In "Coordinate Metrology Society Conference", 2001.

[26] Estler W, Edmundson K, Peggs G, and Parker D. "Large-Scale Metrology An Update". *CIRP Annals - Manufacturing Technology*, 51(2):587–609, 2002. ISSN 00078506. doi: 10.1016/S0007-8506(07)61702-8.

[27] Estler W T. "High-accuracy displacement interferometry in air." *Applied optics*, 24(6):808, 1985. ISSN 0003-6935.

[28] Fox-Murphy A. *Development of a novel alignment system for the ATLAS Inner Detector and an investigation of the effect of alignment inaccuracies on tracker performance.* Dphil thesis, University of Oxford, 1996.

[29] Gibson S M. *The ATLAS SCT alignment system and a comparative study of misalignment at CDF and ATLAS.* Dphil thesis, University of Oxford, 2004.

[30] Gibson S M, Dehchar M, Horton K, Lewis A, Liang Z, Livermore S, Mattravers C, and Nickerson R B. "A novel method for ATLAS FSI alignment based on rapid, direct phase monitoring". Technical Report ATL-INDET-PROC-2010-037, CERN, Geneva, 2010.

[31] Gilbert S L and Swann W C. "NIST special publication 260-133 - Acetylene Absorption Reference for 1510 nm to 1540 nm Wavelength Calibration". Technical report, NIST, 2001.

[32] Gill E, Steckling M, and Butz P. "Gemini: A milestone towards autonomous formation flying". In "ESA Workshop on On-Board Autonomy", pages 415–419. 2001.

[33] Glombitza U and Brinkmeyer E. "Coherent frequency-domain reflectometry for characterization of single-mode integrated-optical waveguides". *Journal of Lightwave Technology*, 11(8):1377–1384, 1993. ISSN 07338724. doi:10.1109/50.254098.

[34] Green J R. *Development of a Prototype Frequency Scanning Interferometric Absolute Distance Measurement System for the Survey & Alignment of the International Linear Collider.* Dphil thesis, University of Oxford, 2007.

[35] Grewal A S. *Detector Development for ATLAS and Supersymmetry Physics Studies.* Dphil thesis, University of Oxford, 1999.

[36] de Groot P. "Chromatic dispersion effects in coherent absolute ranging." *Optics Letters*, 17(12):898, 1992. ISSN 0146-9592.

[37] de Groot P. "Unusual techniques for absolute distance measurement". *Optical Engineering*, 40(1):28, 2001. ISSN 00913286. doi:10.1117/1.1330702.

[38] Hand S D, Mongon W J, Clark J F F, and Schindelholz E. "Measurement of the USS Monitor propeller using structured light and coherent laser radar scanning technologies". *Journal of the CMSC*, 1(1):18–26, 2006.

[39] Hartmann L, Meiners-Hagen K, and Abou-Zeid A. "An absolute distance interferometer with two external cavity diode lasers". *Measurement Science and Technology*, 19(4):045 307, 2008. ISSN 0957-0233. doi:10.1088/0957-0233/19/4/045307.

[40] Heydemann P L M. "Determination and correction of quadrature fringe measurement errors in interferometers". *Applied Optics*, 20(19):3382, 1981. ISSN 0003-6935. doi: 10.1364/AO.20.003382.

[41] Kikuta H, Iwata K, and Nagata R. "Distance measurement by the wavelength shift of laser diode light". *Applied optics*, 25(17):2976–2980, 1986.

[42] Korpelainen V and Lassila A. "Acoustic method for determination of the effective temperature and refractive index of air in accurate length interferometry". *Optical engineering*, 43:2400, 2004.

[43] Lawson P R and Dooley J A. "Technology Plan for the Terrestrial Planet Finder Interferometer". Technical Report June, NASA, 2005.

[44] Lewis A J. *Absolute length measurement using multiple-wavelength phase-stepping interferometry*. Phd thesis, Imperial College London, 1993.

[45] Matsumoto H and Honda T. "Interferometer using the two-colour method of compensating for the refractive index of air". *Measurement science and technology*, 3:1084–1086, 1992.

[46] Meiners-Hagen K, Schödel R, Pollinger F, and Abou-Zeid A. "Multi-Wavelength Interferometry for Length Measurements Using Diode Lasers". *Measurement Science Review*, 9(1):16–26, 2009. ISSN 1335-8871. doi:10.2478/v10048-009-0001-y.

[47] Mendrin M J and Taylor R H. "Variable Frequency Interferometer", 1976.

[48] Michelson A and Morley E. "On the relative motion of the earth and the luminiferous ether". *The American Journal of Science*, 34(203):333–345, 1887.

[49] Mitra A. *Development of an APD amplifier for the Runtime Alignment of the ATLAS Inner Detector and SUSY studies*. Dphil thesis, University of Oxford, 2002.

[50] Moles-Valls R. "Alignment of the ATLAS inner detector tracking system". *Nuclear Instruments and Methods in Physics Research Section A: Accelerators, Spectrometers, Detectors and Associated Equipment*, 617(1-3):568–570, 2010.

[51] Nakamura K, Hara T, Yoshida M, Miyahara T, and Ito H. "Optical frequency domain ranging by a frequency-shifted feedback laser". *IEEE Journal of Quantum Electronics*, 36(3):305–316, 2000. ISSN 00189197. doi:10.1109/3.825877.

[52] NIST. "NIST engineering metrology toolbox - http://emtoolbox.nist.gov", 2011.

[53] Nordin D. *Optical Frequency Modulated Continuous Wave (FMCW) Range and Velocity Measurements*. Ph.D. thesis, Lulea University of Technology, 2004.

[54] Nuhn H D. "LCLS Undulator commissioning, alignment, and performance". Technical report, Stanford Linear Accelerator Center (SLAC), 2009.

[55] Riles K and Nyberg S. "High-precision absolute distance measurement using dual-laser frequency scanned interferometry under realistic conditions". *Nuclear Instruments and Methods in Physics Research Section A: Accelerators, Spectrometers, Detectors and Associated Equipment*, 575(3):395–401, 2007. ISSN 01689002. doi:10.1016/j.nima.2007.02.101.

[56] Schneider R, Thurmel P, and Stockmann M. "Distance measurement of moving objects by frequency modulated laser radar". *Optical Engineering*, 40(1):33, 2001. ISSN 00913286. doi:10.1117/1.1332772.

[57] Schwenke H, Schmitt R, Jatzkowski P, and Warmann C. "On-the-fly calibration of linear and rotary axes of machine tools and CMMs using a tracking interferometer". *CIRP Annals-Manufacturing Technology*, 58(1):477–480, 2009.

[58] Stone J, Stejskal A, and Howard L. "Absolute interferometry with a 670-nm external cavity diode laser". *Applied Optics*, 38(28):5981–5994, 1999.

[59] Suematsu M and Takeda M. "Wavelength-shift interferometry for distance measurements using the Fourier transform technique for fringe analysis". *Applied Optics*, 30(28), 1991.

[60] Swinkels B. *High-accuracy absolute distance metrology*. Phd thesis, Technical University of Delft, 2006.

[61] Thiel J, Pfeifer T, and Hartmann M. "Interferometric measurement of absolute distances of up to 40 m". *Measurement*, 16:1–6, 1995.

[62] Tretter S. "Estimating the frequency of a noisy sinusoid by linear regression". *IEEE Transactions on Information Theory*, 31(6):832–835, 1985.

[63] Umetsu K, Furutnani R, Osawa S, Takatsuji T, and Kurosawa T. "Geometric calibration of a coordinate measuring machine using a laser tracking system". *Measurement Science and Technology*, 16(12):2466–2472, 2005. ISSN 0957-0233. doi:10.1088/0957-0233/16/12/010.

[64] Wells D E and Krakiwsky E J. "The Method Of Least Squares", 1971.

[65] Xiaoli D and Katuo S. "High-accuracy absolute distance measurement by means of wavelength scanning heterodyne interferometry". *Measurement Science and Technology*, 9:1031–1035, 1998.

[66] Yang H J, Deibel J, Nyberg S, and Riles K. "High-precision absolute distance and vibration measurement with frequency scanned interferometry." *Applied optics*, 44(19):3937–44, 2005. ISSN 0003-6935.

[67] Zheng J. "Analysis of optical frequency-modulated continuous-wave interference." *Applied optics*, 43(21):4189–4198, 2004. ISSN 0003-6935.